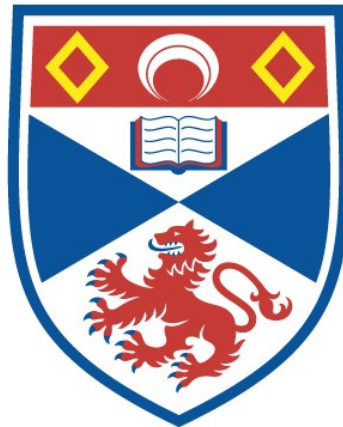


# OPTIMIZATION OF SPRAY PYROLYSIS FOR CATHODE-SUPPORTED SOLID OXIDE FUEL CELLS

Georgios Tsimekas

A Thesis Submitted for the Degree of PhD  
at the  
University of St Andrews



2019

Full metadata for this thesis is available in  
St Andrews Research Repository  
at:

<http://research-repository.st-andrews.ac.uk/>

Identifiers to use to cite or link to this thesis:

DOI: <https://doi.org/10.17630/10023-17385>  
<http://hdl.handle.net/10023/17385>

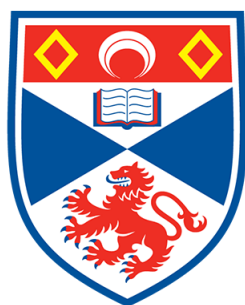
This item is protected by original copyright

This item is licensed under a  
Creative Commons License

<https://creativecommons.org/licenses/by-nc-nd/4.0>

# Optimization of Spray Pyrolysis for Cathode-Supported Solid Oxide Fuel Cells

Georgios D. Tsimekas



University of  
St Andrews

This thesis is submitted in partial fulfilment  
for the degree of Doctor of Philosophy (PhD)  
at the University of St Andrews

September 2018

*Dedicated to my parents Stavroula & Dimitris for their sacrificial love*

# Declarations

## **Candidate's declaration**

I, Georgios Tsimekas, do hereby certify that this thesis, submitted for the degree of PhD, which is approximately 29,000 words in length, has been written by me, and that it is the record of work carried out by me, or principally by myself in collaboration with others as acknowledged, and that it has not been submitted in any previous application for any degree.

I was admitted as a research student at the University of St Andrews in September 2014.

I received funding from an organisation or institution and have acknowledged the funder(s) in the full text of my thesis.

Date

Signature of candidate

## **Supervisor's declaration**

I hereby certify that the candidate has fulfilled the conditions of the Resolution and Regulations appropriate for the degree of PhD in the University of St Andrews and that the candidate is qualified to submit this thesis in application for that degree.

Date

Signature of supervisor

**Permission for publication**

In submitting this thesis to the University of St Andrews we understand that we are giving permission for it to be made available for use in accordance with the regulations of the University Library for the time being in force, subject to any copyright vested in the work not being affected thereby. We also understand, unless exempt by an award of an embargo as requested below, that the title and the abstract will be published, and that a copy of the work may be made and supplied to any bona fide library or research worker, that this thesis will be electronically accessible for personal or research use and that the library has the right to migrate this thesis into new electronic forms as required to ensure continued access to the thesis.

I, Georgios Tsimekas, confirm that my thesis does not contain any third-party material that requires copyright clearance.

The following is an agreed request by candidate and supervisor regarding the publication of this thesis:

**Printed copy**

Embargo on all of print copy for a period of 1 year on the following ground(s):

- Publication would preclude future publication

**Supporting statement for printed embargo request**

- Publication would preclude further publication

**Electronic copy**

Embargo on all of electronic copy for a period of 1 year on the following ground(s):

- Publication would preclude future publication

**Supporting statement for electronic embargo request**

- Publication would preclude further publication

**Title and Abstract**

- I agree to the title and abstract being published.

Date

Signature of candidate

Date

Signature of supervisor

## **Underpinning Research Data or Digital Outputs**

### **Candidate's declaration**

I, Georgios Tsimekas, understand that by declaring that I have original research data or digital outputs, I should make every effort in meeting the University's and research funders' requirements on the deposit and sharing of research data or research digital outputs.

Date

Signature of candidate

### **Permission for publication of underpinning research data or digital outputs**

We understand that for any original research data or digital outputs which are deposited, we are giving permission for them to be made available for use in accordance with the requirements of the University and research funders, for the time being in force. We also understand that the title and the description will be published, and that the underpinning research data or digital outputs will be electronically accessible for use in accordance with the license specified at the point of deposit, unless exempt by award of an embargo as requested below.

The following is an agreed request by candidate and supervisor regarding the publication of underpinning research data or digital outputs:

Embargo on all of electronic files for a period of 1 year on the following ground(s):

- Publication would preclude future publication

### **Supporting statement for embargo request**

- Publication would preclude further publication

### **Title and Description**

- I require an embargo on the title and description

Date

Signature of candidate

Date

Signature of supervisor



# Acknowledgements

The completion of the work in this thesis would not have been possible without the contribution and support of many people.

First and foremost, I would like to express my sincere gratitude to my supervisor, *Prof. John Irvine* for his trust and unlimited support all these years. His great ideas, shed light to the darkest moments of the experimental work and this was a priceless encouragement.

Many thanks also to *Dr. Paul Connor* and *Dr. Cristian Savaniu* for the countless hours of stimulating scientific discussion and their overall help.

I would also like to thank *Ms Candice Mitchell* for research administrative support.

Special thanks to *PhD student Jianing Hui* for his hospitality when I arrived in St Andrews for the first time. He has always been a good friend and always willing to help me with my work.

I am much obliged to: *Mr Ross Blackley* and *Dr. David Miller* for the training and support in electron microscopy. *Dr. Yuri Andreev* and *Dr. Julia Payne* for the help with the X-ray diffraction measurements and their insightful advices on this method. *Ms Sylvia Williamson* for her technical support and advice on thermal analysis equipment. *Ms Julie Nairn* for assistance in scientific equipment purchase and always willing to help.

I greatly appreciate also the help from *Dr. George Carins* and *Dr. Zac Dehaney-Steven* to solve various equipment setbacks and their advice on sealing materials.

Many thanks to my dearest friend *Dr. Kyriakos Giagloglou* for the joyful discussions and moments outside the lab.

I would also like to thank *Mr Drew Anderson*, *Mr Bob Cathcart* and *Mr George Anthony* whose creativity and technical expertise to build essential parts of the experimental equipment was a tremendous help.

Special thanks to present and former members of the JTSI group who supported me during my work: *Dr.Despoina Papargyriou, PhD student Stewart Dickson, Dr.Robert Price, Dr.Alfredo Damiano Bonaccorso, Dr.Aida Fuente Cuesta, Dr.JinGoo Lee, Dr.Yue Xiangling, Dr.Mark Cassidy, Dr.Georgios Triantafyllou and Dr.Dragos Neagu.*

I am also grateful to *Prof.Nikolas Kiratzis* of the Department of Environmental Engineering of Technological Educational Institute of Western Macedonia, for the opportunity to work at his lab and become familiar with spray pyrolysis technique in the first place. He has inspired me to pursue a PhD and always to chase my dreams in life and future career.

Special thanks to *Prof.Michael Stoukides* of the Department of Chemical Engineering of Aristotle University of Thessaloniki and members of his research team *Dr.Vasilis Kyriakou* and *Dr.Ioannis Garagounis*, for insightful scientific discussions and help with experimental work.

Many thanks to *Dr.Dainius Perednis*, who I did not have the chance to meet in person yet. His work on spray pyrolysis was a stepping stone to this research and a great help.

The financial support by the *University of St Andrews* and the *ArchimedesIII research program: Optimization of fabrication processes of solid electrolyte fuel cell components for the direct electrochemical oxidation of hydrocarbons* is kindly acknowledged.

I would also like to thank my spiritual father *Raphael Pavouris* who was a source of continuous guidance and motivation in hard times.

Finally, I wish to express my warmest thanks to my beloved wife *Angeliki* for her unlimited patience and care throughout my studies.

# Abstract

Cathode-supported solid oxide fuel cells (SOFCs) have been the most reliable devices for direct conversion of fuels in electrical power. However, processing at high temperatures to obtain a gas-tight electrolyte is prohibited due to formation of interfacial secondary phases between the electrolyte and the cathode support. Various deposition techniques such as electrochemical vapor deposition have been successfully employed to deposit thin electrolytes, but with a high cost. Therefore, a fabrication method that can meet the requirements of an industrial application at lower cost is the key for commercialization of this type of SOFCs.

The aim of this study was to optimize air-pressurized spray pyrolysis technique for preparation of ultra-thin and dense electrolytes at low temperatures, for cathode-supported SOFCs. This process is cost-effective and easy scalable, suitable for deposition of thin films over large areas.

Cathode-supported SOFCs were developed with thin 3.5-5.5  $\mu\text{m}$  yttria-stabilized zirconia (YSZ) electrolytes of columnar structure, at deposition temperatures as low as 170  $^{\circ}\text{C}$  and deposition rates  $\geq 10 \mu\text{m h}^{-1}$ . The surface of the composite LSM-YSZ cathode support was modified by spraying a LSM interlayer to reduce the roughness of the substrate and thus, secure a uniform thickness of the post-deposited electrolyte layer. To complete the cell with an anode electrode, cobalt ceria  $\text{Co-CeO}_2$  with mixed ionic-electronic conductivity (MIEC) was also deposited by spray pyrolysis. Optimization of spray pyrolysis process parameters revealed the precursor concentration in conjunction with deposition time as the most important parameters to shift the morphology of the film from dense to porous depended on the target film structure. Sintering, from 750  $^{\circ}\text{C}$  up to 950  $^{\circ}\text{C}$ , proved to suppress the formation of zirconate phases at the interface of the YSZ/LSM that would severely degrade the performance of the cell.

The cathode-supported SOFCs were electrochemically tested using 5% $\text{H}_2/\text{Ar}$  as fuel and air as oxidant within a temperature range of 700-850  $^{\circ}\text{C}$ . The measured open circuit voltage values were close to the theoretical ones with a maximum of 1.002 V at

850 °C, indicating a gas-tight electrolyte. A power density of 127 mW cm<sup>2</sup> at 850 °C for a cathode-supported SOFC with a 3.5 μm thick YSZ electrolyte, was achieved. The activation energy of the whole cell was 0.15 eV corroborating the actual ohmic resistance values correspond to the cathode support which is the limiting factor of the cell's performance. Long-term stability test of five days showed a performance degradation to 83 mW cm<sup>2</sup> at 850 °C due to particle agglomeration of the cobalt metal in the anode electrode and reduction of the catalytic active area. The above indicate spray pyrolysis is an established technique for preparation of thin films for use in cathode-supported SOFCs.

# Contents

<b>Declarations</b>	<b>iii</b>
<b>Acknowledgements</b>	<b>vii</b>
<b>Abstract</b>	<b>ix</b>
<b>List of Figures</b>	<b>xiii</b>
<b>List of Tables</b>	<b>xxi</b>
<b>Acronyms</b>	<b>xxiii</b>
<b>1 Introduction</b>	<b>1</b>
1.1 Fuel Cells . . . . .	1
1.2 Fundamentals of SOFCs . . . . .	2
1.3 Challenges and solutions of SOFC designs . . . . .	5
1.4 Processing methods . . . . .	8
1.5 Spray pyrolysis technique . . . . .	10
1.6 Aim of the thesis . . . . .	13
<b>2 Materials and thin films characterisation techniques</b>	<b>15</b>
2.1 Spray pyrolysis apparatus . . . . .	15
2.2 Substrate preparation . . . . .	18
2.3 Precursor solution preparation . . . . .	20
2.4 Thermal analysis (DTA/TG) . . . . .	21
2.5 X-ray diffraction . . . . .	22
2.6 Scanning electron microscopy . . . . .	25
2.6.1 Energy dispersive X-ray spectroscopy . . . . .	29
2.7 Transmission electron microscopy . . . . .	30

---

2.8	Particle size analysis . . . . .	32
2.9	Electrochemical characterisation . . . . .	32
2.9.1	Electrochemical test apparatus . . . . .	32
2.9.2	AC Impedance spectroscopy . . . . .	35
2.9.3	Four-point DC conductivity . . . . .	38
<b>3</b>	<b>Preparation of substrates for cathode supported SOFCs</b>	<b>41</b>
3.1	Introduction . . . . .	41
3.2	Morphology characterization . . . . .	42
3.3	Conductivity measurements . . . . .	50
3.4	Conclusions . . . . .	53
<b>4</b>	<b>Origin of defects in SOFC thin films deposited by spray pyrolysis</b>	<b>55</b>
4.1	Introduction . . . . .	55
4.2	Spray pyrolysis process parameters . . . . .	56
4.2.1	Precursor solution . . . . .	58
4.2.2	Substrate temperature . . . . .	68
4.2.3	Precursor solution concentration . . . . .	84
4.2.4	Deposition time . . . . .	94
4.2.5	Precipitate particle size . . . . .	100
4.2.6	Precursor solution flow rate . . . . .	102
4.2.7	Spray gun nozzle-to-substrate distance . . . . .	104
4.3	Conclusions . . . . .	106
<b>5</b>	<b>Spray pyrolysis strategy for thin film SOFC electrolytes and electrodes</b>	<b>109</b>
5.1	Introduction . . . . .	109
5.2	Modification of substrate surfaces . . . . .	110
5.3	Deposition of thin electrolytes by spray pyrolysis . . . . .	115
5.4	Spray deposition of nano-structured anode electrodes . . . . .	125
5.5	Conclusions . . . . .	129
<b>6</b>	<b>Electrochemical performance of cathode-supported SOFCs</b>	<b>131</b>
6.1	Introduction . . . . .	131
6.2	Electrical measurements . . . . .	132
6.3	Conclusions . . . . .	148
<b>7</b>	<b>General Conclusions</b>	<b>151</b>
	<b>References</b>	<b>155</b>

# List of Figures

1.1	Schematic view of the operating principle of SOFC. . . . .	2
1.2	Typical voltage/current polarization curve of a solid oxide fuel cell under operation. . . . .	4
1.3	Conductivity of SOFC oxygen ion conductors versus reciprocal temperature and thickness, modified from [38]. The ASR for a 3 $\mu\text{m}$ YSZ electrolyte is $\approx 0.08 \Omega \text{cm}^2$ at 600 $^\circ\text{C}$ . . . . .	8
1.4	Processing methods for preparation of solid oxide fuel cells. . . . .	9
1.5	Process steps of spray pyrolysis technique. . . . .	10
2.1	Spray pyrolysis apparatus where a) Infusion pump, b) Air flow controller, c) Hot plate, d) Aluminium plate, e) Substrate, f) Spray gun, g) Relief pressure valve, h) Spraying booth. . . . .	17
2.2	Automatic spray gun DeVilbiss AG-361 and coating pattern. . . . .	17
2.3	5LSM-3YSZ substrates in a button cell geometry (thick.1 mm, $\emptyset$ 11 mm) and sintering profile. . . . .	19
2.4	Schematic illustration of diffraction of X-rays by crystals . . . . .	23
2.5	Basic arrangement of X-ray diffractometer components. T is the X-ray source, D is the detector, C the sample holder and S the divergent slits . . . . .	24
2.6	Schematic drawing of main components of an SEM microscope [79].	26
2.7	Types of signals emitted upon impact of incident electron beam with a specimen [77]. . . . .	27
2.8	Schematic illustration of EDS principle [77]. . . . .	29
2.9	Schematic drawing of key components and ray diagram of a TEM microscope [79, 81]. . . . .	31
2.10	Schematic drawing of SOFC test apparatus . . . . .	33
2.11	SOFC sealing and electrical contacts . . . . .	34
2.12	Typical EIS impedance plots for a solid oxide fuel cell. . . . .	37

---

2.13	Four-point DC conductivity experimental apparatus. . . . .	38
3.1	SEM images in cross section of 5LSM substrates sintered at 1200 °C for two hours. . . . .	43
3.2	Top view SEM images of 5LSM powder a) as obtained after calcination at 800 °C for 1 hour and b) after sieving through a mesh (106 μm). . . . .	44
3.3	Particle size analysis of 5LSM powder before and after calcination at 800 °C for 1 hour with a heating-cooling rate of 3 °C/min. . . . .	45
3.4	TGA analysis of PMMA under air up to 900 °C with a heating rate of 3 °C/min. . . . .	46
3.5	Sintering profile of composite 5LSM-3YSZ substrates (1200 °C and dwell time of 2 hours). . . . .	47
3.6	SEM images of a,b) 5LSM-3YSZ (9:1 wt.%) in cross section with a uniform interconnected porosity of 42%. and c) 5LSM-8YSZ (1:1 wt.%) with a uniform porosity of 25 % sintered at 1200 °C for 2 hours. . . . .	48
3.7	5LSM-3YSZ substrate temperature correlated with the thickness. . . . .	48
3.8	XRD analysis of commercial ceramic powders of 5LSM (π-Kem ltd), 3YSZ (Tosoh) and 5LMS-3YSZ (9:1 wt.%) pellet sintered at 1200 °C for 2 hours. . . . .	49
3.9	5LSM-3YSZ composite cathode electrode prepared for 4-point DC conductivity measurement. . . . .	51
3.10	4-point DC conductivity measurements with a maximum value of 179 S/cm for the 5LSM and 119 S/cm for the 5LSM-3YSZ substrate at 800 °C. . . . .	51
3.11	Arrhenius plot of conductivity with activation energies $E_a$ of 5LSM and 5LSM-3YSZ substrates. . . . .	52
4.1	Photograph of the spray pyrolysis experimental apparatus. . . . .	57
4.2	TG/DTA analysis of zirconium oxynitrate up to 900 °C at a heating rate of 5 °C/min and dwell time of 10 min in air. . . . .	61
4.3	TG/DTA analysis of yttrium nitrate up to 900 °C at a heating rate of 5 °C/min and dwell time of 10 min in air. The three steps of thermal decomposition are also shown: dehydration, nitrates decomposition and crystallization. . . . .	62
4.4	TG/DTA analysis of as-deposited 8YSZ thin film ( $T_{sub.}:200\text{ °C}$ ) up to 900 °C at a heating rate of 10 °C/min and dwell time of 10 min in air. . . . .	63
4.5	X-ray diffraction pattern of 8YSZ thin film deposited on LSM-3YSZ porous substrate. Substrate temperature 200 °C, precursor concentration 0.025 mol/l, calcined at 500 °C for 2 hours. . . . .	64
4.6	TG/DTA analysis of as-deposited GDC thin film ( $T_{sub.}:183\text{ °C}$ ) up to 900 °C at a heating rate of 10 °C/min and dwell time of 10 min in air. . . . .	67

---

4.7	Spray pyrolysis processes initiated with increasing substrate temperature [121]. . . . .	69
4.8	SEM micrographs in top view of 8YSZ thin films deposited on porous cathode substrates of a) 5LSM-3YSZ(9:1wt.%) b) 5LSM-8YSZ(1:1 wt.%) showing the effect of substrate temperature. Precursor concentration 0.1 mol/l, solution flow rate 0.6 ml/min, air flow rate 30 l/min, deposition time 19.5 min, number of cycles 39, nozzle-to-substrated distance 25 cm, calcination at 540 °C for 1 hour and subsequent sintering at 900 °C for 2 hours every 5 min of spray deposition. . . . .	71
4.9	X-ray diffraction patterns of 8YSZ thin films deposited on porous cathodes substrates of 5LSM-8YSZ(1:1wt.%) at 210 °C and 5LSM-3YSZ (9:1wt.%) at 170 °C.( The 8YSZ peaks are denoted by miller indices, XRD patterns of uncoated substrates are also included for reference). . . . .	72
4.10	FIB-SEM micrographs in top view (a-b) and cross-section (c-d) of GDC films deposited on 8YSZ substrates showing the effect of substrate temperature. Precursor concentration 0.1 mol/l, solution flow rate 0.6 ml/min, air flow rate 30 l/min, deposition time 4 min, number of cycles 12, nozzle-to-substrate distance 25 cm, calcination at 540 °C for 1 hour and subsequent sintering at 850 °C for 2 hours. . . .	74
4.11	Deposition rates for GDC thin films deposited on dense substrates with respect to substrate temperature ( $T_{\text{sub}}$ ). Deposition rate for $T_{\text{sub}}$ :178 °C and 225 °C refer to this study, 310 °C to Rupp <i>et al.</i> [115], 400 °C to L. dos Santos Gomez <i>et al.</i> [109] and 410 °C to Szymczewska <i>et al.</i> [124]. . . . .	75
4.12	HAADF-STEM micrographs and EDS maps in cross section of GDC thin films deposited on 8YSZ disks at substrate temperatures of (a-b) 178 °C and (c-d) 225 °C. . . . .	76
4.13	XRD patterns of thin GDC films sprayed on dense YSZ substrates at 225 °C and 178 °C (the GDC peaks are denoted by miller indices and substrate peaks by *). . . . .	78
4.14	Electron diffraction patterns of GDC thin films deposited at different substrate temperatures: (a) 178 °C and (b) 225 °C exhibiting preferential (200) crystal orientation. . . . .	78
4.15	Williamson-Hall plot of GDC films deposited at different substrate temperatures. . . . .	80
4.16	Schematic of gold electrical contacts integrated onto a GDC thin film for 4-point DC conductivity measurements. . . . .	81

---

4.17	Electrical measurements of GDC thin films and 8YSZ substrate: (a) total resistances of GDC/8YSZ and 8YSZ substrate; (b) conductivity of the GDC thin films and 8YSZ. . . . .	82
4.18	Schematic illustration of the precursor solution concentration effect on particle morphology by spray pyrolysis [44]. . . . .	85
4.19	SEM micrographs in tilted view ( $45^\circ$ ) of 8YSZ particles formed during intermittent spray deposition onto porous 5LSM-3YSZ substrates showing the effect of volume and surface precipitation on particle morphology. Precursor concentration 0.1 mol/l, total deposition time 2.5 min with 30 sec/cycle, substrate temperature $210^\circ\text{C}$ , precursor solution flow rate 0.6 ml/min, air flow rate 30 L/min, nozzle-to-substrate 25 cm, sintering at $850^\circ\text{C}$ for 2 hours. . . . .	86
4.20	SEM micrographs in top view of 8YSZ thin films deposited on top of porous 5LSM-3YSZ substrates showing the effect of solution concentration and sintering temperature. Substrate temperature $200^\circ\text{C}$ , precursor solution flow rate 0.6 ml/min, air flow rate 30 L/min, deposition time 100 min, nozzle-to-substrate distance 25 cm, sintering at $500^\circ\text{C}$ and $850^\circ\text{C}$ for 2 hours. . . . .	88
4.21	SEM micrographs in top view of 8YSZ thin films deposited on top of porous 5LSM-3YSZ substrates showing the effect of solution concentration and intermittent spray deposition (a,b) 0.1 mol/l, 30 sec/cycle, 5 cycles (c,d) 0.05 mol/l, 2 min/cycle, 5 cycles. Substrate temperature $210^\circ\text{C}$ , precursor solution flow rate 0.6 ml/min, air flow rate 30 L/min, nozzle-to-substrate 25 cm, sintering at $500^\circ\text{C}$ and $850^\circ\text{C}$ for 2 hours. . . . .	90
4.22	X-ray diffraction patterns of 8YSZ thin films deposited with different precursor concentrations onto porous 5LSM-3YSZ substrates (The 8YSZ peaks are denoted by Miller indices). Deposition time 100 min, substrate temperature $200^\circ\text{C}$ , solution flow rate 0.6 ml/min, air flow rate 30 L/min, nozzle-to-substrate distance 25 cm, sintered at $500^\circ\text{C}$ and $850^\circ\text{C}$ for 2 hours. . . . .	92
4.23	Williamson Hall plot of 8YSZ thin films deposited onto porous substrates of 5LSM-3YSZ showing the effect of sintering temperature on the strain of the films. Precursor solution concentration 0.025 mol/l, deposition time 100 min, substrate temperature $200^\circ\text{C}$ , solution flow rate 0.6 ml/min, air flow rate 30 L/min, nozzle-to-substrate distance 25 cm, sintering at $500^\circ\text{C}$ and $850^\circ\text{C}$ for 2 hours, respectively. . . . .	93

- 4.24 SEM micrographs in top view and cross section of 8YSZ thin films deposited on top of porous 5LSM-3YSZ substrates showing the effect of deposition time (a) 4 min (b) 20 min (c) 60 min (d) 100 min. Precursor solution concentration 0.025 mol/l, solution flow rate 0.6 ml/min, air flow rate 30 L/min, substrate temperature 200 °C, nozzle-to-substrate 25 cm, sintering at 500 °C for 2 hours. . . . . 96
- 4.25 FEG-SEM micrographs in top view and cross section of 8YSZ thin films deposited onto porous 5LSM-3YSZ substrates showing the effect of deposition time and intermittent spray deposition: (a) 40 min (b) 80 min (c) 100 min. Deposition time per cycle 4 min, precursor concentration 0.025 mol/l, substrate temperature 170 °C, solution flow rate 0.6 ml/min, air flow rate 30 L/min, sintering at 750 °C for 2 hours. 98
- 4.26 X-ray diffraction patterns of 8YSZ thin films deposited on 5LSM-3YSZ substrates showing the effect of continuous spray deposition and intermittent spray deposition (deposition time: 4 min/cycle, 25 cycles) on preferential crystal orientation. Precursor solution concentration 0.025 mol/l, *total* deposition time 100 min, solution flow rate 0.6 ml/min, air flow rate 30 L/min, nozzle-to-substrate 25 cm. . . . . 99
- 4.27 SEM micrographs in top view of 8YSZ thin films deposited on top of porous 5LSM-3YSZ substrates showing the effect of precipitate particles size: (a) 0.005mol/l for 100 min (b) 0.025 mol/l for 4 min (c) 0.025 mol/l for 20 min. Substrate temperature 200 °C, precursor solution flow rate 0.6 ml/min, air flow rate 30 L/min, nozzle-to-substrate 25 cm, sintering at 500 °C for 2 hours. . . . . 101
- 4.28 SEM micrographs in top view of 8YSZ thin films deposited in steps of 30 sec with 40 min of pause at 500 °C, on top of 5LSM-3YSZ substrates showing the effect of precursor solution flow rate (a) 1.0 ml/min (b) 1.5 ml/min (c) 2.7 ml/min. Precursor solution concentration 0.1 mol/l, air flow rate 30 L/min, substrate temperature 220 °C, *total* deposition time 2.5 min, nozzle-to-substrate 25 cm, sintering at 500 °C for 2 hours. . . . . 103
- 4.29 SEM micrographs (a) in cross section and (b,c,d) in top view of 8YSZ thin films deposited on top of porous 5LSM-3YSZ substrates showing the effect of a higher nozzle-to-substrate distance. The spray gun nozzle was fixed at 36 cm from the substrate. Precursor solution concentration 0.1 mol/l, substrate temperature 220 °C, solution flow rate 0.6 ml/min, air flow rate 30 L/min, deposition time 5 min, sintering at 750 °C for 2 hours. . . . . 105

- 
- 5.1 SEM micrographs in top view and cross section of 8YSZ thin film (0.6-1.25  $\mu\text{m}$ ) deposited onto porous cathode substrate of 5LSM-3YSZ. Precursor solution 0.1 mol/l, deposition time 15 min, number of spray cycles 30, Substrate temperature 220  $^{\circ}\text{C}$ , nozzle-to-substrate distance 25 cm, sintering temperature 500  $^{\circ}\text{C}$  for 2 hours. . . . . 111
- 5.2 Modification of the porous cathode substrate surface by spray deposition of  $\text{La}_{0.8}\text{Sr}_{0.2}\text{MnO}_3$  thin interlayer and subsequent spray deposition of a 8YSZ thin electrolyte: a) 5LSM-3YSZ(9:1 wt.%), sintered at 1200  $^{\circ}\text{C}$  for 2 hours b) precursor concentration 0.025 mol/l, deposition time 10 min, 5 spray cycles, substrate temperature 200  $^{\circ}\text{C}$ , sintering at 750  $^{\circ}\text{C}$  for 2 hours, c) precursor concentration 0.1 mol/l, deposition time 10 min, 20 spray cycles, substrate temperature 200  $^{\circ}\text{C}$ , Nozzle-to-substrate distance 25 cm, solution flow rate 0.6 ml/min, air flow rate 30 l/min, sintering at 750  $^{\circ}\text{C}$  for 2 hours. . . . . 113
- 5.3 SEM micrographs in cross section of 8YSZ thin electrolyte (2.4-2.8  $\mu\text{m}$ ) deposited onto a porous cathode substrate of 5LSM-3YSZ with an interlayer of LSM. Precursor concentration 0.1 mol/l, substrate temperature 200  $^{\circ}\text{C}$ , deposition time 15 min, 30 spray cycles, solution flow rate 0.6 ml/min, air flow rate 30 l/min, nozzle-to-substrate distance 25 cm, sintering temperature 750  $^{\circ}\text{C}$  for 2 hours with a heating-cooling rate of 3  $^{\circ}\text{C}/\text{min}$ . . . . . 114
- 5.4 FEG-SEM micrographs in cross section of 8YSZ thin films (5.7  $\mu\text{m}$  thick.) deposited on sprayed interlayer of LSM supported on porous cathode substrates of 5LSM-3YSZ. Precursor concentration 0.1 mol/l, deposition time 25 min, 50 spray cycles, substrate temperature 170  $^{\circ}\text{C}$ , solution flow rate 0.6 ml/min, air flow rate 30 l/min, nozzle-to-substrate distance 25 cm, sintering at 750  $^{\circ}\text{C}$  for 2 hours. . . . . 117
- 5.5 FEG-SEM micrograph in cross section of 8YSZ thin electrolyte deposited on porous cathode substrate of 5LSM-8YSZ(1:1 wt.%). Precursor concentration 0.05 mol/l, deposition time 2.5 min, 5 spray cycles, Precursor concentration 0.1 mol/l, deposition time 11.5 min, 23 spray cycles, substrate temperature 210  $^{\circ}\text{C}$ , solution flow rate 0.6 ml/min, air flow rate 30 l/min, nozzle-to-substrate 25 cm, sintering at 900  $^{\circ}\text{C}$  for 2 hours. . . . . 117
- 5.6 TEM micrographs in cross section of 8YSZ thin films a) deposited at 220  $^{\circ}\text{C}$  and sintered at 500  $^{\circ}\text{C}$  b) deposited at 170  $^{\circ}\text{C}$  and sintered at 900  $^{\circ}\text{C}$  c) Electron diffraction pattern of 8YSZ preferential(111) oriented film d) Selected area electron diffraction (SAED) pattern of a single crystal 8YSZ. . . . . 119

- 
- 5.7 Variable temperature X-ray diffraction (VT-XRD) patterns of a 8YSZ thin film sintered initially at 750 °C for 2 hours. An isotherm of 1 hour was kept at each temperature during the measurement (Mo,  $K_{\alpha 1,2}$ , \* corresponds to substrate peaks). . . . . 121
- 5.8 X-ray diffraction patterns of 8YSZ thin films in (a) and the corresponding Williamson-Hall plots in (b) sintered at 750 °C for 2 hours and 950 °C for 1 hour, respectively. Precursor solution 0.1 mol/l, total deposition time 25 min, 50 spray cycles, substrate temperature 170 °C, nozzle-to-substrate distance 25 cm. . . . . 122
- 5.9 EDS analysis of 8YSZ thin film (5.5  $\mu\text{m}$  thick.) deposited on porous cathode substrates of 5LSM-3YSZ after sintering at 950 °C. Chemical composition 84.36 at.% for Zr and 15.64 at.% for Y. . . . . 124
- 5.10 SEM micrographs in top view of Ni-YSZ anode prepared by spray pyrolysis after testing electrochemically in 5%  $\text{H}_2/\text{Ar}$ . Precursor concentration 0.005 mol/l, deposition time 270 min, 3 spray cycles, substrate temperature 210 °C, solution flow rate 0.6 ml/min, air flow rate 30 l/min, nozzle-to-substrate distance 25 cm, sintering at 750 °C for 2 hours. . . . . 126
- 5.11 SEM micrographs in top view of nano-structured anode of Co–CeO<sub>2</sub> (1:1 vol.%) prepared by spray pyrolysis: a,b) oxidized and c,d) reduced after testing in  $\text{H}_2$  at 600 °C. Precursor concentration 0.005 mol/l, total deposition time 180 min, 2 spray cycles, substrate temperature 170 °C, solution flow rate 0.6 ml/min, air flow rate 30 l/min, nozzle-to-substrate distance 25 cm, sintering at 750 °C for 2 hours. . . . . 128
- 5.12 Four point conductivity of Co–CeO<sub>2</sub> in 5% $\text{H}_2/\text{Ar}$ , deposited on tape cast 8YSZ by spray pyrolysis. Precursor concentration 0.005 mol/l, deposition time 180 min, 2 spray cycles, substrate temperature 170 °C solution flow rate 0.6 ml/min, air flow rate 30 l/min, nozzle-to-substrate distance 25 cm, sintered at 750 °C for 2 hours. . . . . 129
- 6.1 SEM micrographs in cross section and top view of cathode-supported SOFC(no.A1) with a 3.5  $\mu\text{m}$  thick 8YSZ electrolyte and Co–CeO<sub>2</sub> anode after testing in 5% $\text{H}_2$  for  $\approx$  100h. . . . . 135
- 6.2 Long-term performance of cathode-supported SOFC(no.A1) under 5% $\text{H}_2/\text{Ar}$  at various temperatures for 5 days. (\* I-V curve obtained during the 4<sup>th</sup> day of operation). . . . . 137
- 6.3 TEM and EDS analysis of the Co–CeO<sub>2</sub> anode electrode (fuel cell no.A1) after testing in 5% $\text{H}_2/\text{Ar}$  within a temperature range of 700-850 °C for 5 days. (a,c) TEM micrographs of the analysed area, (b,d) EDS mapping of cobalt, cerium, zirconium and gold. Gold paste used as a current collector explaining the presence of Au particles. . . . . 138

---

6.4	Impedance spectra of cathode-supported SOFC(no.A1) obtained at OCV within a temperature range of 700-850 °C for a) 1 day and b) after 5 days. . . . .	140
6.5	Arrhenius plot of the inverse ohmic resistance for a cathode-supported SOFC (no.A1) over a range of operating temperatures in 5%H <sub>2</sub> /Ar. .	141
6.6	SEM micrograph in cross section of a cathode-supported SOFC (no.A2) after testing in pure H <sub>2</sub> at 600 °C. . . . .	143
6.7	Electrochemical performance of cathode-supported SOFC(no.A2) in pure H <sub>2</sub> a) Voltage and power density vs current density and b) Impedance spectra obtained at open circuit voltage. . . . .	144
6.8	SEM micrograph in cross section of a cathode-supported SOFC (no.A3) with a 3.8 μm 8YSZ electrolyte after testing in 5%H <sub>2</sub> /Ar at various temperatures for 5 consecutive days. . . . .	145
6.9	Long-term performance of cathode-supported SOFC(no.A3) in 5%H <sub>2</sub> /Ar a) I-V and I-P curves and b) Impedance spectra obtained at open circuit voltage . . . . .	146
6.10	SEM micrographs in top view of Co–CeO <sub>2</sub> (fuel cell no.A3) after testing in 5%H <sub>2</sub> /Ar at intermediate operating temperatures for 5 days.	147
6.11	Open circuit voltage (OCV) of cathode-supported SOFC(no.A3) as a function of time at 700 °C in 5%H <sub>2</sub> /Ar. . . . .	147

# List of Tables

1.1	Characteristics of SOFC designs. . . . .	6
1.2	Performance of SOFCs with supported thin electrolytes prepared by spray pyrolysis. . . . .	13
2.1	Aqueous dispersion composition and stages of roll milling. . . . .	20
2.2	Aqueous precursor solutions. . . . .	21
2.3	Impedance of modeling electrical elements. . . . .	37
2.4	Simulated capacitance values attributed to electrochemical processes [89]. . . . .	38
4.1	TGA results of metal nitrates and aqueous precursor solutions. . . . .	66
4.2	Lattice parameters of GDC. . . . .	77
4.3	Geometric parameters of the GDC films. . . . .	79
4.4	Lattice & geometric parameters of the 8YSZ films. Precursor concentration 0.025 mol/l, deposition time 100 min, substrate temperature 200 °C, nozzle-to-substrate distance 25 cm. . . . .	91
4.5	Summary of the spray pyrolysis process parameters effect on the morphology of YSZ and GDC thin films. . . . .	107
5.1	Thermal expansion coefficient of a 8YSZ film deposited on porous cathode substrate of 5LSM-3YSZ at various temperatures. (Mo, K <sub>α1</sub> )	120
5.2	Effect of sintering temperature on lattice & geometric parameters of a 8YSZ film deposited onto porous 5LSM-3YSZ substrate. Precursor concentration 0.1 mol/l, deposition time 25 min, 50 spray cycles, substrate temperature 170 °C, nozzle-to-substrate distance 25 cm. . .	123
5.3	Optimum spray pyrolysis process parameters for preparation of thin film cathode-supported SOFC components. . . . .	130

6.1	Spray pyrolysis process parameters for deposition of thin film cathode-supported SOFC components. . . . .	134
6.2	Long-term performance of cathode-supported SOFC(no.A1). . . . .	136
6.3	Total polarization ( $R_p$ ) and ohmic ( $R_s$ ) resistances of cathode-supported SOFC(no.A2) obtained at OCV. . . . .	143
6.4	Summary of the cathode-supported SOFCs performance . . . . .	149

# Acronyms

**3YSZ** 3 mol % Ytria-stabilized zirconia.

**5LSM** 5% A-site deficient strontium doped lanthanum manganite.

**8YSZ** 8 mol % Ytria-stabilized zirconia.

**AA-CVD** Aerosol-assisted chemical vapor deposition.

**APS** Atmospheric plasma spray.

**ASR** Area specific resistivity.

**BEs** Backscattered electrons.

**CPE** Constant phase element.

**CVD** Chemical vapor deposition.

**DTA** Differential thermal analysis.

**EDS** Energy dispersive X-ray spectroscopy.

**EIS** Electrochemical impedance spectroscopy.

**EVD** Electrochemical vapor deposition.

**FEG** Field emission gun.

**FIB** Focused ion beam.

**GDC** Gadolinia-doped ceria.

**HAADF** High-angle annular dark-field imaging.

**LSM** Strontium-doped lanthanum manganite.

**LZO** Lanthanum zirconate.

**MIEC** Mixed ionic-electronic conductor.

**OCV** Open circuit voltage.

**PLD** Pulsed laser deposition.

**PMMA** Poly(methyl methacrylate).

**PVD** Physical vapor deposition.

**SEM** Scanning electron microscopy.

**SEs** Secondary electrons.

**SOFCs** Solid Oxide Fuel Cells.

**SZO** Strontium zirconate.

**TEC** Thermal expansion coefficient.

**TEM** Transmission electron microscopy.

**TGA** Thermogravimetric analysis.

**TPBs** Triple phase boundaries.

**VT-XRD** Variable temperature X-ray diffraction.

**W-H** Williamson-Hall method.

**XRD** X-ray diffraction.

**YSZ** Yttria-stabilized zirconia.

# Introduction

## 1.1 Fuel Cells

The efficient production of electrical power in conjunction with reduced CO<sub>2</sub> emissions is a fundamental requirement for the industry and manufacturing sector, that will improve their economic viability [1]. To establish both, environment protection and economic development, a transition from energy systems based on thermal engines to a sustainable energy model based on efficient energy productive systems is needed [2].

The potential, to convert chemical fuels directly into electricity via an electrochemical process, has been demonstrated by fuel cells. These devices inherently exhibit the highest efficiency to produce electrical power, since are not limited by the Carnot cycle of thermal engines [3]. Since, the discovery of the first hydrogen fuel cell in 1839 by Sir William Grove [4], a vast development has been done on fuel cell technology to cover different applications energy demands [5].

## 1.2 Fundamentals of SOFCs

Solid oxide fuel cells (SOFCs) are electrochemical devices that convert the chemical energy of fuels directly into electrical power. The basic structure of a SOFC consists of two porous electrodes, the anode and the cathode, separated by a solid oxide ion-conductor electrolyte. The state-of-the-art SOFC typically consists of yttria-stabilized zirconia (YSZ) as the electrolyte, nickel/YSZ composite for the anode and strontium-doped lanthanum manganite (LSM) for the cathode. The operating temperature of SOFCs is commonly within 750-1000 °C dictated by the ionic conductivity of the electrolyte [6]. A schematic illustration of the operating principle of this device is shown in figure 1.1.

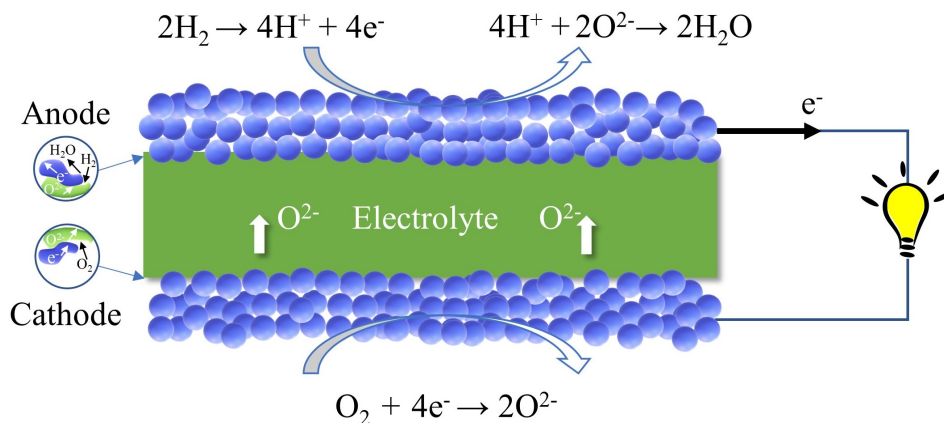


Figure 1.1: Schematic view of the operating principle of SOFC.

Under operation, fuel (*e.g.* hydrogen or methane) is supplied to the anode where it is oxidized, and releasing electrons to the external circuit. Oxygen is supplied to the cathode and by accepting electrons from the external circuit is reduced into  $\text{O}^{2-}$ , which migrate through the electrolyte reaching the anode. The driving force for the

operation of the SOFC is the electrochemical potential difference of oxygen between the two electrodes under equilibrium state (*i.e.* no current is flowing), expressed by the Nernst equation:

$$E^\circ = \frac{RT}{4F} \ln \left( \frac{pO_2^{(c)}}{pO_2^{(a)}} \right) \quad (1.1)$$

where  $E^\circ$  is the voltage of the cell when no current is flowing, known as open circuit voltage (OCV),  $R$  is the universal gas constant,  $T$  is the operating temperature,  $F$  is the faraday constant and  $(pO_2^{(c)})$  and  $(pO_2^{(a)})$  corresponding to the oxygen partial pressures at the cathode and the anode, respectively [7]. Electrochemical reactions shown in figure 1.1 mainly occur in the vicinity of the triple phase boundaries (TPBs) where the gas phase, the ionic conductor and the electronic conductor are joined together [8].

Figure 1.2 shows a characteristic I-V curve of a SOFC. The difference between the open circuit voltage and the operating cell voltage is defined as polarization or overpotential denoted as  $\eta$ . It should be noted, that if gas leakage occurs due to sealing cracks or existing pin holes through the electrolyte the starting OCV will be lower, reducing the cell's performance.

As current is drawn from the SOFC, the cell voltage falls due to ohmic, activation and concentration polarizations [9, 10]. The ohmic polarizations are the sum of the ohmic resistances of the electrodes, the interfaces of the electrodes with the current collectors and the electrolyte, with the latter to contribute the most (especially for thick  $>100 \mu\text{m}$  electrolytes). Activation polarizations are associated with charge transfer processes during the electrochemical reactions of the electrodes. The charge transfer for oxygen reduction at the cathode is known to be the limiting fac-

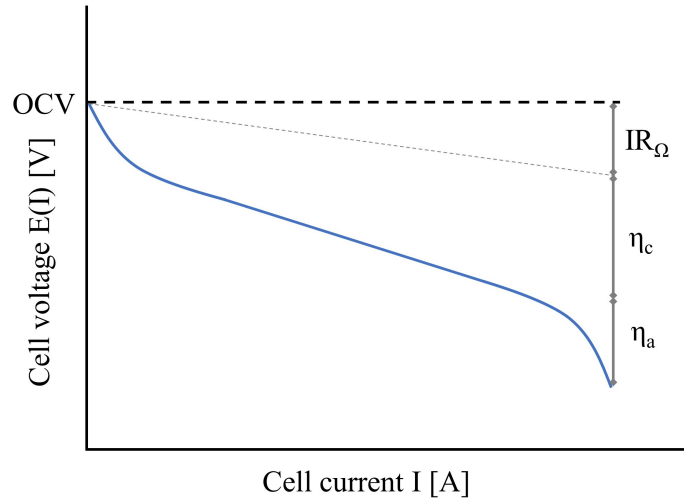


Figure 1.2: Typical voltage/current polarization curve of a solid oxide fuel cell under operation.

tor in SOFC performance, especially at low operating temperatures (*i.e.*  $< 800^\circ\text{C}$ ). Concentration polarizations associated with the transport of gases (*i.e.* fuel and oxidant) through the porous electrodes, therefore are dictated by the microstructure of the electrodes. Considering, the various polarizations that occur during operation, the voltage of the fuel cell is given by:

$$E(I) = E^\circ - IR_\Omega - \eta_c - \eta_a \quad (1.2)$$

where  $R_\Omega$  is the total ohmic losses of the cell and  $\eta_c$  and  $\eta_a$  are the polarization losses of the cathode and the anode, respectively.

To ensure a good performance, the components of the SOFC must meet certain requirements. The microstructure of each component has to be stable during fabrication and operation of the SOFC to avoid either delamination and cracking or particle agglomeration. In addition, chemical stability under oxidizing and/or

reducing atmospheres and similar thermal expansion coefficients (TECs) [3]. More specifically, the electrodes must be sufficiently porous to facilitate gas transport to the reaction sites (*i.e.* TPB) and also exhibit adequate electronic conductivity. Moreover, the SOFC performance can be enhanced extending the TPB region into the electrodes. This can be achieved by using composite electrodes comprising a mixture of ionic and electronic conductors or a single phase of mixed ionic-electronic conducting (MIEC) electrode [11]. On the other hand, the electrolyte which is the key component of the SOFC, has to be gas-tight to prevent mixing of the gases and also exhibit high ionic conductivity with negligible electronic conductivity at operating temperatures [12].

### 1.3 Challenges and solutions of SOFC designs

Single SOFCs in order to produce sufficient power output are combined in stacks. Depending on the specific stack configuration, SOFCs have been made into various designs with the most famous to be the tubular and planar design. The tubular design with the one-end closed feature has the advantage of seal-less design and the planar design offers higher power densities over its tubular counterpart. Based on the component which is used for mechanical support, SOFC designs are distinguished in electrolyte-supported, electrode-supported (*i.e.* anode or cathode) and metal-supported [13]. Table 1.1 summarizes the characteristics of each design.

The main challenge that impedes wide commercialization of SOFCs is the reduction of high cost of materials and processing. Towards that end, extensive research efforts have been focused on the reduction of operating temperature of these devices that would enable a relaxation of materials selection requirements and thus the use

Table 1.1: Characteristics of SOFC designs.

Support	Advantages	Disadvantages	Ref.
Cathode	<ul style="list-style-type: none"> <li>• redox stability</li> <li>• low cost</li> <li>• thin electrolyte</li> <li>• tolerant to carbon deposition</li> </ul>	<ul style="list-style-type: none"> <li>• moderate power densities</li> <li>• higher polarisation resistance</li> <li>• difficulty in processing</li> <li>• limited gas diffusion</li> <li>• weaker mechanical support</li> </ul>	[14–24]
Anode	<ul style="list-style-type: none"> <li>• higher power densities</li> <li>• thin electrolyte</li> <li>• ease of processing at high Temp.</li> <li>• lower polarisation resistance.</li> <li>• stronger mechanical support</li> </ul>	<ul style="list-style-type: none"> <li>• limited gas diffusion</li> <li>• susceptible to mechanical failure due to redox instability</li> <li>• high cost</li> </ul>	[25–30]
Electrolyte	<ul style="list-style-type: none"> <li>• thin electrodes</li> <li>• robust mechanical stability</li> </ul>	<ul style="list-style-type: none"> <li>• higher ohmic resistance at low operating temp.</li> <li>• thick electrolyte</li> <li>• high cost</li> </ul>	[31]
Metal	<ul style="list-style-type: none"> <li>• thin fuel cell components</li> <li>• stronger mechanical support</li> <li>• thermal shock tolerant</li> <li>• low cost</li> </ul>	<ul style="list-style-type: none"> <li>• susceptible to oxidation</li> <li>• difficulty in processing</li> </ul>	[32–35]

of cost-effective materials for sealing and interconnection. In addition, operation within this temperature range extends the lifetime of the cells and thus, durability of the stack is improved [36,37].

The reduction of the operating temperature requires the use of either thin solid electrolytes (*i.e.*  $<10\ \mu\text{m}$ ) to reduce the ohmic losses of the cell or alternative materials with higher ionic conductivities. Figure 1.3 illustrates the ionic conductivity for several solid oxide electrolytes and the potential operating temperature as the thickness of the electrolyte is decreased. The state-of-the-art electrolyte for use in SOFCs is considered to be the YSZ. This extraordinary material offers excellent chemical compatibility with the vast majority of electrodes and it is stable in both reducing and oxidizing atmospheres. Moreover, is inexpensive and although exhibits a moderate ionic conductivity, in thin film form, it is suitable for operating temperatures reduced to  $600\ ^\circ\text{C}$ . Other oxygen ion-conducting materials such as gadolinia-doped ceria (GDC) although exhibit superior conductivities than YSZ, introduce new difficulties of electronic conductivity, chemical reactivity and general in processing (*i.e.* to obtain a dense microstructure) [38].

In figure 1.3 it is manifested that the area specific resistivity (ASR) for the YSZ electrolyte starts to become negligible at low temperatures when the thickness becomes  $< 15\ \mu\text{m}$ . However, electrode total polarization losses will be considerable at low temperatures often exceeding the ohmic losses and thus, to minimize the total ASR of the cell either alternative electrode materials or improved structures are needed [9].

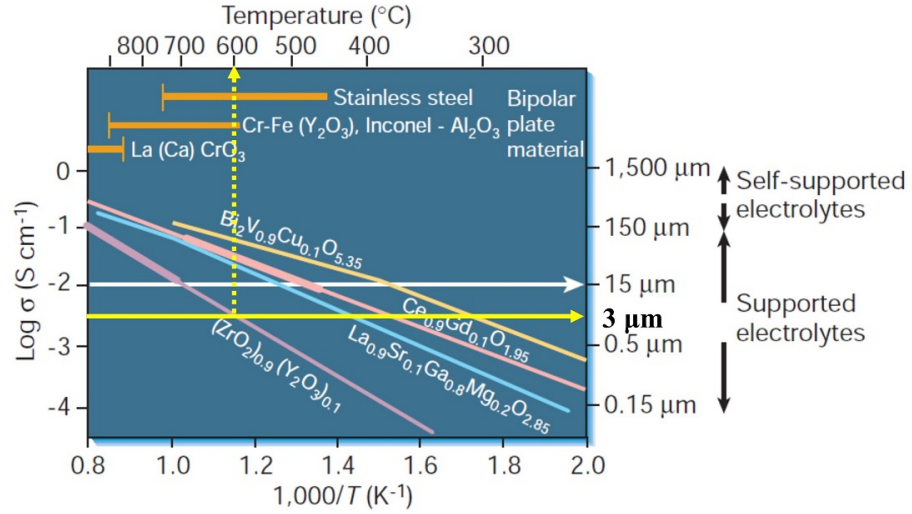


Figure 1.3: Conductivity of SOFC oxygen ion conductors versus reciprocal temperature and thickness, modified from [38]. The ASR for a 3  $\mu\text{m}$  YSZ electrolyte is  $\approx 0.08 \Omega \text{cm}^2$  at 600  $^\circ\text{C}$ .

## 1.4 Processing methods

Thin electrolytes are not mechanically robust by themselves and thus must be supported on a thicker porous substrate (*i.e.* electrode or metal, table 1.1). To succeed the challenging task to prepare a thinner and gas-tight electrolyte on porous support electrodes, various innovative processes have been developed [39]. These can be distinguished as conventional which are based on ceramic powder processing and deposition techniques which entail the formation of thin film SOFC components supported on porous substrates via physical or chemical processes. An overview of these methods is shown in figure 1.4.

In short, the physical deposition techniques include those of pulsed laser deposition (PLD), atmospheric plasma spray (APS) and physical vapor deposition (PVD). The chemical deposition techniques comprise those based on film deposition from

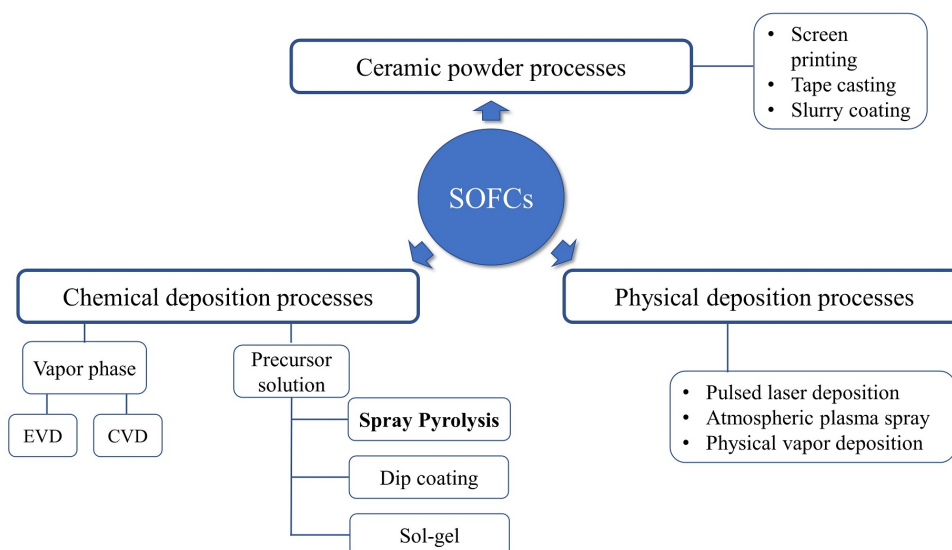


Figure 1.4: Processing methods for preparation of solid oxide fuel cells.

the vapor phase such as chemical vapor deposition (CVD), electrochemical vapor deposition (EVD) and from the precursor solution route such as dip coating, sol-gel and spray pyrolysis. The processing conditions in which the precursor materials are subject, in order to obtain desirable characteristics are significantly different from those encountered in a SOFC operating environment [40]. Therefore, each processing method should be chosen wisely based on the materials properties, target structure and their chemical compatibility. The leverage of the deposition techniques over the rival conventional ceramic techniques lies in the preparation of thinner films on different substrate geometries (*i.e.* tubular, planar) at reduced sintering temperatures. Siemens/Westinghouse successful cathode-supported tubular design with thin YSZ electrolytes prepared by EVD process is a good example [15]. On the other hand, the majority of the deposition techniques require expensive and complex equipment and thus, are not viable for large-scale mass production. However, from the family of these techniques spray pyrolysis due to its simplicity and low cost has attracted

considerable attention in SOFCs development, since Chamberlin and Skarman pioneered this technique [41].

## 1.5 Spray pyrolysis technique

Spray pyrolysis is a versatile and cost-effective technique that has been used to prepare thin films and powders for various applications in solar panels, thermal barrier coatings, batteries, solid oxide fuel cells and other [42, 43].

The process of spray pyrolysis involves atomization of a precursor solution into fine droplets sprayed onto a heated substrate. Once the droplets reach the substrate surface, thermal decomposition of the precursor occurs forming a thin oxide film. This process can be repeated in spray cycles increasing the thickness of the film while it can repair possible defects which formed in a previous cycle. An illustration of the spray pyrolysis process is shown in figure 1.5.

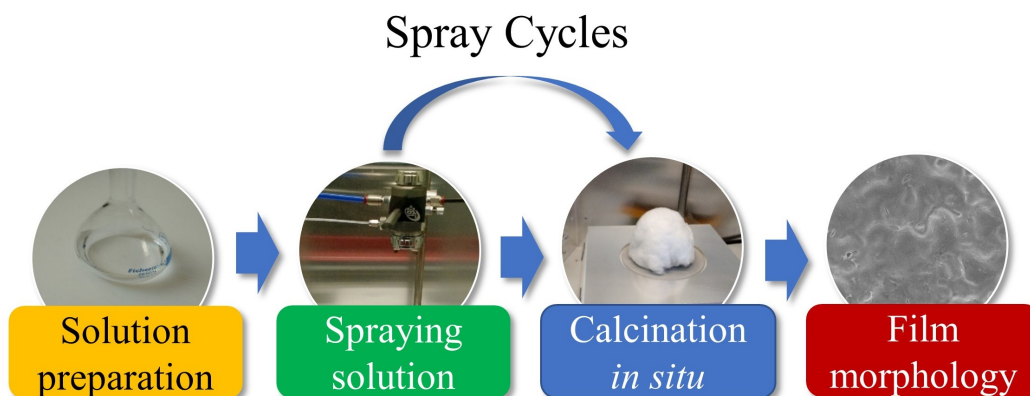


Figure 1.5: Process steps of spray pyrolysis technique.

Typically the equipment for the application of spray pyrolysis consists of a precursor solution pump, spray gun and a hot plate attached with a temperature controller. Based on the atomization technique used for solution aerosol formation, we can distinguish spray pyrolysis in three main varieties namely, air-pressurized, ultrasonic and electrostatic. These atomization techniques control the initial droplet size and size distribution as well as droplet velocity. Pneumatic spray nozzles are capable of atomizing large volumes of solution at high rates (*i.e.*  $>3$  ml/min) with a droplet size distribution of 10-100  $\mu\text{m}$ . However, as the air pressure increases this distribution becomes narrower. On the other hand, ultrasonic nozzles are able to produce a more uniform droplet size distribution and with smaller droplet size (*i.e.* 2-4  $\mu\text{m}$ ), but the atomization rate is limited up to 2 ml/min [44]. Similarly, electrostatic nozzles are able to produce small droplet sizes, but with controlled trajectory to the surface of the substrate, induced by an electric field and thus, with a higher deposition efficiency [45]. However, aqueous solutions are more difficult to be atomized due to the properties of the solvent (*i.e.* surface tension and conductivity) that cause electric disruptive discharges [46]. In addition, preferential landing of the charged droplets is favourable to prepare porous structures for electrodes but is more challenging to obtain a dense morphology suitable for electrolyte films [47]. Spray pyrolysis limitations include relatively low deposition rates, release of corrosive gases and low deposition efficiency in case of use of pneumatic and ultrasonic nozzles [48]. Moreover, all the components in the thin film form need a support that only can be made by conventional powder techniques (*e.g.* tape casting).

However, unlike other deposition techniques using vacuum systems (*e.g.* PVD) spray pyrolysis due to equipment simplicity can easily be scaled-up for processing films at an industrial level. Moreover, in contrast with most of solution-based pro-

cesses this technique combines precursor precipitation, thermal decomposition and sintering steps into a single process [44]. It should be noted, the latter applies only for *true* solutions and should be distinguished from spraying powder suspensions [36]. Furthermore, a wide range of available soluble precursors offers an easy way to deposit films of nearly any stoichiometry at droplet level with minimum impurities while moderate process temperatures also expands the range of substrates with less robust materials. Either multi-layered films or films with a gradient structure can also be obtained by simply changing the composition of the precursor solution. In general, the properties and features of the films are directly controlled from the process parameters (*i.e.* substrate temperature, precursor concentration, deposition time, gas flow rate, solution flow rate and nozzle-to-substrate distance) and the physicochemical characteristics of the precursor solution [49].

Various good reviews on thin film deposition techniques with emphasis on SOFC components have been published. Will *et al.* [39] give a description of processing techniques characteristics for deposition of gas-tight YSZ electrolytes either on dense or porous substrates. De Jonghe *et al.* [40] explore the economic viability of processing techniques for synthesis of supported electrolyte thin films. Perednis and Gauckler [42] describe the effect of spray pyrolysis process parameters on film properties demonstrating the significance of the optimization process. Beckel *et al.* [50] review the application of thin film deposition techniques and the geometric limits of deposited films for micro-SOFCs. The most recent review on spray pyrolysis and the critical process parameters that influence thin films morphology was published by Kiratzis [36].

Spray pyrolysis has attracted the interest of many researchers with the rise of the need to prepare thinner SOFC electrolytes and thus, reduce the operating tempera-

ture of the cells. This explains why the vast majority of this work has been focused on the challenging task to produce a thin and gas-tight electrolyte layers [51–61] although cathode [62–64] and anode [65–67] electrodes have also been produced by this technique with promising performance. It is noteworthy, that only a limited number of reports, shown in table 1.2, have demonstrated electrochemical results on SOFCs with thin electrolytes prepared by spray pyrolysis indicating the challenging task of process optimization.

Table 1.2: Performance of SOFCs with supported thin electrolytes prepared by spray pyrolysis.

Substrate support	LSM	Ni-YSZ	Ni-YSZ	SS-430
Substrate porosity [%]	17	26/40	-	-
Electrolyte	CSZ	YSZ/CYO	CGO	SDC
Electrolyte thickness [ $\mu\text{m}$ ]	33	0.4-0.8	3.3	5
Anode	Ni-YSZ	supported	supported	Ni-SDC
Cathode	supported	LSCF	SSC/SDC	SSC/SDC
Fuel	H <sub>2</sub>	H <sub>2</sub>	H <sub>2</sub>	H <sub>2</sub>
Operating temperature [ $^{\circ}\text{C}$ ]	1000	770	650	600
OCV [V]	0.96	1.01	0.71	$\approx 0.67$
Max.power density[W/cm <sup>2</sup> ]	0.5	0.76	0.51	$\approx 0.09$
References	[14]	[25]	[26]	[32]

## 1.6 Aim of the thesis

The aim of this study was to develop a spray pyrolysis technique for preparation of ultra-thin and gas-tight film electrolytes (*i.e.*  $< 5 \mu\text{m}$ ) supported on cathode electrodes at low sintering temperatures ( $< 1000^{\circ}\text{C}$ ). It was also contemplated to identify the process parameters with the greatest effect on film morphology, electrochemical performance and long term durability of cathode-supported SOFCs.



# Chapter 2

## Materials and thin films characterisation techniques

Sophisticated preparation techniques such as spray pyrolysis can produce thin films with unique structural features and electrochemical performance [68]. Utilising analytical techniques for characterisation of thin films can give a more in-depth understanding of the fabrication process parameters and their effect on the properties of the films in terms of microstructure and electrical performance. For example electron microscopy can provide useful information regarding the growth mechanism and the existence of potential structural defects of the films. In this chapter is given a detailed description of the experimental techniques used to prepare and characterise the deposited films.

### 2.1 Spray pyrolysis apparatus

For spray pyrolysis application in thin films the experimental apparatus illustrated in figure 2.1 was used. The system was assembled from an infusion pump (Harvard-apparatus 22), a mass flow controller (Uniflux, Cache Ltd), an industrial automatic

spray gun (DeVilbiss AG-361, with a 0.85 mm fluid tip and a TE10 air cap), a relief pressure valve, a ceramic hot plate (Technico) and a homemade spraying booth (40x40x60 cm).

To eliminate the cooling effect of the air flow that restricts a high substrate temperature spray deposition was carried out in intermittent cycles. The spray gun as shown in figure 2.2a has three parts (i.e. ATOM and FAN air valves, needle adjustment knob) to be properly adjusted in order to produce a fine aerosol with a circular spraying pattern. For a precursor solution flow rate up to 1.5 ml/min the needle knob was placed at the 2<sup>nd</sup> position out of 18. The ATOM valve was fully opened, and the FAN valve was fully closed. The atomising air flow was accurately regulated by a mass flow controller at 30 L/min. To trigger the spraying gun an air pressure of 5 bar was applied. The spray gun was earthed and mounted on a metallic rod to dissipate any electrostatic charges caused by either air or liquid flow [69]. The distance between the spray gun tip and the substrate was 25 cm. Application of the above settings resulted to a circular spraying pattern of 5 cm in diameter as shown in figure 2.2b. To achieve a good thermal contact the surface of the substrates needs to be as flat as possible including the surface of the supporting plate which can be polished prior the spraying deposition. Opposite of meeting this requirement can result in moving substrates outside the spraying pattern during the deposition cycle.

Prior to every spraying cycle the substrate was heated by a hot plate at 540 °C for 20 min. An aluminium plate (Ø100 mm, thickness 3 mm) was placed underneath the substrates to protect the surface of the hot plate and to ensure temperature homogeneity over the substrate positions. Since the entire process takes place under open atmosphere the substrates were covered by an alumina crucible and glass wool to ensure a high uniform temperature. At the end of dwell time the temperature

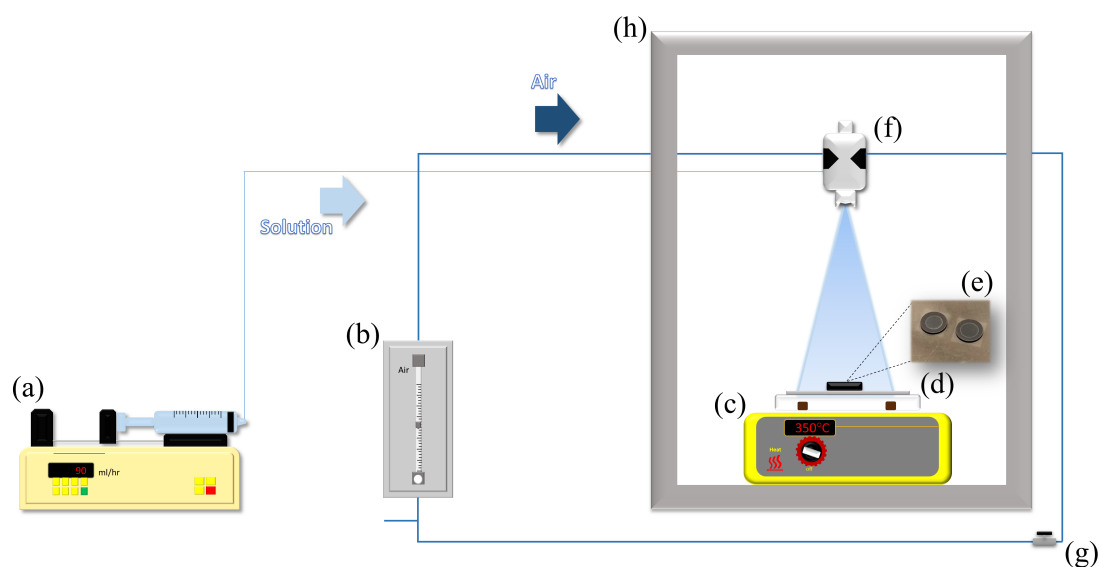


Figure 2.1: Spray pyrolysis apparatus where a) Infusion pump, b) Air flow controller, c) Hot plate, d) Aluminium plate, e) Substrate, f) Spray gun, g) Relief pressure valve, h) Spraying booth.



(a) Spray gun air valves and needle knob. (b) Spray deposition pattern formed at 25 cm operating distance.

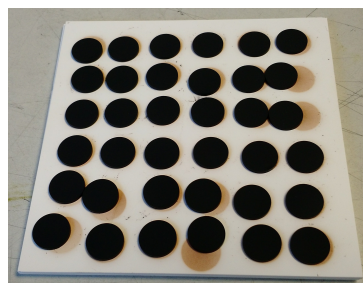
Figure 2.2: Automatic spray gun DeVilbiss AG-361 and coating pattern.

of the hot plate was adjusted accordingly. Afterwards, the glass wool was removed and the spray gun was triggered with only air to flow for 5 min on the crucible and for 2 min on the substrates. The temperature of the substrate was measured with a type K handheld surface thermocouple (GOF500, GHM-Greisinger, Germany). Immediately after the precursor solution was fed with a flow rate controlled by an infusion pump to the spray gun. An aerosol was produced directed to the heated substrates followed by thermal decomposition of the salts and forming a thin oxide film. To complete the spraying deposition the syringe pump was stopped and the air stream was initially blocked and stopped to avoid formation of agglomerates on the surface of the films caused by residual sprayed solution. The synthesised films were calcined *in situ* on the hot plate for an hour and subsequently post-sintered in a muffle furnace (Carbolite) within a temperature range of 750-900 °C to complete the sintering process.

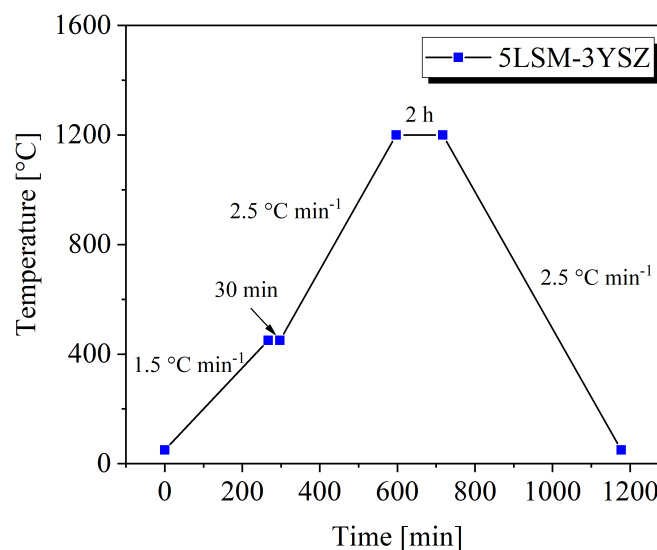
## 2.2 Substrate preparation

Composite cathode electrodes were used as substrates (figure 2.3a) for spray deposition of thin electrolyte films. Starting ceramic powders of LSM and YSZ were pre-treated by roll milling before pressed into pellets and sintered. In detail, ceramic powder of 5% A-site deficiency LSM (Pi-Kem ltd) was presintered at 800 °C with dwell time of one hour and heating-cooling rate of 3 °C/min to increase the particle size. To break formed agglomerates after the thermal treatment the LSM powder was sieved through a stainless-steel mesh(106 µm).

Aqueous dispersions of ceramic powders of either 3 mol % YSZ or 8 mol % YSZ and pre-treated 5LSM were roll milled in a polyethylene bottle (125 ml) with disper-



(a) Composite substrates after sintering.



(b) Sintering profile of composite substrates (1200 °C and dwell time of 2 h).

Figure 2.3: 5LSM-3YSZ substrates in a button cell geometry (thick.1 mm, Ø 11 mm) and sintering profile.

sant, de-foaming agent and pore former at 160 rpm for five hours. This was followed by the addition of a binder and subsequent roll milling for one hour. Additional deionized water was added to recover residue material from the inside of the bottle and poured into a glass beaker where it was left inside a fume cupboard overnight to dry. A detailed description of the quantities of the materials and characteristics is given in table 2.1. The resulting powder was pressed into pellets at 147 MPa for 35 sec using stainless steel dies of 12 mm and a manual hydraulic press (Specac Atlas 15t). Afterwards, the pellets were placed between porous alumina plates and sintered in a muffle furnace (Carbolite) at 450 °C for 30 min to burn the pore former and at 1200 °C for 2 h (figure2.3b) to complete the thermal treatment. Pellets with sufficient mechanical strength and flat surface were produced. Porosity of the pellets was measured by the Archimedes method and image processing of scanning electron

microscopy (SEM) photos using ImageJ software. Morphology was examined by SEM. Conductivity measurements were performed by four-point DC conductivity.

Table 2.1: Aqueous dispersion composition and stages of roll milling.

Material	Composition [wt%]	Role	Supplier
$(\text{La}_{0.8}\text{Sr}_{0.2})_{0.95}\text{MnO}_3$	90	powder	$\pi$ -Kem
$(\text{Y}_2\text{O}_3)_{0.03}(\text{ZrO}_2)_{0.97}$	10	powder	Tosoh
$(\text{La}_{0.8}\text{Sr}_{0.2})_{0.95}\text{MnO}_3$	50	powder	$\pi$ -Kem
$(\text{Y}_2\text{O}_3)_{0.08}(\text{ZrO}_2)_{0.92}$	50	powder	Tosoh
PMMA (325 nm)	15*	pore former	Soken ltd
32 zirconia balls ( $\text{Ø}10$ mm)	-	milling	-
1 <sup>st</sup> stage of roll milling, 5 h at 160 rpm			
Triton QS-44	3.5*	dispersant	Dow
DF002	0.6*	de-foaming agent	Haiku Tech
2 <sup>nd</sup> stage of roll milling, 1 h at 160 rpm			
Decoflux WB-41	5.0*	binder	Zchimmer Schwarz

\* wt% of total ceramic powders.

## 2.3 Precursor solution preparation

Aqueous precursor solutions were prepared for spray deposition of thin film SOFC components. Table 2.2 gives a summary of the salts used for the synthesis of each component. Metal nitrates are cost effective, highly soluble in water and exhibit relatively low decomposition temperatures. Thus, the appropriate precursors were dissolved in deionised water according to the stoichiometry of the target material. Relatively, concentrated solutions of 0.1 mol/l were used for spray deposition of dense electrolyte films while diluted solutions of 0.005 mol/l were used for spray deposition of porous electrode films.

Table 2.2: Aqueous precursor solutions.

Material	Precursor	Purity [%]	Supplier
$Y_{0.16}Zr_{0.92}O_{2-\delta}$	$Y(NO_3)_3 \cdot 6 H_2O$	99.9	Fisher Scientific
	$ZrO(NO_3)_2 \cdot 6 H_2O$	99.5	Fisher Scientific
$Gd_{0.1}Ce_{0.9}O_{1.95}$	$Gd(NO_3)_3 \cdot 6 H_2O$	99.9	Fisher Scientific
	$Ce(NO_3)_3 \cdot 6 H_2O$	99	Sigma Aldrich
Co–CeO <sub>2</sub> , (50:50 vol %)	$Co(NO_3)_2 \cdot 6 H_2O$	98	Sigma Aldrich
Ni–YSZ <sup>1</sup> , (40:60 vol %)	$Ni(NO_3)_2 \cdot 6 H_2O$	99	Fisher Scientific
$La_{0.8}Sr_{0.2}MnO_3$	$La(NO_3)_3 \cdot 6 H_2O$	99.9	Alfa Aesar
	$Sr(NO_3)_2$	99	Sigma Aldrich
	$Mn(NO_3)_2 \cdot xH_2O$	99.98	Alfa Aesar

<sup>1</sup> The same metal nitrates were used as for the  $Y_{0.16}Zr_{0.92}O_{2-\delta}$

## 2.4 Thermal analysis (DTA/TG)

Two of the most significant methods of thermal analysis are thermogravimetric analysis (TGA) in which the mass change of a substance is measured as a function of temperature increase or time, and differential thermal analysis (DTA) [70]. The latter is a measurement of temperature difference  $\Delta T$  between the sample and an inert reference material as a function of time. In DTA, the measured temperature of the sample and the reference should be the same ( $\Delta T = 0$ ) until a physico-chemical event (e.g. desorption, decomposition) takes place. During an exothermic event the temperature of the sample will exceed the reference's temperature while for an endothermic event will lag behind [71]. Ultimately, analysis of the DTA curve plotted against time will reveal either exothermic events appearing as crests or endothermic events observed as troughs.

Due to a different thermal behaviour of the starting metal nitrates and a precursor solution of these compounds, DTA/TG analysis was conducted for each case

separately [72]. Metal nitrates used for preparation of the precursor solutions were first analysed to determine accurately the stoichiometric water content, since these compounds are highly hygroscopic exhibiting a deviation of the labelled formula weight. Subsequently, an aqueous precursor solution was prepared and sprayed on a glass substrate. The recovered powder was analysed using a NETZSCH STA 449C Jupiter<sup>®</sup> analyser. Typically, samples were placed in an Al<sub>2</sub>O<sub>3</sub> crucible and heated up to 900 °C with a heating rate of 5 °C/min or 10 °C/min and air flow rate of 40 ml/min while any mass change was recorded. From the produced TGA plots decomposition temperature was determined giving an indication of the minimum post-sintering temperature that should be adopted to obtain stable crystalline films.

## 2.5 X-ray diffraction

X-ray diffraction (XRD) is one of the dominant analytical techniques to determine the crystalline phases of materials. The Braggs approach makes the assumption the crystal is built up in atomic planes which act as a mirror. Incident X-ray beams reflect upon these planes and interfere. Diffraction occurs when constructive interference of the X-rays takes place.

This is depicted in figure 2.4 where two parallel X-ray beams labelled 1' and 2' are in phase to satisfy the condition where the path length differences of the two X-rays must be equal to a whole number ( $n = 1, 2, 3, \dots$ ) of wavelengths [73]. These are related by:

$$n\lambda = \overline{AB} + \overline{BC} \quad (2.1)$$

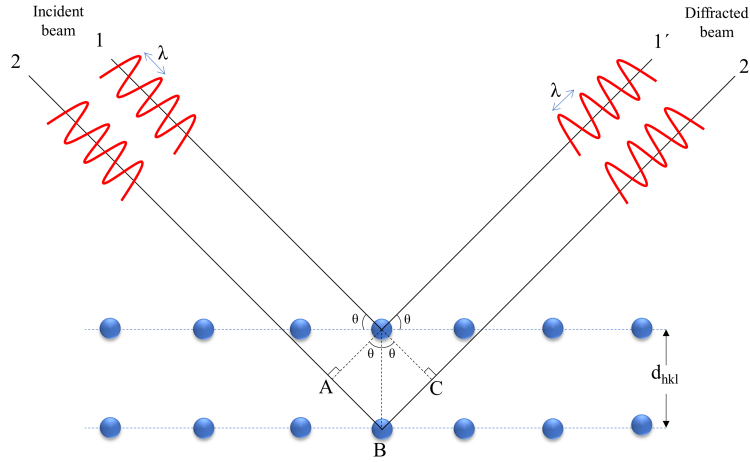


Figure 2.4: Schematic illustration of diffraction of X-rays by crystals

Therefore

$$\begin{aligned} n\lambda &= d_{hkl} \sin \theta + d_{hkl} \sin \theta \\ &= 2d_{hkl} \sin \theta \end{aligned} \quad (2.2)$$

Equation 2.2 represents Bragg's law where  $d_{hkl}$  is the space between the planes,  $\theta$  is the incident angle to an atomic plane and  $\lambda$  is the wavelength of the X-rays [74]. In case interference of the X-rays is destructive Bragg's law is not satisfied, resulting in a low intensity diffracted beam. Given the interplanar spacing  $d_{hkl}$  from Bragg's law, the unit cell parameter(s) of a crystal system can be calculated by a plane-spacing equation. For instance, for a cubic structure the corresponding equation will be:

$$d_{hkl} = \frac{\alpha}{\sqrt{h^2 + k^2 + l^2}} \quad (2.3)$$

where  $\alpha$  is the lattice parameter and  $h, k, l$  the Miller indices [73]. Similar equations exist for the rest of the crystal systems to calculate the unit cell parameter(s).

The first X-ray spectrometer was prototyped by W.H. Bragg and notably improved by M. Siegbahn [75]. The basic components of an X-ray spectrometer to conduct a measurement are limited to an X-ray source, the specimen holder and a detector which measures the intensity of the diffracted X-rays [71]. A simplified schematic of a diffractometer is illustrated in figure 2.5.

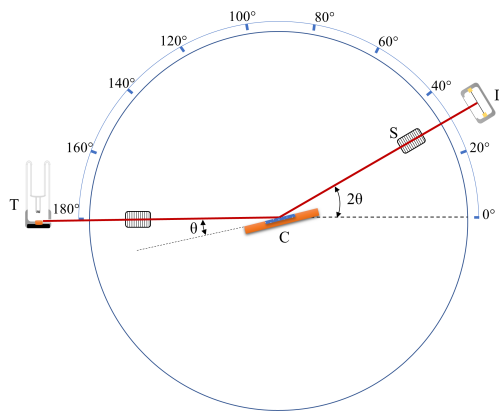


Figure 2.5: Basic arrangement of X-ray diffractometer components. T is the X-ray source, D is the detector, C the sample holder and S the divergent slits

Under operation, X-rays generated by collision of accelerating electrons with a metal target (e.g. Cu, Mo etc.) are incident on the specimen which rotates at different angles. Any intensities of diffracted X-rays which satisfy Bragg's law are detected by a counter and plotted as a function of  $2\theta$ . Investigation to determine formed crystal phases of the prepared thin films was carried out on an X-ray diffractometer (Panalytical Empyrean Alpha-1) using  $\text{CuK}\alpha$  radiation (20 kV, step size 0.02, scan rate 0.5 min<sup>-1</sup>,  $20^\circ < \theta < 90^\circ$ ) in Bragg-Brentano geometry.

For the analysis of measured X-ray diffractograms STOE WinX<sup>POW</sup> software was used. Additional information about the grain size and lattice strain of the thin films was estimated by the Debye-Scherrer formula and the Williamson-Hall (W-H)

method [76].

$$D = \frac{K\lambda}{\beta_{hkl} \cos \theta} \quad (2.4)$$

where  $D$  is the grain size,  $K$  the particle shape factor (0.9),  $\lambda$  the wavelength,  $\beta_{hkl}$  the full width at half maximum of the peak and  $\theta$  the diffraction angle. More specifically correction of the instrumental broadening was calculated by the following relation

$$\beta_{hkl} = [(\beta_{hkl})_{measured}^2 - (\beta_{hkl})_{insturmental}^2]^{1/2} \quad (2.5)$$

Considering that the grain size and micro-strain ( $\varepsilon$ ) are independently contributing to peak broadening the observed peak breadth can be expressed as

$$\beta_{hkl} = \frac{K\lambda}{D \cos \theta} + 4\varepsilon \tan \theta \quad (2.6)$$

or

$$\beta_{hkl} \cos \theta = \frac{K\lambda}{D} + 4\varepsilon \sin \theta \quad (2.7)$$

The micro-strain and the grain size was calculated more accurately by W-H plots of  $4 \sin \theta$  ( $x$  axis) and  $\beta_{hkl} \cos \theta$  ( $y$  axis). From a linear fitting of the data the  $y$ -intercept corresponds to the grain size and the slope of the fit to the micro-strain [76].

## 2.6 Scanning electron microscopy

Scanning electron microscopy (SEM) is one of the most versatile methods for structural and chemical analysis of materials [77]. Interaction of accelerated electrons

with the specimen is being utilized to produce images exceeding in resolution those produced by light microscopy [78]. Light microscopy is limited in resolution of approximately  $0.1\ \mu\text{m}$ , due to the wavelength  $\lambda$  range of visible light spectra (i.e. 400-700 nm). However, types of radiation with shorter wavelengths that lie within ultraviolet and X-rays range produce images of higher resolution [79]. The key parts of an SEM are illustrated in figure 2.6. A typical SEM microscope comprises a source of electrons (e.g. tungsten filament), column with electromagnetic lenses, suitable signal detectors, specimen chamber and a computer with an appropriate software for analysis and data recording.

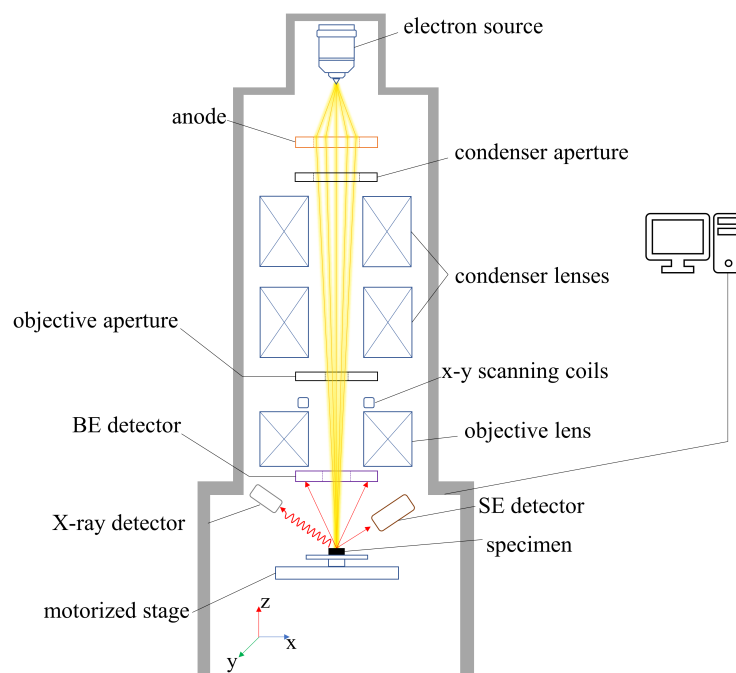


Figure 2.6: Schematic drawing of main components of an SEM microscope [79].

In principle, upon impact of an incident electron beam with a specimen, under vacuum, different signals will be emitted which are detected and used to form images of examined areas of the specimen. A summary of the produced signals is illustrated

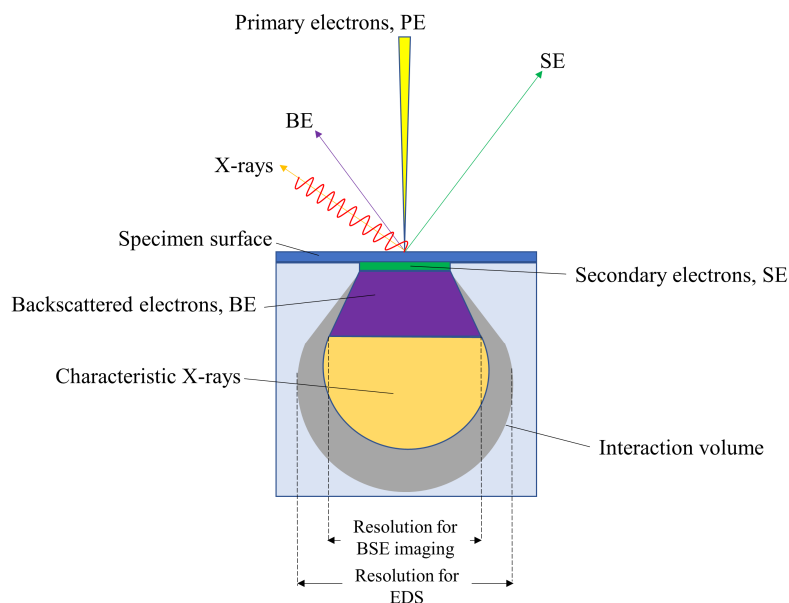


Figure 2.7: Types of signals emitted upon impact of incident electron beam with a specimen [77].

in figure 2.7. Based on the types of the signals we distinguish produced images of secondary electrons (SEs), backscattered electrons (BEs) and X-ray elemental maps. The origin of secondary and backscattered electrons is inelastic (i.e. loss of energy) and elastic scattering respectively of the primary electrons. In general, SEs possess a relative low energy of 3-50 eV escaping from a shallow region close to the surface. Therefore, these are usually exploited to form images of actual topographic contrast. On the other hand, BEs have a greater energy compared to SEs escaping from specimen regions of greater depth and providing information of compositional contrast based on the atomic number of the elements [80]. Images of BEs will reveal distinctive boundaries of heavier elements with a higher brightness and elements of lower atomic number and lower brightness [78].

Usually in conventional SEM microscopes a tungsten filament in a V shape is

being used as an electron source due to its low cost. However, when imaging of even higher resolution is needed using an electron source of a field emission gun (FEG) is more suitable. In general the same principles in SEM apply also to FEG-SEM. The difference lies in the shape of the tungsten filament which is a pointed sharp tip resulting to a much smaller electron probe and consequently to a higher resolution imaging [78]. Among the different types of FEG, cold field emission (CFE) can function at room temperature and basically depends on the electric potential difference of the electrodes. The small surface area of the electron beam and the emission area enables high brightness at low current of the incident electron beam. Nevertheless, one of the limitations of CFE is the formation of absorbed gas layers on the tip of the FEG which interfere with the current emission causing instability. A solution to remove residue gas layers is to heat the tip at a very high temperature for a very short time, a process better known as flashing [78].

Specimen preparation is essential for electron microscopy. For instance, samples which are not sufficiently conductive tend to accumulate a negative charge. As a result incident and emitted electrons start to deflect disturbing the image formation. Coating a thin conducting layer of gold or carbon can prevent this effect [80]. However the thickness of the conducting layer should not be too thick to cover structural features of the sample or too thin with uncovered charging areas [81]. In addition, for cross-sectional imaging of samples with unique characteristics such as thin films a focused ion beam (FIB) is usually employed to make a clean cut of the specimen. In detail, as a specimen preparation mechanism FIB uses a beam of gallium ions emitted by a liquid-metal ion source which is focused on the area of interest by electrostatic lenses. The beam removes atoms from the sample surface, line-by-line, making a clean cross-section cut [77]. Moreover, fractured surfaces in some cases

can also be representative cross-sections of a sample. A smooth cross-section reveals various structural features of the films such as the thickness of the film, porosity or potential existing defects. Further processing by FIB can also thin down to electron transparency a region of interest from the sample to prepare a lamella suitable for observation by transmission electron microscopy (TEM) [77].

### 2.6.1 Energy dispersive X-ray spectroscopy

Energy dispersive X-ray spectroscopy (EDS) is being used to estimate elemental composition of a substance. In principle, when primary electrons bombarding a specimen, electrons orbiting around atomic nucleus are being removed from their inner shell leaving behind an electron vacancy which is filled by an electron of higher energy [82]. This transition of electrons cause emission of characteristic X-rays as shown in figure 2.8.

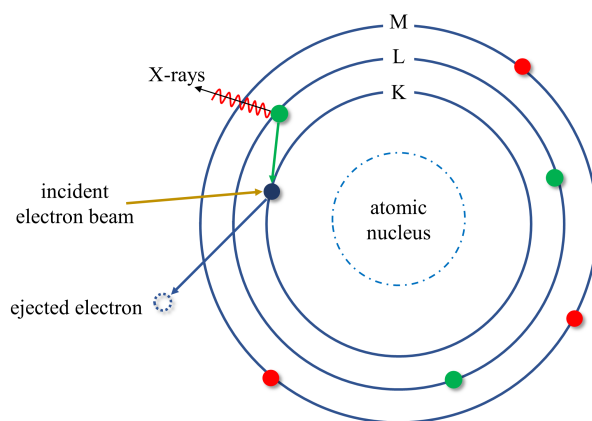


Figure 2.8: Schematic illustration of EDS principle [77].

Detection of the X-ray spectra is carried out by a dispersive X-ray energy spectrometer employing a solid-state detector (e.g. Si(Li)) [82]. Analysis of the X-ray peaks results into identification of the elements by comparison of their energy with

elemental standards [79].

Analysis of the specimens was performed by a SEM JEOL 5600 microscope coupled with an EDS Oxford Inca Energy 200 system and a FEG-SEM Jeol 6700 microscope. For certain samples a FEI Scios FIB-SEM was used to prepare cross-sections of the deposited thin films.

## 2.7 Transmission electron microscopy

Transmission electron microscopy (TEM) is a powerful analytical technique for characterisation of nanostructured materials such as powder particles and thin films [79]. The main components and the ray path for a TEM microscope are illustrated in figure 2.9 [81]. Under operation, an electron beam is generated by a heated electron-emitting cathode typically made of  $\text{LaB}_6$ . Emitted electrons in order to obtain sufficient energy and pass through an ultrathin (i.e.  $\leq 100$  nm) specimen are accelerated by a high voltage (i.e. 80–300kV). The accelerated electron beam then is focused by a set of condenser lenses placed before the specimen. Afterwards, transmitted electrons passing through the specimen are refocused by the objective lenses to produce the diffraction pattern and an image in the back focal plane. Projector lenses are set accordingly for signal magnification based on whether a diffraction pattern or an image is to be analysed [83]. A phosphorescent screen is being used to convert incident electrons to a live image. Recording of the images or the diffraction patterns can be accomplished by either using photographic film or electronically via digital charge-coupled (CCD) devices connected to a computer with a suitable software [79].

Various TEM modes are used to characterise a specimen based on the type

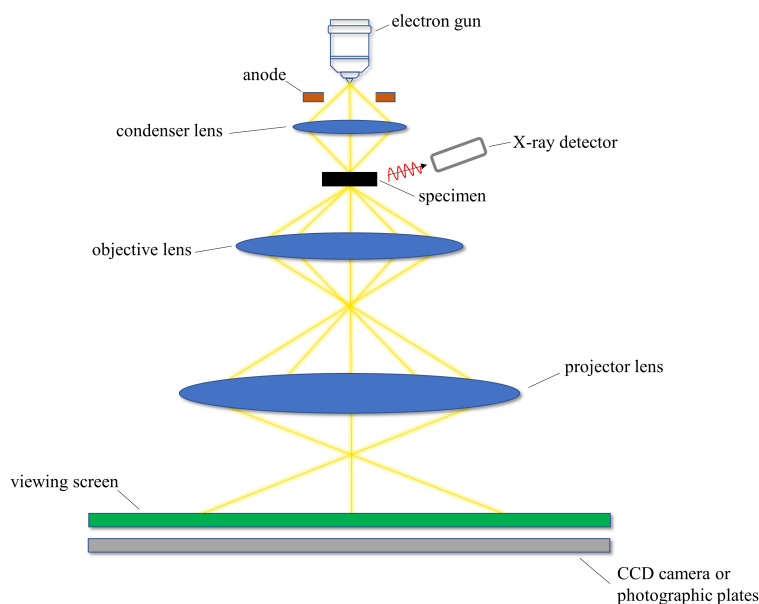


Figure 2.9: Schematic drawing of key components and ray diagram of a TEM microscope [79, 81].

of the analysis (e.g. structural or chemical). For bright field (BF) imaging only transmitted electrons passing through the objective aperture are used to form a BF image reflecting structural features of the specimen. One of the most useful TEM modes is the electron diffraction. In this mode, elastically scattered electrons are used to form a diffraction pattern, similarly with X-ray diffraction, while transmitted electrons are blocked by the objective aperture. The diffraction pattern will appear as arrays of dots for a single crystal or concentric rings for a polycrystalline or an amorphous specimen. Elemental analysis can also be performed by EDS analogous to scanning electron microscopy. However, spatial resolution of measuring X-rays is superior than SEM due to the small thickness of the sample compared to the interaction volume used in SEM [79, 84]. Preparation of the samples prior TEM analysis was performed using FEI Scios FIB-SEM. Produced thin specimen analysed

using a FEI Titan themis 200 TEM microscope with a resolution of 0.24 nm.

## 2.8 Particle size analysis

One of the most useful techniques to estimate particle size distribution is laser diffraction (LD) [85]. The application of this technique is based on scattering of an incident laser beam by suspended particles, with suitable detectors measuring angular scattering intensity signals [86]. Signal conversion to size evaluation is based on Mie theory which considers particles as perfect spheres. Related to the particle size, scattering of the beam will be more intense at small angles for larger particles while for smaller particles will be weaker at large angles. Data of particle size distribution are usually expressed in d10, d50 and d90 values, corresponding to average volume percentages [85].

Particle size analysis of ceramic powders used for substrates preparation was conducted using a particle size analyser (Mastersizer 2000, Malvern instruments ltd). Preparation of the samples included powder suspension in deionised water with the addition of a dispersant (Triton QS-44). Ultrasonic agitation was performed for a limited time to break existing agglomerates prior of the measurements.

## 2.9 Electrochemical characterisation

### 2.9.1 Electrochemical test apparatus

Electrochemical testing of prepared cathode supported SOFCs was conducted in the experimental apparatus illustrated in figure 2.10. The system comprises three alumina tubes (O.D.12 mm, 5 mm(2)) fitted to stainless steel parts (swagelok) for

direct gas supply to the fuel cell, a handcrafted ceramic cup (macor) to properly align the top alumina tube, two rotameters (Uniflux, Cache ltd), a probe thermocouple, a metallic weight for sealant compression and a vertical tubular furnace with a temperature controller (Carbolite).

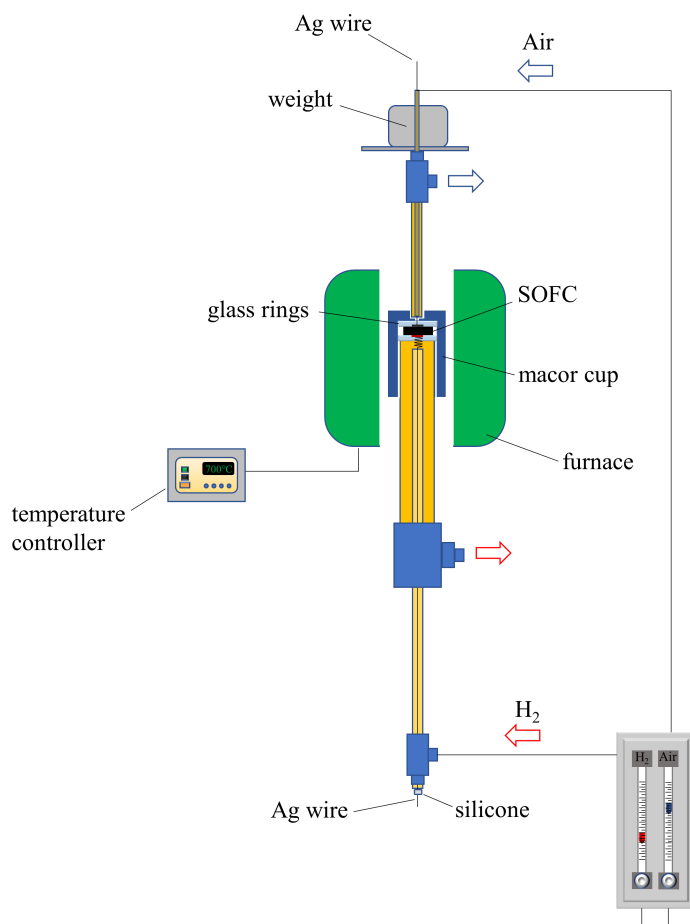


Figure 2.10: Schematic drawing of SOFC test apparatus

Initially, gold or silver paste was applied using a painting brush onto the electrodes of the fuel cell to improve current collection. The layers were subsequently fired at 540 °C for 30 min and at operating temperature. Nickel mesh was placed on top of the inner alumina tube to support a silver wire (Ø0.020 mm, Agar scientific)

spiral in contact with the anode electrode (figure 2.11a). The button fuel cell was sealed at one end of the alumina tube using pyrex glass rings ( $\text{\O}12\text{ mm}$ , Multi-lab ltd) as shown in figure 2.11b. A probe thermocouple was placed close to the fuel cell for accurate measurement of the operating temperature. To complete the setup a macor cup was placed on top of the fuel cell fitted with an alumina tube to supply air and electrical insulation to the silver wire in contact with the cathode (figure 2.11c). Under operation the fuel cell was heated at operating temperature with  $5\text{ }^{\circ}\text{C}/\text{min}$  to soften the glass rings while a metallic weight was placed on the upper part of the system to compress the rings and seal the fuel cell. The anode was reduced at  $500\text{ }^{\circ}\text{C}$  under 5% hydrogen diluted in argon while air was flown at the cathode. During operation flow rates of the gases were controlled by suitable rotameters (Uniflux, Cache ltd). A potentiostat-galvanostat (Solatron 1287) and a frequency response analyser (Solatron 1255) were used for electrical measurements in terms of I-V plots, open circuit voltage OCV and impedance spectroscopy operated with CorrWare<sup>®</sup> and Zview<sup>®</sup> software.



(a) Spiral of silver wire for anode electrical contact      (b) SOFC placed between pyrex glass rings      (c) Macor<sup>®</sup> cup with fitted alumina tube

Figure 2.11: SOFC sealing and electrical contacts

### 2.9.2 AC Impedance spectroscopy

Electrochemical impedance spectroscopy (EIS) is a well established technique for analysis of electrochemical properties of SOFC components and their interfaces. During an EIS measurement a frequency response analyser (FRA) applies a sinusoidal voltage signal of small amplitude (i.e. 10-50 mV) over a wide range of frequencies to a fuel cell and measuring an alternating current signal output. Impedance of SOFCs is usually measured within a frequency range of 0.01 Hz to 1 MHz but with a small amplitude to fulfil the requirement for a pseudo-linear response [87]. Mathematical relationships between the two signals are described as follows to calculate the impedance [88]. The applied excitation signal to the cell is expressed as:

$$E(t) = E_o \sin(\omega t) \quad (2.8)$$

where  $E_o$  is the amplitude of the signal and  $\omega$  is the angular frequency, ( $\omega = 2\pi f$ ).

In a pseudo-linear response, the alternate current is expressed as:

$$I(t) = I_o \sin(\omega t + \phi) \quad (2.9)$$

where  $\phi$  represents the difference in phase angle between current ( $I$ ) and voltage ( $E$ ) and  $I_o$  the signal amplitude.

Taking into account Ohm's law and equations (2.8, 2.9) a first expression of impedance  $Z$  is:

$$Z = \frac{E(t)}{I(t)} = \frac{E_o \sin(\omega t)}{I_o \sin(\omega t + \phi)} = Z_o \frac{\sin(\omega t)}{\sin(\omega t + \phi)} \quad (2.10)$$

Employing Euler's formula  $e^{ix} = \cos x + i \sin x$ , impedance in a complex notation

is given by:

$$Z(\omega) = \frac{E_o e^{i\omega t}}{I_o e^{i(\omega t + \phi)}} = Z_o e^{i\phi} = Z_o (\cos \phi + i \sin \phi) = Z_{re} + i Z_{im} \quad (2.11)$$

where  $Z_{re}$  and  $Z_{im}$  represent the real and imaginary parts of the impedance. Graphic representation of these two parts for different values of  $\omega$  is given in a Nyquist plot shown in figure 2.12a. However, in this type of plot the missing information are the frequency values. Complementary Bode plots (fig. 2.12b) give frequency values plotted against the magnitude of impedance  $|Z|$  and phase angle  $\phi$ . Thus, often to get a better understanding of the EIS both types of plots are presented together (fig. 2.12) [87].

Interpretation of impedance data involves the use of equivalent electrical circuit models fitting the measured EIS-data. Such models consist from resistive and reactive (capacitive, inductive) components connected in series or in parallel or even in subcircuits of both. Impedance of modeling elements used to built an equivalent circuit is given in table 2.3. Basically, these circuits simulate electrochemical processes taking place within the fuel cell in real time under a given excitation signal. Isolation of different electroactive regions of the fuel cell can be implement by estimation of their electrical relaxation time or time constant  $t$  [89]. For example for each parallel RC element shown in figure 2.12a it is calculated from equation 2.12.

The Nyquist plot in figure 2.12a is simulated from the equivalent circuit of two parallel RC elements and an R element in series. From the characteristic semicircles, values of the R and C elements can be obtained. The intercept of the  $Z_{re}$  axis gives the R value and by using equation to the frequency ( $\omega_{max}$ ) at the maximum of the semicircle gives C value. Based on the value of the capacitance listed in table 2.4

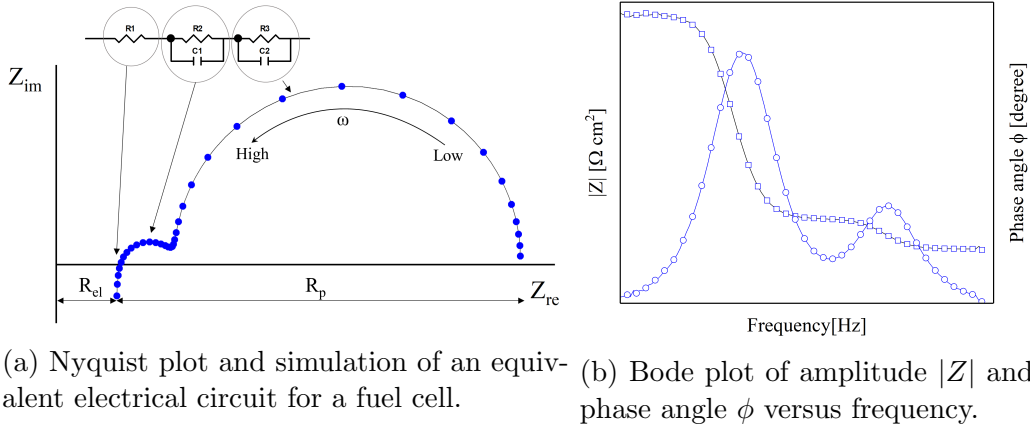


Figure 2.12: Typical EIS impedance plots for a solid oxide fuel cell.

enables to distinguish the dominant electrochemical process [89].

$$\tau = RC = \frac{1}{\omega_{max}} \quad (2.12)$$

However, under real operating conditions of a fuel cell interpretation of EIS-data is convoluted with depressed or overlapping semicircles. In that case, elements such as a constant phase element (CPE) or a Warburg element are employed. Basically, CPE refers to a circuit element with a constant phase angle and a Warburg with a phase shift angle of  $45^\circ$  [90,91]. Impedance formula for a CPE is given in table 2.3 where  $\alpha$  is a variable coefficient with values  $-1 \leq \alpha \leq 1$ . When  $a = 1$  the CPE behaves as a capacitor, for  $a = 0$  as a resistor and for  $a = -1$  as an inductor.

Table 2.3: Impedance of modeling electrical elements.

Element	Description	Impedance
R	Resistor	R
C	Capacitor	$\frac{1}{i\omega C}$
L	Inductor	$i\omega L$
Q	CPE	$\frac{1}{C(i\omega)^\alpha}$
W	Warburg	$\frac{1}{C\sqrt{i\omega}}$

Table 2.4: Simulated capacitance values attributed to electrochemical processes [89].

Capacitance [F]	Phenomenon responsible
$10^{-12}$	Bulk
$10^{-11} - 10^{-8}$	Grain boundary
$10^{-9} - 10^{-7}$	Surface layer
$10^{-7} - 10^{-5}$	Sample-electrode interface
$10^{-4}$	Electrochemical reactions

AC impedance spectra for tested SOFCs were recorded within a frequency range of 0.1 Hz to 1 MHz and alternating voltage amplitude of 10 mV and 20 mV using a Solatron SI 1287 potentiostat-galvanostat and a Solatron SI 1255 frequency response analyser. Analysis of the EIS data was carried out with ZView and OriginPro software.

### 2.9.3 Four-point DC conductivity

Conductivity of sprayed deposited electrolyte and anode electrode films was measured using a 4-point collinear probe technique. Electrical measurements carried out using the experimental apparatus illustrated in figure 2.13.

The system consists of an alumina tube with a sample holder, a tubular furnace, a thermocouple, Pt wires, a source measurement unit, and a PC unit.

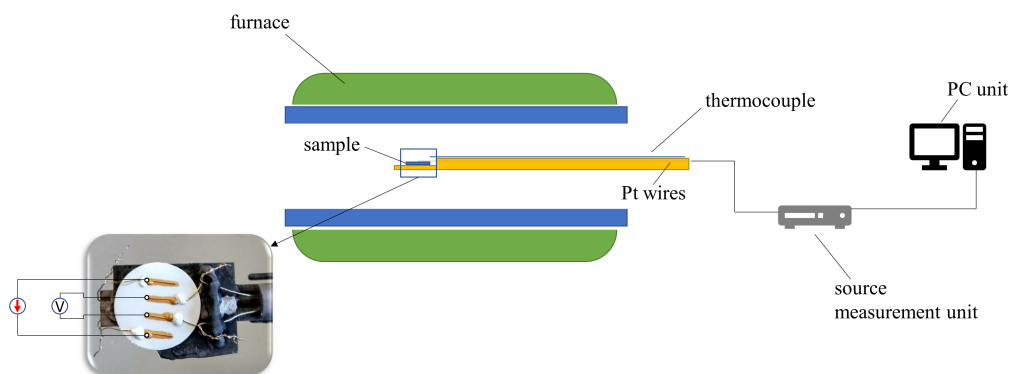


Figure 2.13: Four-point DC conductivity experimental apparatus.

a source measurement unit (Keithley 2401) which can source and measure current and voltage and a computer software to record the data. Gold paste (M-9875, Metalor<sup>®</sup>) was used to paint four stripes of similar dimensions on the deposited films and subsequently sintered at 800 °C. The dimensions and the distance of the four stripes were measured using ImageJ<sup>®</sup> software. Platinum wires were used to connect the contacts with the instrument unit. To accurately measure the temperature a K-type thermocouple was placed close to the sample. In principle, as shown in figure 2.13 a DC current is applied at the two outer probes while the voltage between the two inner probes is being measured. To calculate the resistivity of the film measured values of resistance have to be corrected with a geometric factor given by:

$$G.factor = \frac{Lt}{d} \quad (2.13)$$

where  $L$  is the length of the stripes,  $t$  is the thickness of the film and  $d$  is the space between the voltage probes.

Therefore, the conductivity ( $S/cm$ ) of the film at a certain temperature is calculated by:

$$\sigma = \frac{1}{G.factor R} \quad (2.14)$$

where  $\sigma$  is the conductivity and  $R$  the measured resistance. Temperature dependence of conductivity which is a thermally activated process can be expressed as:

$$\sigma T = \sigma_o \exp\left(\frac{-E_\alpha}{kT}\right) \quad (2.15)$$

where  $\sigma_o$  is a pre-exponential factor,  $E_\alpha$  the activation energy,  $k$  Boltzmann constant and  $T$  the absolute temperature. A graphic representation of the above equation is given by an Arrhenius plot of  $\log(\sigma T)$  versus  $1000/T$ . Thus, from the slope of the Arrhenius line the activation energy can be calculated [92].

Four-point DC conductivity measurements were performed under static air or 5% H<sub>2</sub>/Ar against temperature with a heating-cooling rate of 3 °C/*min*.

# Preparation of substrates for cathode supported SOFCs

## 3.1 Introduction

Cathode-supported solid oxide fuel cells (SOFCs) among the other existing designs exhibit exceptional high durability and low cost making them attractive for commercialisation [93]. Siemens/Westinghouse was the first to develop a cathode-supported SOFC stack which has demonstrated the longest lifetime ( $>35,000$  h) in the history of SOFCs [15]. The merits of this design rely on the thin electrolyte and contribution of reduced ohmic losses and a thin anode with improved redox stability [18,94]. In addition, strontium-doped lanthanum manganite (LSM) is considered to be the state of the art cathode material due to excellent chemical and thermal expansion compatibility with the yttria-stabilized zirconia (YSZ) electrolyte at operating temperatures, high electronic conductivity, good catalytic activity for oxygen reduction and low cost [19, 94, 95]. Furthermore, combining LSM with YSZ in a composite structure has the advantage of expanding the triple phase boundary areas (TPBs) enhancing the ionic conductivity and thus reducing the polarisation resistance of the

electrode [96,97]. However, due to application of high sintering temperatures (*i.e.*  $>1300\text{ }^{\circ}\text{C}$ ) for densification of the YSZ electrolyte formation of secondary phases ( $\text{La}_2\text{Zr}_2\text{O}_7$ , LZO and  $\text{SrZrO}_3$ , SZO) occurs at the interface of LSM/YSZ degrading significantly the cell's performance [18,19,22,98]. This rapid SOFC degradation can be explained by the low ionic conductivity and different thermal expansion coefficient compared to YSZ of the LZO and SZO phases [99]. To suppress the formation of the zirconate phases A-site deficient  $(\text{La}_{0.8}\text{Sr}_{0.2})_{0.95}\text{MnO}_3$  can be used which is less reactive with a zirconia-based electrolyte than the stoichiometric LSM at high sintering temperatures [22,94]. Also, the formation of the LZO can be hindered with an increased ratio of LSM/YSZ [98]. Since, the cathode provides the structural support to the SOFC it is crucial to be highly porous to enable gas diffusion due to the high thickness (*i.e.*  $0.2 - 1\text{ mm}$ ) and mechanically strong [22,100]. In addition, the top-surface morphology of the substrate has a great impact on structural features (*e.g.* uniform thickness) of a thin oxide film deposited on top by spray pyrolysis technique [45,60]. Therefore, the top surface has to be smooth with small pore sizes and minimum defects. Composite substrates of LSM-YSZ were prepared in button and bar shape pellets. Microstructure and phase composition were investigated by scanning electron microscopy (SEM) and X-ray diffraction (XRD), respectively. Electrical measurements performed by means of 4-point DC conductivity within a temperature range of  $400\text{-}800\text{ }^{\circ}\text{C}$  in static air.

## 3.2 Morphology characterization

Initially, for the preparation of the substrate-pellets commercial ceramic powder of  $(\text{La}_{0.8}\text{Sr}_{0.2})_{0.95}\text{MnO}_3$  (5LSM,  $\pi$ -Kem) was used. To enhance the porosity of the

substrates polymethyl methacrylate (PMMA, Soken ltd) microspheres were used as a pore former which leads to formation of an interconnected network of pores within the substrate [101,102]. The 5LSM powder was mixed with 5 wt.% binder (Decoflux wb-41), 7.5 wt% pore former (PMMA) and deionized water using a mortar and pestle. The resulting suspension was dried at 80 °C for 60 min and pressed into pellets at 147 MPa using stainless steel dies of 25 mm and a hydraulic press (Specac). Afterwards, the samples were sintered at 1200 °C for two hours. Figure 3.1 shows obtained microstructure of the substrates where formation of isolated large (0.28 cm<sup>2</sup>) dense areas is observed. One possible explanation is the excessive particle growth and shrinkage of 5LSM [103].

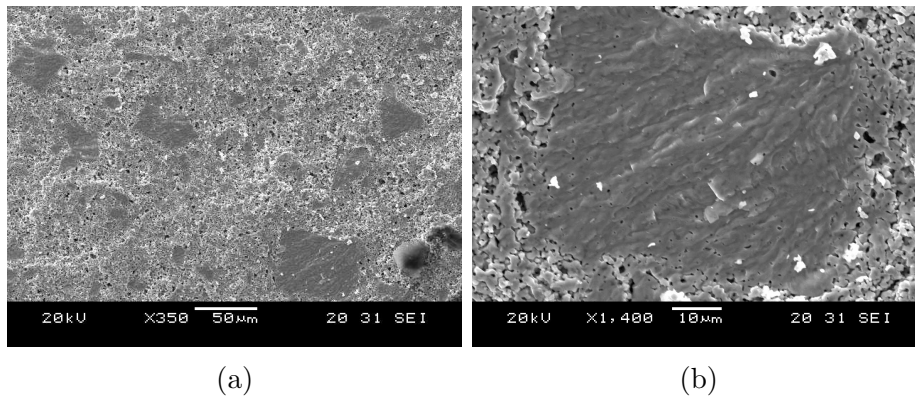


Figure 3.1: SEM images in cross section of 5LSM substrates sintered at 1200 °C for two hours.

However, these agglomerates cause a significant reduction of the substrate porosity and leading to serious gas diffusion problems [22]. As a first attempt to avoid the formation of these agglomerates into the 5LSM cathode, substrates were sintered at lower temperatures (<1200 °C) leading to substrates with poor mechanical properties. Therefore, in order to optimize the microstructure of the substrates a series of steps was followed. At first, 5LSM powder was calcined at 800 °C for one hour to

coarsen the particles and sieved through a mesh (106  $\mu\text{m}$ ) to break down formed agglomerates. It is known, that thermal pre-treatment of a ceramic powder increases the particle size and thus improves the porosity [104]. In figure 3.2 shows calcined 5LSM powder before and after sieving where smaller agglomerates are present.

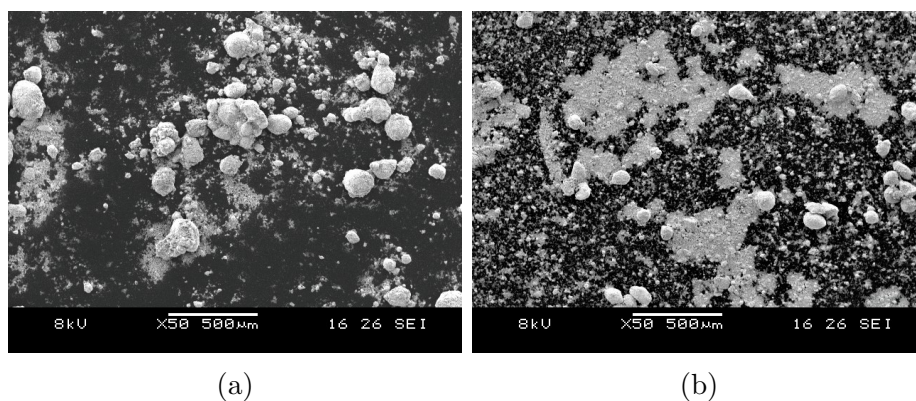


Figure 3.2: Top view SEM images of 5LSM powder a) as obtained after calcination at 800 °C for 1 hour and b) after sieving through a mesh (106  $\mu\text{m}$ ).

Particle size analysis of the 5LSM powder was performed using a particle size analyser (Mastersize 2000, Malvern Instruments ltd.). The starting particle size (D50) increased after the calcination and sieving from 2.85  $\mu\text{m}$  to 5.00  $\mu\text{m}$  with a reduced percentage of agglomerates as shown in figure 3.3. In addition, to suppress excessive particle growth of the 5LSM during the sintering step that reduces the porosity of the substrates commercial powder of 3 mol % yttria-stabilized zirconia (3YSZ, Tosoh) with a smaller particle size of 0.04  $\mu\text{m}$  was used to coat the particles of the 5LSM [105, 106].

Thermogravimetric analysis (TGA) of the PMMA was performed using a TG analyser (NETZSCH TG 209) to determine the temperature in which complete removal occurs forming a porous microstructure. A quantity of 7.7 mg of PMMA was placed in an alumina crucible and heated up to 900 °C with a heating rate of

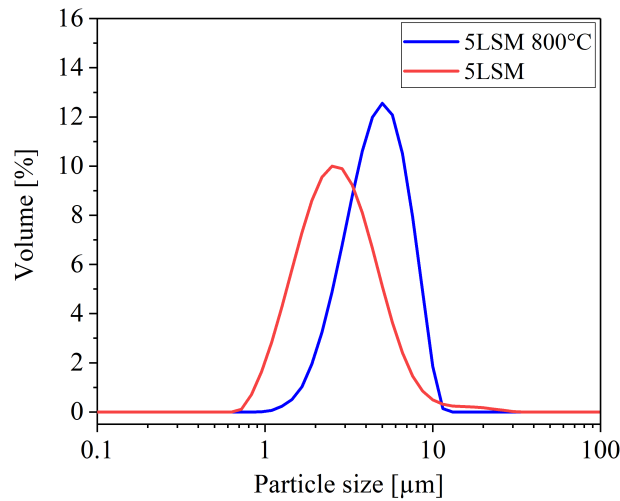


Figure 3.3: Particle size analysis of 5LSM powder before and after calcination at 800 °C for 1 hour with a heating-cooling rate of 3 °C/min.

3 °C/min. Figure 3.4 shows that mass loss starts approximately at 300 °C and finish at 400 °C. In order to avoid structure collaption of the substrate the first segment of the sintering profile was set at 450 °C with a slow heating rate of 1.5 °C/min and 2.5 °C/min for the second segment up to 1200 °C as shown in figure 3.5.

In addition, to homogenize the mixture and obtain a substrate microstructure with uniform porosity two stage ball milling was applied. A detailed description of the ball milling procedure and the optimum material quantities being used is given in chapter two (see section 2.2). In figure 3.6-a,b SEM microphotographs in cross section of the prepared composite 5LSM-3YSZ substrates are shown. The obtained morphology is free from agglomerates compared to the initial microstructure (Fig. 3.1) and the porosity was 42% as measured by Archimedes method and image processing using ImageJ<sup>®</sup> software. Although, the porosity obtained for the 5LSM-3YSZ is optimum for gas diffusion it corresponds to less mechanically strong

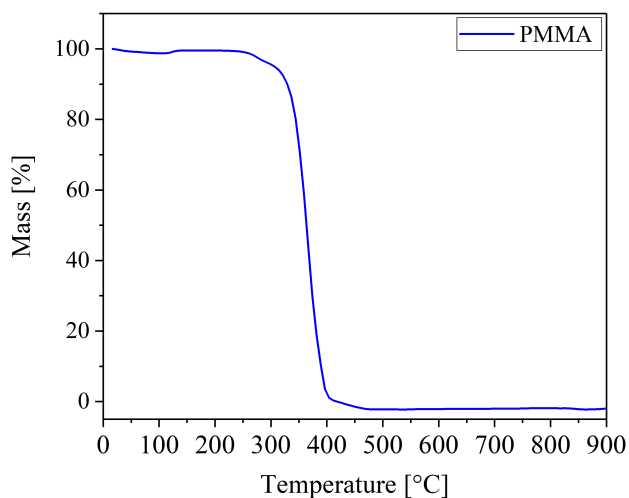


Figure 3.4: TGA analysis of PMMA under air up to 900 °C with a heating rate of 3 °C/min.

substrates [22]. This in conjunction with sealants of different thermal expansion coefficient (TEC) can lead to cracking of the support during operation and failure of the SOFC. To avoid this, composite substrates of 5LSM-8YSZ prepared with an increased ratio of 1:1 wt.%. Moreover, the porosity reduced to approximately 25% by using 4.5 wt.% of PMMA. The same procedure of ceramic pretreatment and sintering was followed for the new substrates. The produced 5LSM-8YSZ pellets were mechanically stronger with an increased ionic conductivity and reduced porosity (Fig. 3.6c). For a certain number of experiments 5LSM-8YSZ substrates were used to examine if they are sufficiently strong to withstand produced stresses and perform efficiently as a cathode electrode support during a fuel cell operation. Another structural feature of the substrates that strongly affects the mechanical strength of the substrates and also the deposition temperature is the thickness of the pellets. In general, thicker substrates provide improved mechanical stability. However, these

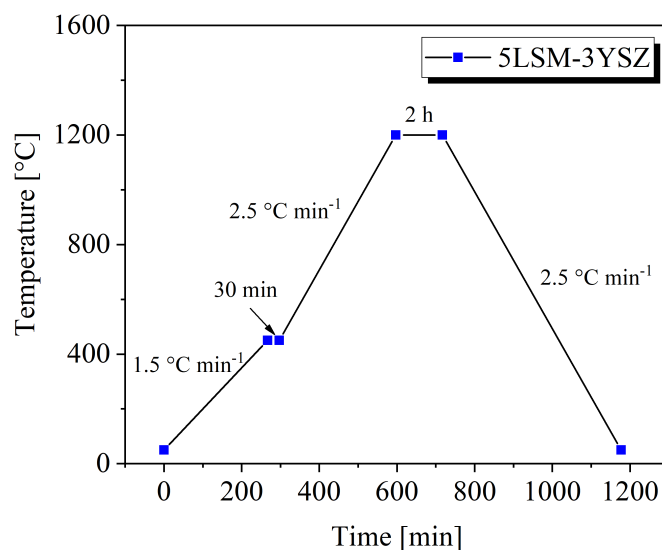


Figure 3.5: Sintering profile of composite 5LSM-3YSZ substrates (1200 °C and dwell time of 2 hours).

exhibit limited gas diffusion and increased ohmic resistance contribution leading to poor SOFC performance. In figure 3.7 shows the effect of the substrate thickness to the deposition temperature. The maximum deposition temperature that can be applied is inversely proportional to the thickness of the substrate due to a different rate of heat flow. Substrate temperature measurements were performed using a handheld temperature probe to estimate the maximum temperature that could be achieved at a fixed distance of 25 cm between the spray gun and the substrate and an air flow rate of 30 L/min. As an optimum substrate thickness in terms of mechanical strength and adequate substrate temperature for the spray deposition experiments without compromising significantly gas diffusion was approximately 1 mm.

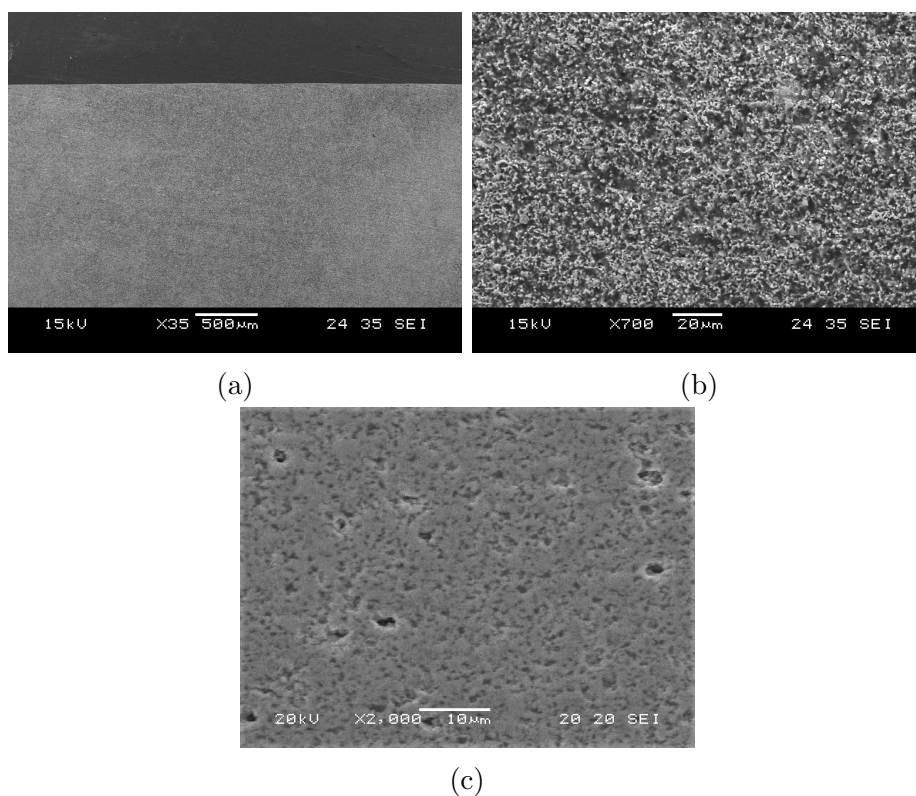


Figure 3.6: SEM images of a,b) 5LSM-3YSZ (9:1 wt.%) in cross section with a uniform interconnected porosity of 42%. and c) 5LSM-8YSZ (1:1 wt.%) with a uniform porosity of 25 % sintered at 1200 °C for 2 hours.

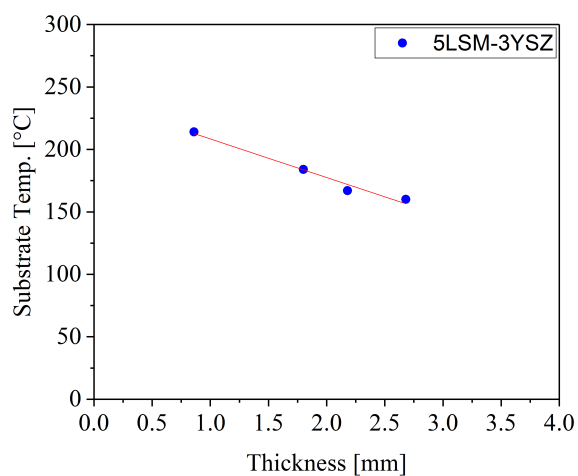


Figure 3.7: 5LSM-3YSZ substrate temperature correlated with the thickness.

Figure 3.8 shows X-ray diffraction patterns of individual ceramic powders of 5LSM and 3YSZ in comparison with the composite 5LSM-3YSZ substrate. Since the sintering temperature was lower than 1350 °C there are no XRD peaks corresponding to insulating phases of  $\text{La}_2\text{Zr}_2\text{O}_7$  (LZO) and  $\text{SrZrO}_3$  (SZO) formed between the 5LSM and YSZ in agreement with the literature [22, 94, 103].

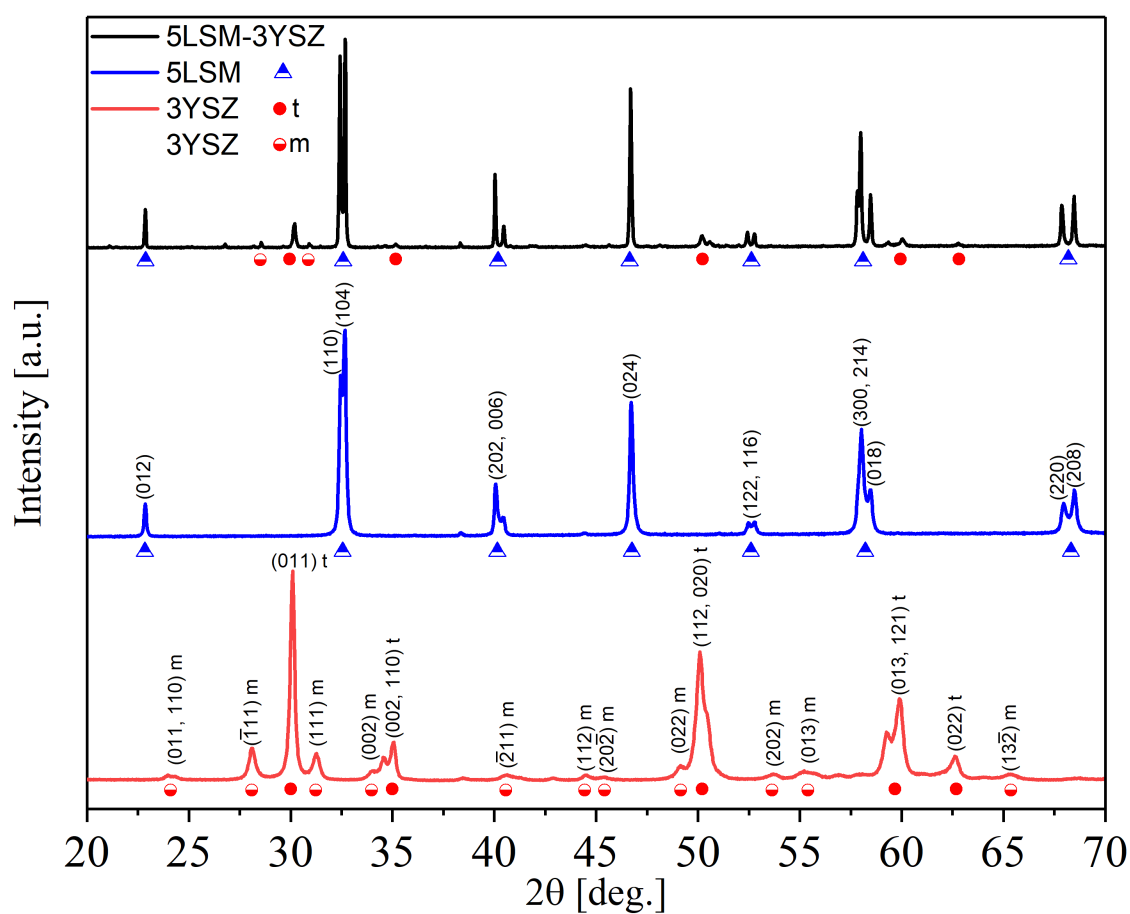


Figure 3.8: XRD analysis of commercial ceramic powders of 5LSM ( $\pi$ -Kem ltd), 3YSZ (Tosoh) and 5LMS-3YSZ (9:1 wt.%) pellet sintered at 1200 °C for 2 hours.

### 3.3 Conductivity measurements

To evaluate the effect of 3YSZ on substrates electrical conductivity and estimate the ohmic contribution of the composite substrate to the SOFC, four-point DC conductivity was carried out. Ceramic powders of 5LSM and 5LSM-3YSZ were uniaxially pressed using a hydraulic press at 147 MPa into bar-shape pellets and sintered at 1200 °C (Fig. 3.5). Prior to each measurement four stripes were painted on the bars using a gold paste. On each stripe a gold wire was placed and fixed at one point by using a ceramic adhesive (Ceramabond 552, Aremco Inc.). The prepared samples initially were dried at 80 °C for 10 min and subsequently sintered at 750 °C for 1 h with a heating rate of 2 °C/min. A photograph of a prepared sample is shown in figure 3.9. The dimensions and the space between the gold stripes were measured using ImageJ<sup>®</sup> software. During an electrical measurement a source measurement unit (Keithley 2401) applied a DC current at the two outer probes while the voltage between the two inner probes was measured. The DC conductivity measurements were performed in static air within a temperature range of 400-800 °C with a heating-cooling rate of 2 °C/min. The resistance values derived by Ohm's law were recorded by a suitable interface software. To estimate the conductivity  $\sigma$  (S/cm) of the sample from the measured values of resistance the appropriate geometric factors were used. In figure 3.10, even though a small conductivity reduction is observed from 179 S/cm to 119 S/cm at 800 °C due to addition of 3YSZ (10 wt.%) this conductivity value is still suitable for a SOFC electrode. Respectively, in figure 3.11 a negligible increase of the activation energy is observed from 0.10 eV to 0.11 eV corroborating a metallic conduction mechanism through the LSM phase [22].

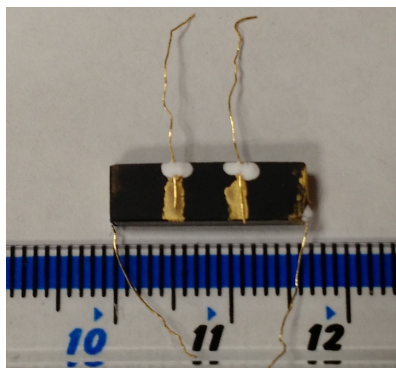


Figure 3.9: 5LSM-3YSZ composite cathode electrode prepared for 4-point DC conductivity measurement.

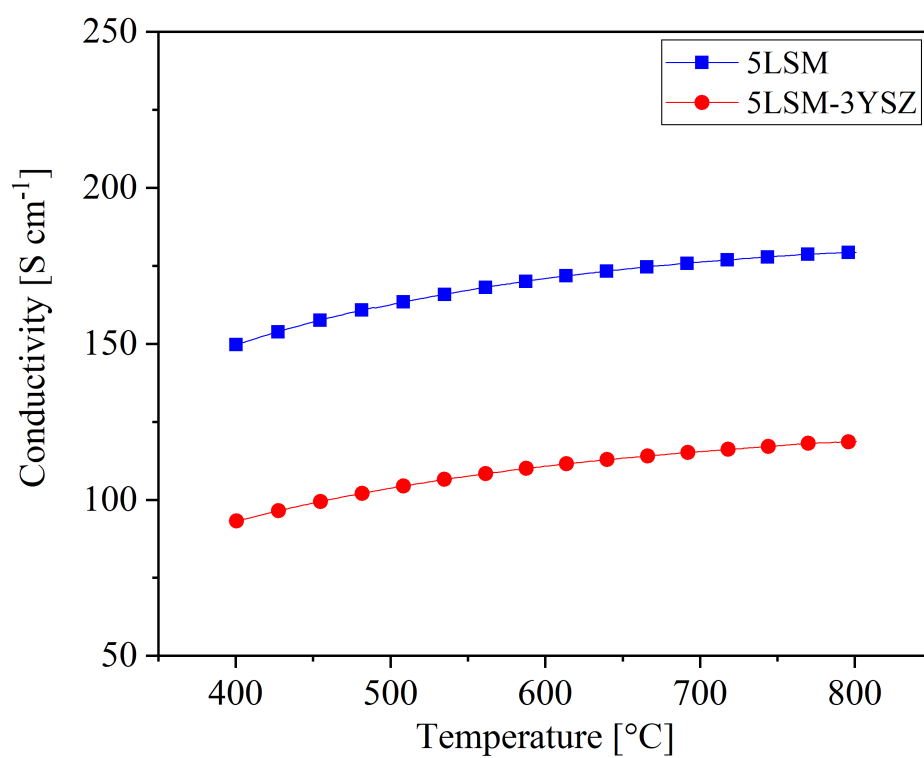


Figure 3.10: 4-point DC conductivity measurements with a maximum value of 179 S/cm for the 5LSM and 119 S/cm for the 5LSM-3YSZ substrate at 800 °C.

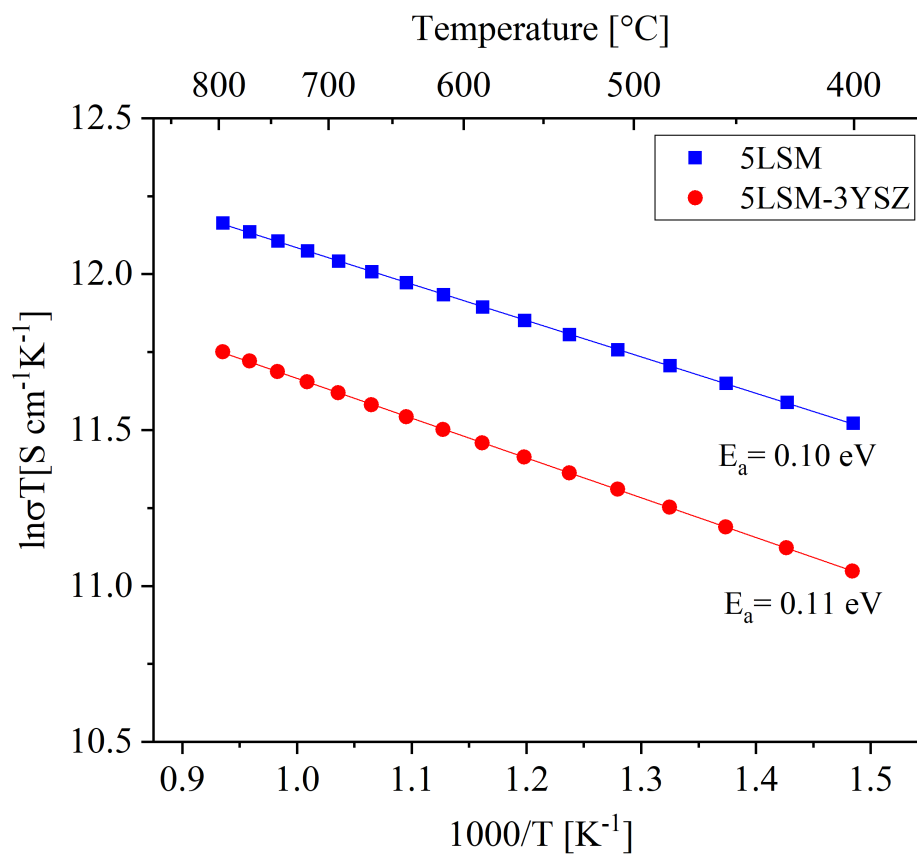


Figure 3.11: Arrhenius plot of conductivity with activation energies  $E_a$  of 5LSM and 5LSM-3YSZ substrates.

## 3.4 Conclusions

Suitable cathode supports of LSM-YSZ for use in SOFCs were produced successfully by using a series of steps of conventional ceramic processing (i.e. coarsening of ceramic particles, ball milling, powder pressing). A uniform porosity of 42 wt.% was achieved fulfilling the requirement for adequate gas diffusion. Produced pellets were sintered at 1200 °C for 2 hours and characterised by XRD with no indication of secondary zirconate phase formation at the interface of LSM and YSZ. Cathode substrates of 1 mm thickness exhibited adequate gas diffusion, mechanical strength and deposition temperature for coating of thin films by spray pyrolysis. A conductivity value of 119 S/cm was measured at 800 °C in air for the composite cathode substrates by four-point DC conductivity indicating a suitable electronic conductivity for a SOFC electrode.



# Origin of defects in SOFC thin films deposited by spray pyrolysis

## 4.1 Introduction

Cathode-supported solid oxide fuel cells (SOFCs) enable the use of thin electrolytes (*i.e.*  $\leq 10\ \mu\text{m}$ ) lowering the operating temperature of these devices to an intermediate range of 650-750 °C [19]. As a cathode support lanthanum strontium manganite (LSM) is commonly used with an yttria stabilized zirconia (YSZ) electrolyte due to low cost and excellent chemical and thermal stability these materials exhibit at operating temperatures. However, the application of high sintering temperatures ( $\sim 1400\ \text{°C}$ ), in order to obtain a gas-tight electrolyte, leads to formation of resistive zirconate phases at the interface between the cathode and the electrolyte with detrimental effects on the performance of the cells [16]. In addition, similar chemical side-reactions with the electrolyte occurs when alternative more catalytically efficient cathode materials such as  $\text{La}_{0.6}\text{Sr}_{0.4}\text{Co}_{0.2}\text{Fe}_{0.8}\text{O}_{3-\delta}$  (LSCF) are used [107]. To avoid the formation of these resistive interfacial layers the addition of diffusion barrier coatings, such as gadolinia-doped ceria (GDC) has been a possible solu-

tion [108]. Still, to achieve the requirement of a dense structure, processing even at temperatures as low as 1000 °C has been found to form an insulating layer at the interface of GDC and YSZ [109].

Towards this end, various deposition techniques such as physical vapor deposition (PVD) and chemical vapor deposition (CVD) have been developed over the last two decades to prepare supported thin electrolytes and diffusion barrier coatings at reduced sintering temperatures. However, these techniques suffer from low deposition rates and require more complicated and expensive equipment limiting the potential for mass production [17]. Among the family of deposition techniques spray pyrolysis represents a cost-effective and easy to scale technique for preparation of SOFC thin films at low sintering temperatures [49].

Nevertheless, many process parameters (*e.g.* precursor concentration, deposition time etc.) are involved which if are not optimized properly introduce defects such as cracks, porosity and large particles disrupting the structure of the film and thus the gas-tightness of the interface protective coating or the electrolyte itself. In this chapter a parametric study was conducted to reveal the origin of defects in SOFC thin films and how to optimize the process parameters of spray pyrolysis technique to obtain defect-free SOFC thin films.

## 4.2 Spray pyrolysis process parameters

The spray pyrolysis technique involves atomization of a precursor solution to an aerosol directed to a heated substrate where thermal decomposition (*i.e.* pyrolysis) of the salts occurs forming a thin oxide film. The main component of a typical spray pyrolysis system is the spray nozzle. Spray pyrolysis is distinguished in dif-

ferent varieties (*e.g.* air pressurized, ultrasonic, electrostatic) based on the type of the spray nozzle [46]. The means of solution aerosol formation determines the atomization rate, initial droplet size and droplet velocity that consequently affect the film morphology [55, 110]. The fact that pressure atomizers exhibit significantly higher atomization rates combined with equipment simplicity and low cost makes them the industrial standard by many companies [44]. In figure 4.1 shows a photograph of the air-pressurised spray pyrolysis apparatus that was used to investigate the effect of the process parameters on YSZ and GDC thin films. Optimization of the spray pyrolysis technique was carried out using aqueous solutions for the following process parameters: substrate temperature, precursor solution concentration, deposition time, precursor solution flow rate and spray gun nozzle-to-substrate distance.

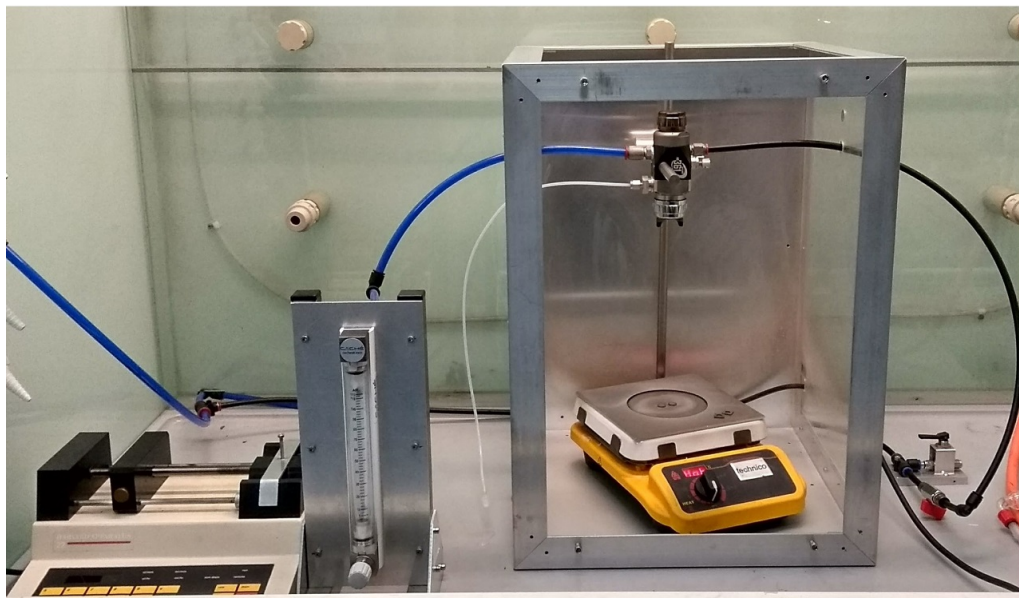


Figure 4.1: Photograph of the spray pyrolysis experimental apparatus.

### 4.2.1 Precursor solution

Among the many process parameters involved in spray pyrolysis technique the most important is the type of the precursor solution that is used for preparation of thin films. Based on the type of the solvent and the precursor, physical properties of the solution are varied such as the boiling point, solubility of the precursor, viscosity and surface tension. These, affect the drying, decomposition kinetics and spreading behaviour of the droplets on the substrate surface modifying the morphology of the film [36,45,46,111]. Thus, other important parameters of spray pyrolysis such as the maximum precursor concentration in conjunction with the substrate temperature and deposition time are tailored based on the type of the precursor solution and the targeted morphology of the film [45,46].

The solvents used are usually deionised water, organics or a mixture of both [42]. The merits of pure aqueous solutions stem from low cost and an environmentally friendly nature [112]. In addition, there is a comprehensive choice of highly water-soluble metal salts (*e.g.* nitrates or chlorides) enabling the preparation of thin films with composite structures [49]. Moreover, due to the high solubility of these types of salts precipitation is hindered within a droplet during spray deposition resulting in formation of a dense particle [44]. However, the higher surface tension of water (*i.e.*  $72 \times 10^{-3}\text{N/m}$ ) compared to other organic solvents such as ethanol (*i.e.*  $21.8 \times 10^{-3}\text{N/m}$ ) might lead to tensile stresses upon drying and consequently to formation of cracks within the film [46,113]. Moreover, the use of metal-organic precursors is limited due to poor solubility in water. Therefore, organic solvents are more suitable to use with these types of precursors.

In addition, with certain types of organic solvents higher boiling points can be

achieved affecting the optimum deposition temperature during spray pyrolysis and consequently the morphology of the films. Chen *et al.* [45] investigated the effect of the solvent composition on film morphology. A denser structure of a  $\text{LiCoO}_2$  thin film was obtained when a mixture of ethanol with butyl carbitol with a higher boiling point (*i.e.*  $230^\circ\text{C}$ ) was used than with pure ethanol (*i.e.*  $78^\circ\text{C}$ ) at a substrate temperature of  $250^\circ\text{C}$ . Perednis *et al.* [46] also observed for deposition of a 8YSZ thin film that using a solvent with a lower boiling point of  $120^\circ\text{C}$  a dense thin film could be obtained at a lower substrate temperature of  $180^\circ\text{C}$ . To this end, Setoguchi *et al.* [14] obtained a thin film of calcia-stabilized zirconia (CSZ) using only ethanol as a solvent at an even lower substrate temperature of  $80^\circ\text{C}$ . In all cases the substrate temperature was higher than the boiling point of the solvent and it seems the lower end of the substrate temperature that can be applied in order to obtain a coherent film is proportional to the boiling point of the solvent. It is noteworthy that the latter comes into agreement with an empirical model described by Beckel *et al.* [114] The authors showed there is an optimum ratio range between deposition temperatures ( $T_{\text{dep}}$ ) and the boiling point ( $T_{\text{bp}}$ ) of solvents where a coherent film of  $\text{La}_{0.6}\text{Sr}_{0.4}\text{Co}_{0.2}\text{Fe}_{0.8}\text{O}_{3-\delta}$  (LSCF) can be obtained. Interestingly, smoother films with no cracks were obtained for the same ratio of  $T_{\text{dep}}/T_{\text{bp}}$  corresponding to a lower deposition temperature and a lower boiling point of solvent. Moreover, for higher substrate temperatures (*i.e.*  $320^\circ\text{C}$ ) where the ratio exceeded 1.25 no continuous film was obtained. This was attributed by the authors to faster solvent evaporation of the droplets and thus to formation of dry particles which were removed by the air stream unable to reach the substrate. From these findings it is evident that the boiling point of the solvent controls the optimum deposition temperature and vice versa for a deposition of a coherent film with no cracks.

Nevertheless, the use of metal-organic salts and organic solvents increase significantly the process cost. In addition, carbon content found in films derived from the organic precursor solution often needs high sintering temperatures to be eliminated and also has adverse effects on crystal phase development [44, 115]. Furthermore, spraying deposition of a flammable solution on heated substrates is not particularly safe [116].

Aqueous solutions consisted of zirconium oxynitrate ( $\text{ZrO}(\text{NO}_3)_2 \cdot 6 \text{H}_2\text{O}$ , Fisher-Scientific, 99.9%) and yttrium nitrate ( $\text{Y}(\text{NO}_3)_3 \cdot 6 \text{H}_2\text{O}$ , Fisher-Scientific, 99.9%) were prepared for deposition of yttria-stabilized zirconia (YSZ) thin films. The total concentration of metal ions was varied from 0.001 to 0.1 mol/l. In order to obtain a stoichiometry of  $(\text{ZrO}_2)_{0.92}(\text{Y}_2\text{O}_3)_{0.08}$ , a molar ratio of Zr:Y=85.2:14.8 was employed. Thermal behaviour of 8YSZ powder and the constituent precursor chemical compounds was evaluated using thermal gravimetric analysis (TGA) combined with differential thermal analysis (DTA) in a Netzsch STA 449C Jupiter<sup>®</sup> analyser.

Figure 4.2 shows TG/DTA measurements of zirconium oxynitrate performed within a temperature range of 40-900 °C at a heating rate of 5 °C/min in air. The two distinct weight derivative (DTG) peaks at 107 °C and 196 °C which also correspond to two endothermic peaks designated in DTA curve, accompanied by a weight loss of 8.35 wt.% and 37.73 wt.% attributed to evaporation of the crystal water. Above ~ 200 °C the anhydrous salt starts to decompose with a simultaneous release of nitrogen ( $\text{NO}_x$ ) gases and reaching a plateau approximately at 407 °C. At this temperature point a weight loss of 63.3 wt.% was measured indicating the formation of amorphous  $\text{ZrO}_2$ . The exothermic peak at 454 °C can be ascribed to crystallization of the formed oxide from the amorphous to monoclinic phase and the burning of residual nitrates in agreement with L.D. Jadhav *et al.* [52]. At 730 °C thermal de-

composition of  $\text{ZrO}(\text{NO}_3)_2 \cdot 6 \text{H}_2\text{O}$  has been fully completed and the weight loss has stabilized to 64.6 wt.% which corresponds to the stoichiometric conversion to  $\text{ZrO}_2$ :

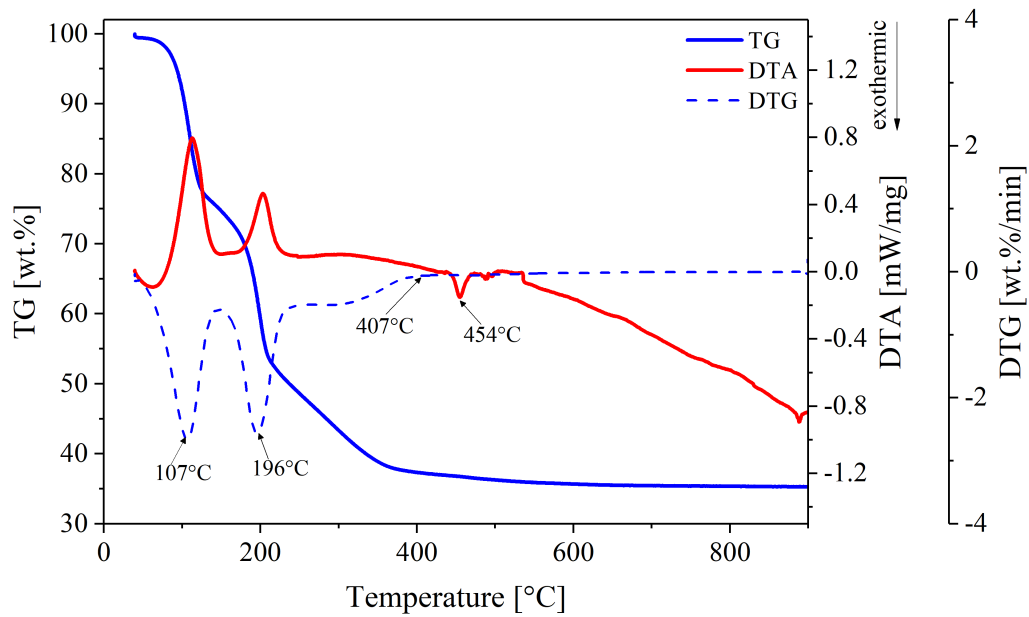
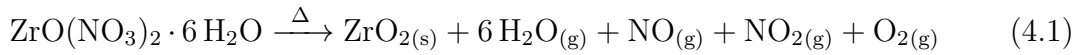


Figure 4.2: TG/DTA analysis of zirconium oxynitrate up to 900 °C at a heating rate of 5 °C/min and dwell time of 10 min in air.

Figure 4.3 shows TG/DTA measurements of yttrium nitrate obtained within a temperature range of 20-900 °C at a heating rate of 5 °C/min in air and dwell time of 10 min. Thermal decomposition of the metal salt occurs in three steps (*i.e.* dehydration, nitrate decomposition and crystallization) as denoted in figure 4.3. Initially, dehydration of the salt occurs up to 249 °C which corresponds to a mass loss of 23.95 wt.%. At the second step residual nitrates and salt intermediates (*e.g.*  $\text{YONO}_3$ ) start

to decompose and burn, up to 560 °C. At this temperature, weight loss has reached a plateau designated in the TG/DTG curve which corresponds to 68 wt.%. A total weight loss of 68.7 wt.% indicates the formation of  $Y_2O_3$  (eq. 4.2) already at 560 °C and improvement of crystallization process up to 900 °C.

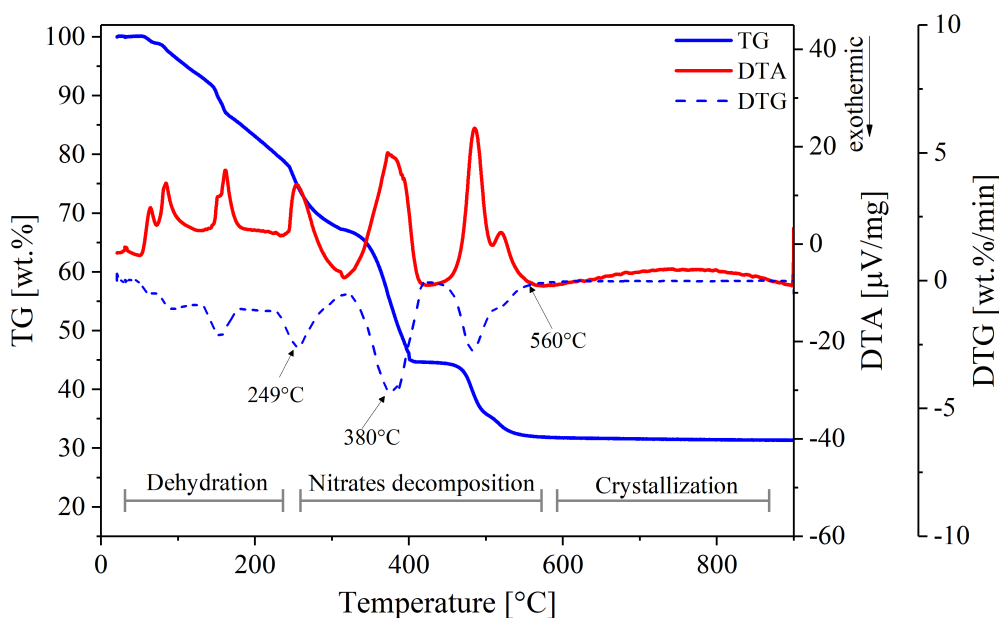
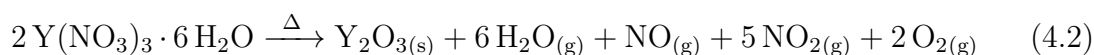


Figure 4.3: TG/DTA analysis of yttrium nitrate up to 900 °C at a heating rate of 5 °C/min and dwell time of 10 min in air. The three steps of thermal decomposition are also shown: dehydration, nitrates decomposition and crystallization.

Since the precursor solution consists of both zirconium and yttrium salts which exhibit different decomposition temperatures (table 4.1) it is mandatory to conduct thermal analysis of the precursor solution to determine the minimum sintering temperature at which the decomposition of the dissolved metal salts is fully completed.

Figure 4.4 shows thermal analysis of amorphous 8YSZ powder performed within a range of 40-900 °C at a heating rate of 10 °C/min and dwell time of 10 min. The powder prior the TG/DTA measurements was recovered after spraying deposition of 0.1 mol/l aqueous precursor solution on glass substrates at a substrate temperature of 200 °C.

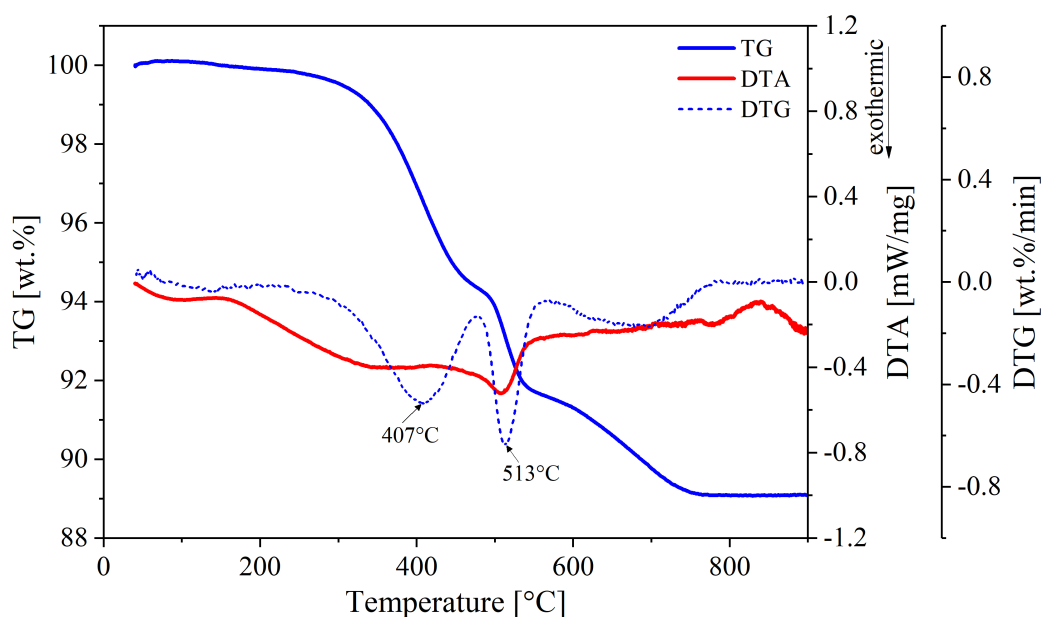


Figure 4.4: TG/DTA analysis of as-deposited 8YSZ thin film ( $T_{\text{sub.}}:200\text{ }^{\circ}\text{C}$ ) up to 900 °C at a heating rate of 10 °C/min and dwell time of 10 min in air.

The two peaks designated in the DTG curve at approximately 407 °C and 513 °C corresponding to weight losses of 3.4 wt.% and 6.9 wt.%, respectively. The latter

corresponds also to an exothermic peak indicating a conversion from amorphous to a crystalline 8YSZ from  $\sim 500$  °C, as confirmed by XRD (fig. 4.5). Additional weight loss is observed up to 750 °C where it was stabilized at 10.9 wt.%. The smaller percentage of total mass loss compared to the individual metal salts (Fig. 4.2, 4.3) indicates a partial decomposition of the salts during spray deposition [117]. From the above results, a minimum sintering temperature of 750 °C should be employed in order to obtain a fully crystalline 8YSZ thin film by spray pyrolysis.

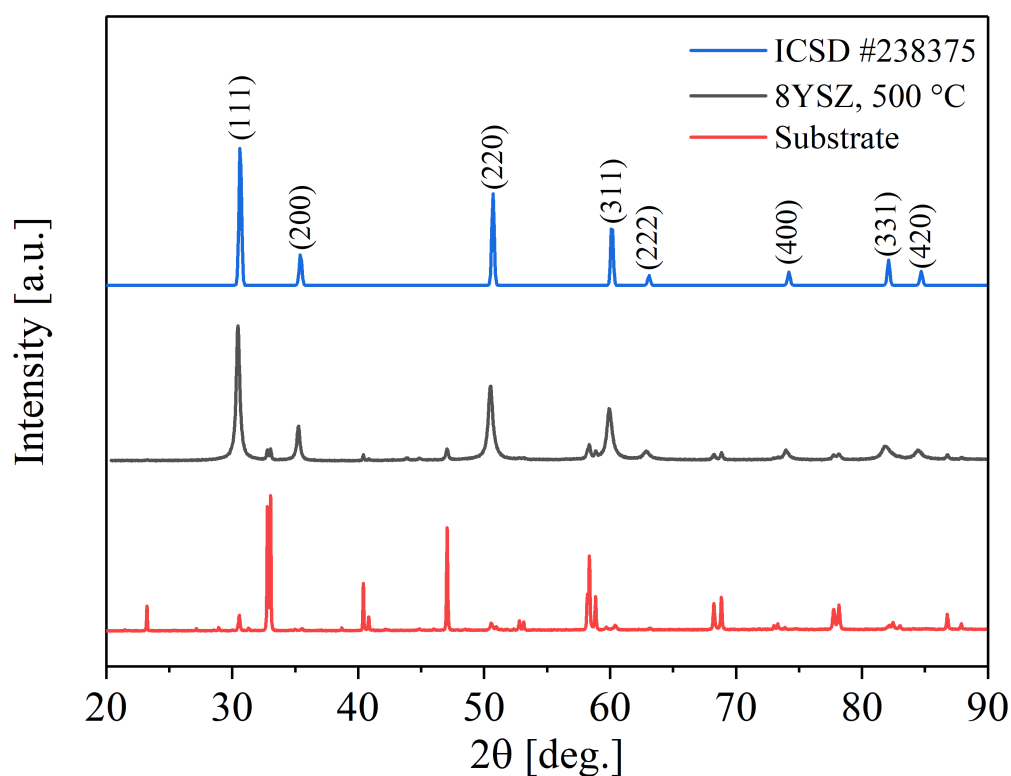


Figure 4.5: X-ray diffraction pattern of 8YSZ thin film deposited on LSM-3YSZ porous substrate. Substrate temperature 200 °C, precursor concentration 0.025 mol/l, calcined at 500 °C for 2 hours.

In a similar way, an aqueous precursor solution of gadolinia-doped ceria (GDC) was also prepared to investigate the thermal behaviour of the precursor and to determine the sintering temperature where a complete thermal decomposition of the metal salts occurs. The  $\text{Gd}_{0.1}\text{Ce}_{0.9}\text{O}_{1.95}$  (GDC) precursor solution with a total ion concentration of 0.1 mol/l consisted of 0.018 mol/l gadolinium nitrate ( $\text{Gd}(\text{NO}_3)_3 \cdot 6\text{H}_2\text{O}$ , Fisher-Scientific, 99.9%) and 0.082 mol/l cerium nitrate ( $\text{Ce}(\text{NO}_3)_3 \cdot 6\text{H}_2\text{O}$ , Sigma-Aldrich, 99%) dissolved in 100 vol% deionized water. Amorphous GDC powder obtained after spray deposition of 0.1 mol/l precursor solution on glass substrates at a substrate temperature of 183 °C. Figure 4.6 shows TG/DTG measurements obtained within a temperature range of 22-900 °C at a heating rate of 10 °C/min and dwell time of 10 min, in air. The first derivative peak at 93 °C corresponds to physically absorbed water evaporation and to a weight loss of 1.1 wt.%. At 390 °C a sharp weight loss is observed indicating the formation of partially crystalline GDC. This was expected since the conversion temperature to oxide of cerium nitrate is completed at 400 °C which is the dominant metal nitrate in the GDC precursor solution. It is noteworthy, that Choolaei et al. [118] were able to produce a crystalline single phase GDC at a temperature as low as 400 °C confirmed by X-ray diffraction. However, a different approach was used where the authors alter the physiochemical properties of the solution with the addition of ammonium tartrate ( $\text{C}_4\text{H}_{12}\text{N}_2\text{O}_6$ , which enable them to reduce the temperature. A total weight loss of 10.6 wt.% was measured which stabilized from 700 °C. Previous TGA measurements of the constituent metal nitrates showed that the total mass loss is approximately equal to 60 wt.% [72,119]. The smaller percentage of weight loss of the GDC precursor indicates a partial decomposition of the salts during the spray deposition process. From these measurements sintering temperatures  $\geq 700$  °C should be applied in order to obtain

a well crystalline GDC thin film by spray pyrolysis technique.

A summary of the thermal analysis results is given in table 4.1. Due to spray deposition at elevated substrate temperatures (*e.g.* 200 °C) partial decomposition of the precursor solution occurs, explaining the significant difference of total weight loss compared to the individual chemical compounds. Hence, the use of metal nitrates results in negligible volume changes during post thermal treatment of the spray deposited films enhancing the formation of dense microstructures. However, in case of using metal nitrates with considerable different decomposition temperatures such as cerium nitrate (*i.e.* 400 °C) and gadolinium nitrate (*i.e.* 575 °C), stresses might be introduced within the film forming cracks [120]. Interestingly, the temperatures where the weight loss (wt.%) stabilized for both the YSZ and GDC precursor solutions seems to be affected by the decomposition temperatures of the non-dominant metal nitrates. Nevertheless, from the above results to obtain fully crystalline 8YSZ and GDC thin films heat treatment should be applied at temperatures  $\geq 750$  °C and 700 °C, respectively.

Table 4.1: TGA results of metal nitrates and aqueous precursor solutions.

Precursor & metal nitrates	Crystallization Temp. [°C]	TG Total wt.%	Oxide	H <sub>2</sub> O x	Ref.
Y(NO <sub>3</sub> ) <sub>3</sub> · xH <sub>2</sub> O	560-760*900	68.7	Y <sub>2</sub> O <sub>3</sub>	4.8	Present work
ZrO(NO <sub>3</sub> ) <sub>2</sub> · xH <sub>2</sub> O	454-652*900	64.7	ZrO <sub>2</sub>	6.6	Present work
(ZrO <sub>2</sub> ) <sub>0.92</sub> (Y <sub>2</sub> O <sub>3</sub> ) <sub>0.08</sub>	513-750*900	10.9	8YSZ		Present work
Ce(NO <sub>3</sub> ) <sub>3</sub> · 6 H <sub>2</sub> O	400-650	60.4	CeO <sub>2</sub>		[72, 119]
Gd(NO <sub>3</sub> ) <sub>3</sub> · 6 H <sub>2</sub> O	575-700	59.8	Gd <sub>2</sub> O <sub>3</sub>		[72]
Ce <sub>0.9</sub> Gd <sub>0.1</sub> O <sub>1.95</sub>	390-700*900	10.6	10GDC		Present work

\* At these temperatures weight loss (wt.%) was stabilized up to 900 °C.

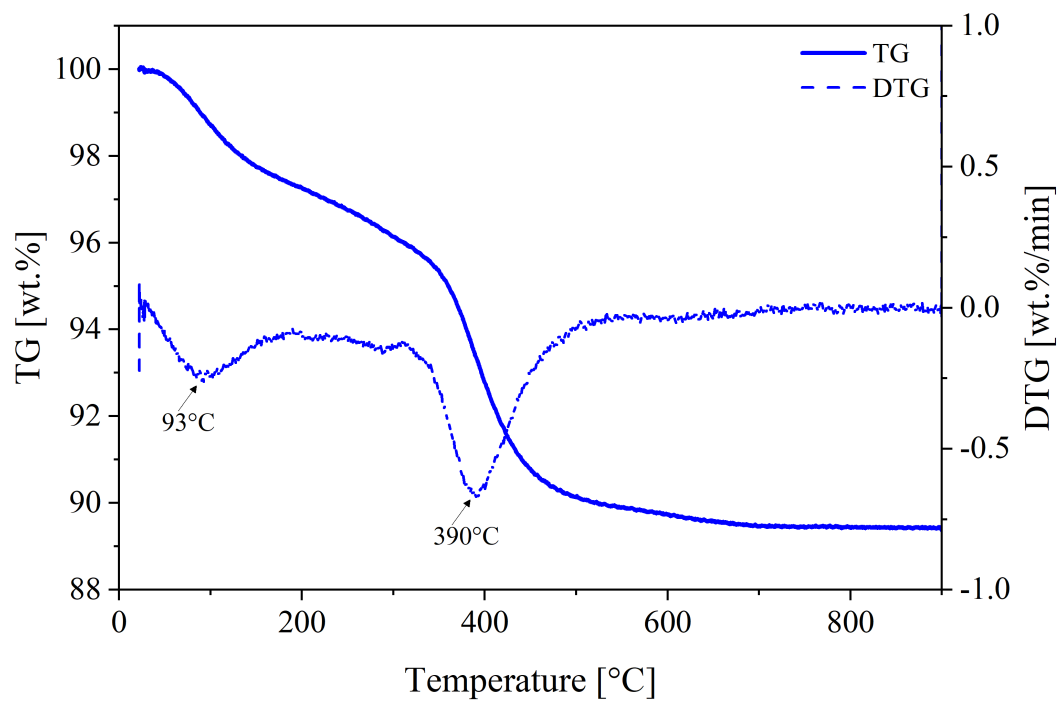


Figure 4.6: TG/DTA analysis of as-deposited GDC thin film ( $T_{\text{sub.}}$ :183°C) up to 900°C at a heating rate of 10°C/min and dwell time of 10 min in air.

### 4.2.2 Substrate temperature

During spray pyrolysis many processes take place including solvent evaporation, precursor precipitation, thermal decomposition (*i.e.* pyrolysis) and sintering of the oxide film which all are combined into a single continuous process [44]. Since, substrate temperature is involved in all the aforementioned processes and is one of the most significant parameters that affect film morphologies and their properties. Viguie and Spitz in 1975 classified spray pyrolysis processes (shown in figure 4.7) that occur based on increasing substrate temperature [121]. At the lowest temperature range (process A) the droplet splashes on the substrate where the solvent vaporises, and the precipitate decomposes. As the temperature increases (process B) the solvent vaporises before the droplet hits the substrate and the dry precipitate hits the surface followed by decomposition. At even higher temperatures (process C) the solvent evaporates and the solid precipitate melts and vaporises (or sublimates). Afterwards the vapor diffuses to the substrate to undergo a chemical vapor deposition (CVD). At the highest temperature range (process D) the solid precipitate vaporises and the chemical reaction occurs in the vapor phase forming powder. The authors suggested that processes A and D should be avoided because they lead to formation of rough or non-adherent films.

In general, the optimum substrate temperature range that leads to formation of continuous and adherent films is dictated by other process parameters such as the type of the salts [46], boiling point of the solvent [114] and precursor concentration [117]. Muecke *et al.* [113] investigated the effect of substrate temperature on deposition rate and film morphology in conjunction with the boiling point and substrate thermal properties. The authors concluded that at high substrate tem-

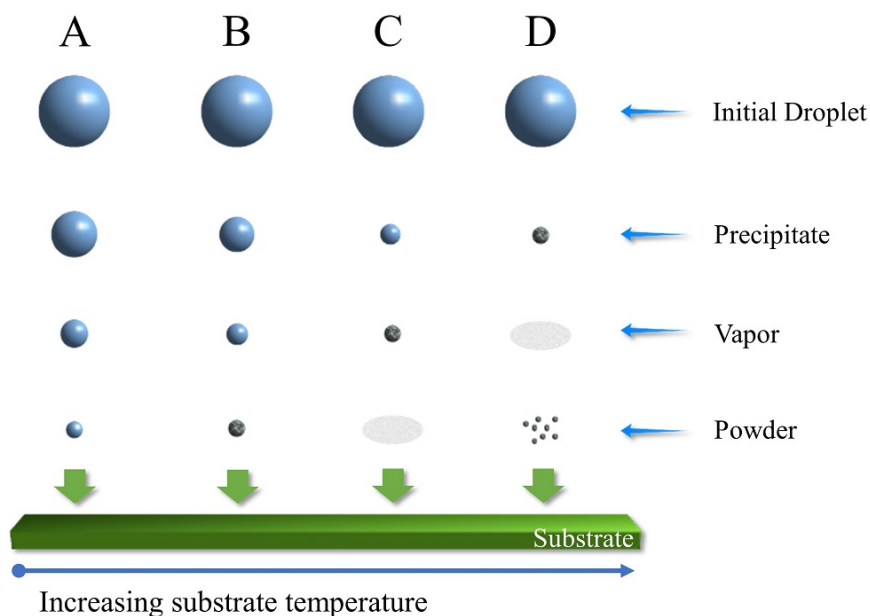


Figure 4.7: Spray pyrolysis processes initiated with increasing substrate temperature [121].

peratures deposition rate decreases and above a maximum substrate temperature for each precursor, Leidenfrost phenomenon takes place that ceases film deposition. This phenomenon occurs when the substrate temperature is well above the boiling point of the solvent, resulting in the formation of a thin vapor layer between the incident droplet and the substrate surface that levitates the droplet instead of reaching the surface.

### YSZ thin films

Yttria-stabilized zirconia  $((Y_2O_3)_{0.08}(ZrO_2)_{0.92})$  thin films were simultaneously deposited on porous cathode substrates of LSM-YSZ by spray pyrolysis. To prepare the precursor solution metal nitrates of yttrium nitrate and zirconium oxynitrate

were dissolved in deionised water with a total ion concentration of 0.1 mol/l. The flow rate of the solution to the spray gun was 0.6 ml/min. To atomize the solution into a uniform aerosol air flow rate was kept at 30 l/min. The nozzle-to-substrate distance was 25 cm. To investigate the effect of the substrate temperature on the 8YSZ thin films two temperatures were chosen at 170 °C and 210 °C. It should be noted, that due to the intense cooling effect of the atomising air a higher substrate temperature was limited. As mentioned earlier the maximum substrate temperature is also affected by properties of the substrate such as heat conductivity, density and heat capacity [113]. Therefore, to be able to increase the LSM-YSZ substrate temperature the porosity of the substrate was decreased to approximately 20% by changing the (wt.%)ratio of the components and reducing the pore former. Spray deposition was carried out in 39 intermittent cycles of 30 sec. After each spray cycle the samples were calcined at 540 °C for 20 min and every 10 cycles for 1 hour. Subsequently, the samples were sintered at 900 °C for 2 hours with a heating-cooling rate of 3 °C/min.

Surface morphologies of  $(Y_2O_3)_{0.08}(ZrO_2)_{0.92}$  thin films deposited on porous 5LSM-3YSZ and 5LSM-8YSZ substrates at substrate temperatures of 170 °C and 210 °C, respectively are shown in figure 4.8. SEM micrographs were taken after sealing and testing both samples electrochemically thus explaining the presence of micro-defects. At the higher deposition temperature the droplets landing on the substrate are dryer hindering their spreading. Therefore, a rougher film morphology is obtained (Fig. 4.8b). In contrast, at a lower deposition temperature the incident droplets on the substrate are semi-dry upon impact with the substrate and thus, they spread more easily forming a smoother film (Fig. 4.8a).

X-ray diffraction patterns of the 8YSZ thin films obtained after sintering at

900 °C for 2 hours are shown in figure 4.9. For both films a cubic fluorite structure is formed with a crystal preferential (111) orientation. This can be observed by considering the intensity of the rest of the diffraction peaks which are significantly decreased compared to the (111) peak. Although, spray deposition of the 8YSZ film at 170 °C indicates formation of preferential orientation at a higher degree this might not be the case as the reflection signal from the 5LSM-3YSZ substrate which contains a smaller percentage of 3YSZ interferes with the measurement.

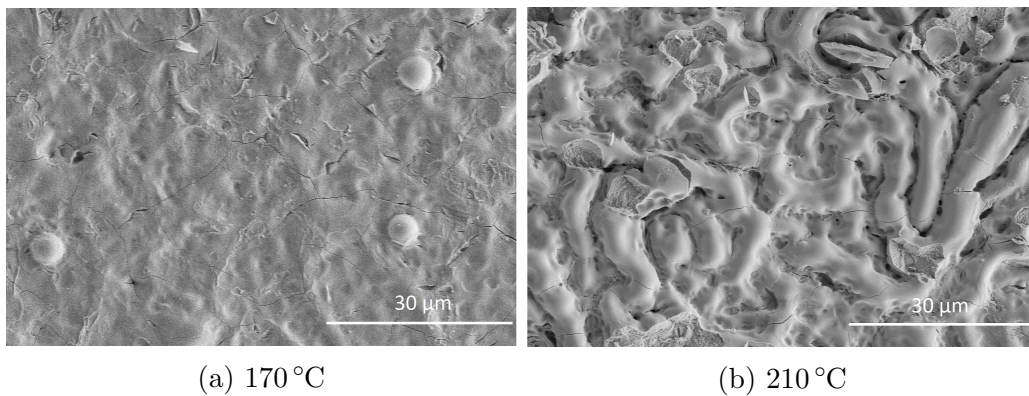


Figure 4.8: SEM micrographs in top view of 8YSZ thin films deposited on porous cathode substrates of a) 5LSM-3YSZ(9:1wt.%) b) 5LSM-8YSZ(1:1 wt.%) showing the effect of substrate temperature. Precursor concentration 0.1 mol/l, solution flow rate 0.6 ml/min, air flow rate 30 l/min, deposition time 19.5 min, number of cycles 39, nozzle-to-substrated distance 25 cm, calcination at 540 °C for 1 hour and subsequent sintering at 900 °C for 2 hours every 5 min of spray deposition.

Nevertheless, comparing the XRD patterns of the film deposited at 210 °C and the corresponding substrate peaks it can be seen the intensities of the peaks (excluding 111 peak) of the coated film are significantly lower, in contrast with the film deposited at 170 °C. Therefore, the preferential orientation seems stronger for the 8YSZ sprayed at a higher substrate temperature. This effect of substrate temperature on promotion of crystal preferential orientation has also been observed by Heiroth *et al.* [122] for 8YSZ thin films prepared by pulsed laser deposition (PLD).

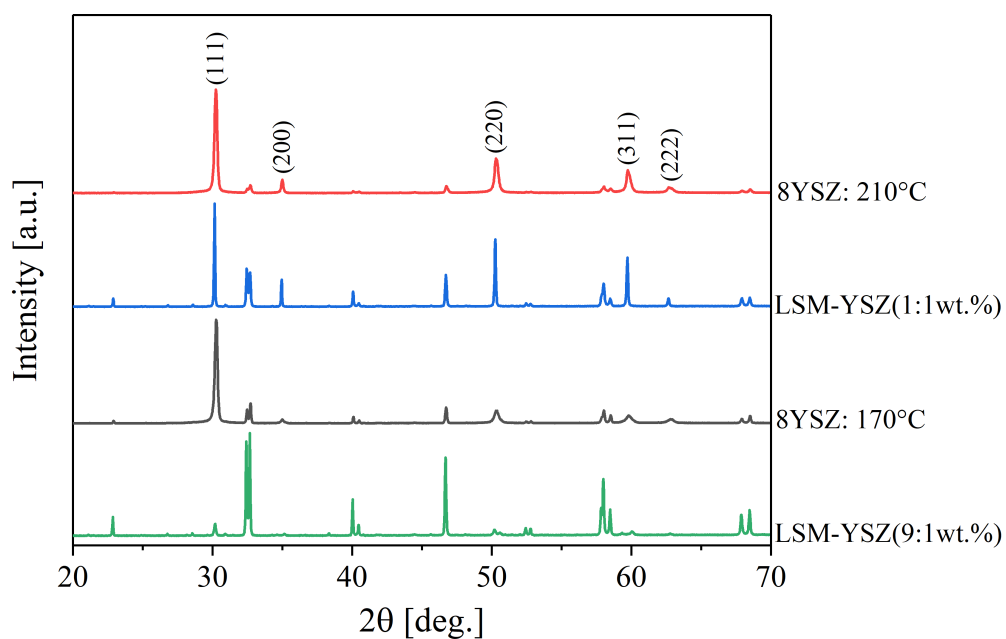


Figure 4.9: X-ray diffraction patterns of 8YSZ thin films deposited on porous cathodes substrates of 5LSM-8YSZ(1:1wt.%) at 210 °C and 5LSM-3YSZ (9:1wt.%) at 170 °C.( The 8YSZ peaks are denoted by miller indices, XRD patterns of uncoated substrates are also included for reference).

The authors found that a preferential(111) orientation is especially favoured for substrate temperatures higher than 400 °C.

### GDC thin films

Gadolinia-doped ceria  $\text{Gd}_{0.1}\text{Ce}_{0.9}\text{O}_{1.95}$  (GDC) thin films were deposited on 8YSZ substrates by air-pressurized spray pyrolysis technique. An aqueous precursor solution was prepared by dissolving metal nitrates of cerium nitrate and gadolinium nitrate with a total ion concentration of 0.1 mol/l. The aqueous precursor solution was fed with a flow rate of 0.6 ml/min to the spray gun where it was atomised by compressed air with a flow rate of 30 l/min. The produced aerosol from a distance of 25 cm was directed to the heated substrate followed by pyrolysis of the salts to form a GDC thin film. The substrate temperature was set to 178 °C (nr. S1) and 225 °C (nr. S2) for each experiment. Prior to spray deposition, substrate temperature was measured with a handheld surface thermocouple. Spray deposition was performed in 12 intermittent cycles of 20 sec. Afterwards, the substrate was covered with an  $\text{Al}_2\text{O}_3$  crucible and glass wool for homogeneous distribution of heat at 540 °C for 20 min. At the end, the samples were further calcined at 540 °C for 1 hour and transferred to a muffle furnace where they post-sintered at a higher temperature of 850 °C for 2 hours with a heating-cooling rate of 3 °C/min. To assess the effect of substrate temperature the same procedure was followed where only the value of this important process parameter was changed.

Figure 4.10 presents top view and cross-section SEM micrographs of the GDC films. Comparison of the two morphologies shows cracks propagated at the surface for both samples with more intense cracks to be present for S1. Although, spray deposition was carried out in intermittent cycles which is a known strategy to relieve stresses during pyrolysis and thus to avoid cracking of the film it was not sufficient to prevent crack formation. One possible explanation might be the precursor compo-

sition in which the decomposition temperature of the metal nitrates is significantly different ( $\sim 175^\circ\text{C}$ ) [120]. However, this type of defect appear not to extend in depth to the entire film reaching the substrate, that would prohibit using the film as a diffusion barrier layer.

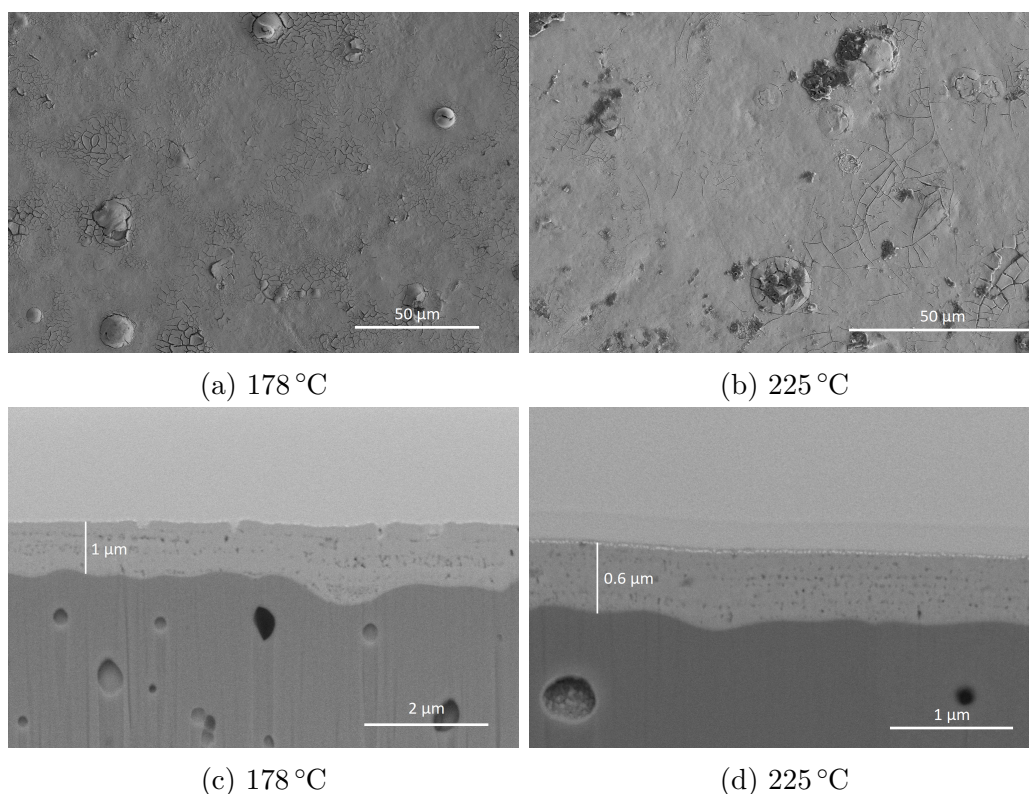


Figure 4.10: FIB-SEM micrographs in top view (a-b) and cross-section (c-d) of GDC films deposited on 8YSZ substrates showing the effect of substrate temperature. Precursor concentration 0.1 mol/l, solution flow rate 0.6 ml/min, air flow rate 30 l/min, deposition time 4 min, number of cycles 12, nozzle-to-substrate distance 25 cm, calcination at  $540^\circ\text{C}$  for 1 hour and subsequent sintering at  $850^\circ\text{C}$  for 2 hours.

The obtained thickness of the films is  $1.0\ \mu\text{m}$  for S1 ( $T_{\text{sub.}}:178^\circ\text{C}$ ) and  $0.6\ \mu\text{m}$  for S2 ( $T_{\text{sub.}}:225^\circ\text{C}$ ) corresponding to a deposition rate of  $15\ \mu\text{m}/\text{h}$  and  $9\ \mu\text{m}/\text{h}$ , respectively. This effect of the substrate temperature on the deposition rate is attributed mostly to thermophoretic forces acting opposite to the initial trajectory of

the droplets, thus fewer precipitates are able to reach the substrate leading to a lower deposition rate [113,123]. A significant increase of the deposition rate compared to the literature is illustrated in figure 4.11. This improvement is mainly attributed to a combination of the applied process parameters mentioned earlier.

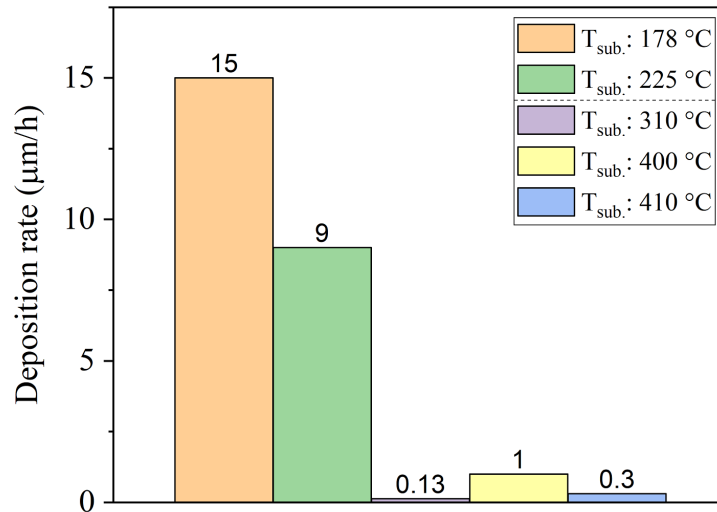


Figure 4.11: Deposition rates for GDC thin films deposited on dense substrates with respect to substrate temperature ( $T_{\text{sub}}$ ). Deposition rate for  $T_{\text{sub}}$ :178 °C and 225 °C refer to this study, 310 °C to Rupp *et al.* [115], 400 °C to L. dos Santos Gomez *et al.* [109] and 410 °C to Szymczewska *et al.* [124].

In figure 4.12a,c TEM micrographs of GDC lamellas are shown. The formation of isolated pores for both films is evident with a higher average size of 70 nm for the S1 film (fig. 4.12a) compared to the 30 nm average pore size for the S2 (fig. 4.12c). It is noteworthy, that the average percentage in closed pores has been estimated to 7% for the S1 and 11% for the S2. This difference possibly can be explained from the higher substrate temperature applied in S2 that limits even more the spreading of the droplets forming more pores and to faster thermal decomposition of the precursor [125]. Surprisingly, a uniform thickness of the GDC films is obtained

although the existing defects (*i.e.* open pores) of the substrates surface as shown in figure 4.12c.

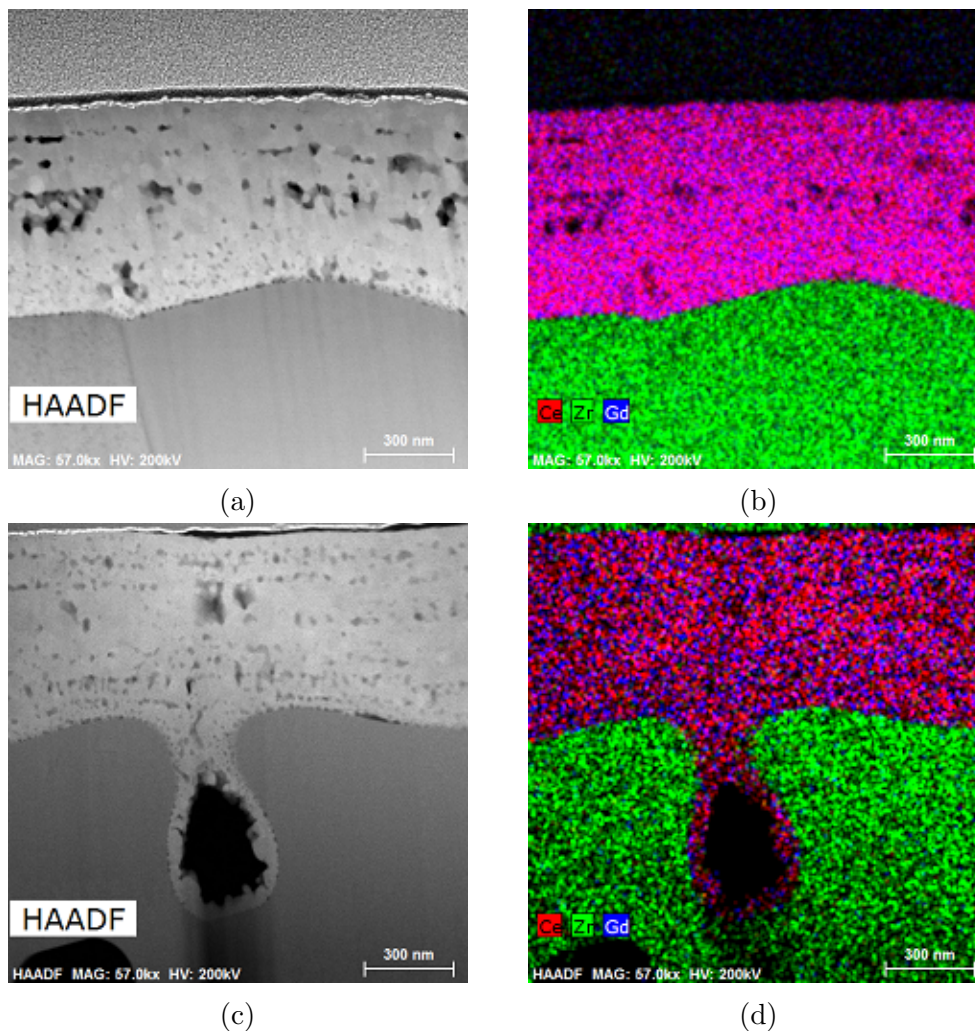


Figure 4.12: HAADF-STEM micrographs and EDS maps in cross section of GDC thin films deposited on 8YSZ disks at substrate temperatures of (a-b) 178 °C and (c-d) 225 °C.

One of the most likely causes is the high surface tension of deionised water used as a solvent that also affect the spreading behaviour of the incident precursor droplets on the substrate [46,113]. Previous studies reported an interdiffusion at the interface of GDC/YSZ forming a highly resistive layer at sintering temperatures as low as

950 °C [57] and 1000 °C [126]. Therefore, heat treatment of the nanostructured GDC films was limited at 850 °C to avoid any side-reaction at the interface. Towards this end, EDS mapping shown in figure 4.12b,d indicated no evidence of interdiffusion.

X-ray diffraction patterns of the GDC films deposited on YSZ disks at different substrate temperatures are shown in figure 4.13. The lattice parameters of the films are given in table 4.2. The GDC films are fully crystalline after sintering at 850 °C with a single cubic fluorite phase [127–129]. It is noteworthy, that the increase of the substrate temperature to 225 °C appears to have a strong effect on preferential oriented growth of the GDC film, while at a lower substrate temperature of 178 °C shows no evidence of preferential growth. The latter is also supported by electron diffraction patterns obtained from both of the films, shown in figure 4.14. In previous works, the effect of preferential orientation of GDC films as a function of post-sintering temperature has been studied [72,115]. However, this is the first time reported that the substrate temperature can strongly control the orientation of a GDC film prepared by spray pyrolysis. In addition, a similar preferential orientation of the GDC film deposited on YSZ disks at 225 °C was reported by Rupp *et al.* [115] where the GDC films were deposited on sapphire substrates. This indicates that the preferential orientation is independent to some extent of the substrate material.

Table 4.2: Lattice parameters of GDC.

Lattice parameter [ $\alpha$ (Å)]	Substrate temperature [°C]	Sample	Reference
5.4302(3)	178	Thin film	this study
5.4319(5)	225	Thin film	this study
5.40	310	Thin film	[115]
5.420		Pellet	[128]
5.4312		Powder	[130]

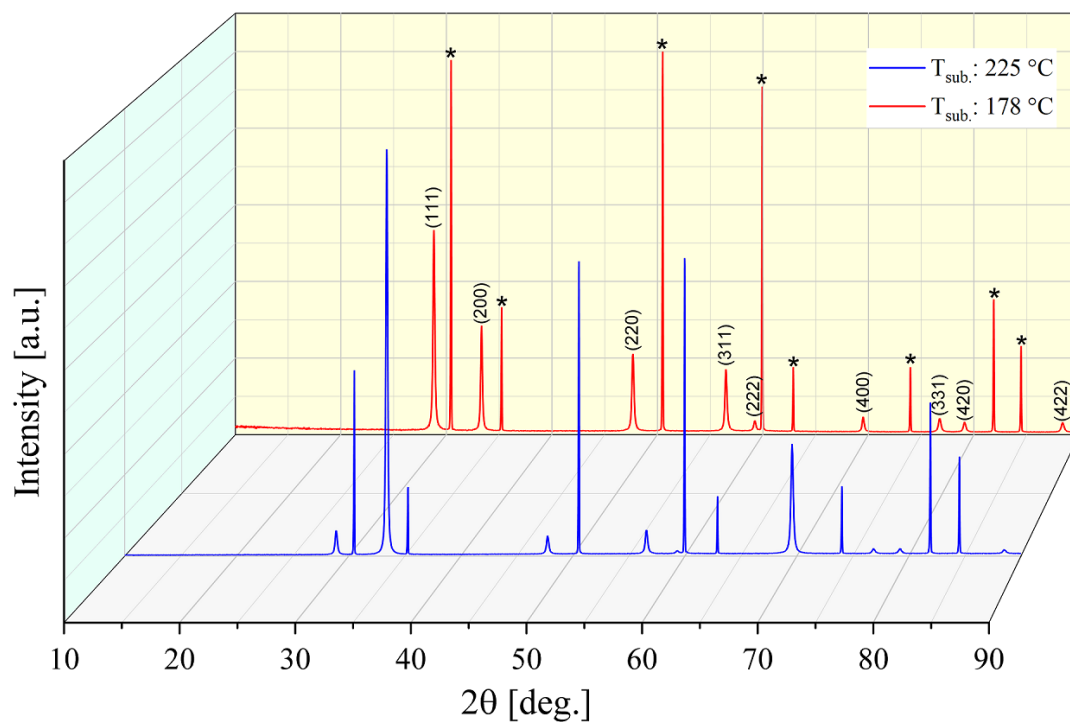


Figure 4.13: XRD patterns of thin GDC films sprayed on dense YSZ substrates at 225 °C and 178 °C (the GDC peaks are denoted by miller indices and substrate peaks by \*).

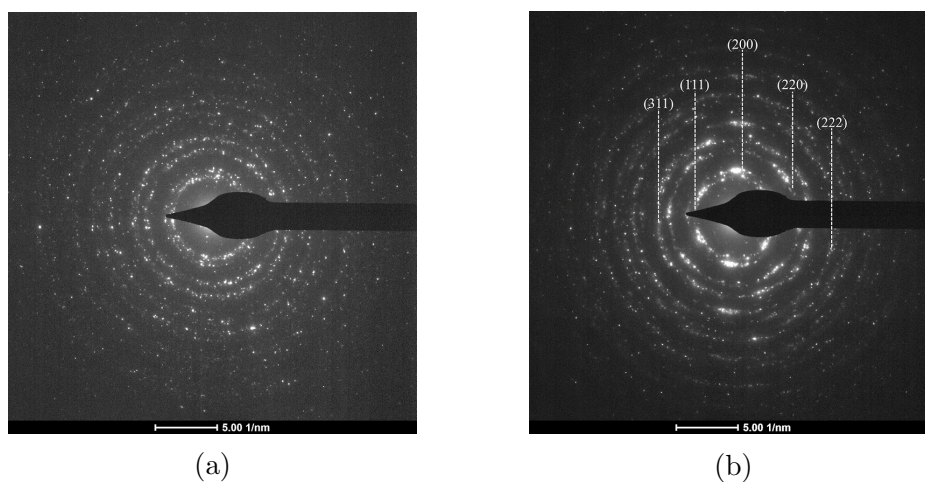


Figure 4.14: Electron diffraction patterns of GDC thin films deposited at different substrate temperatures: (a) 178 °C and (b) 225 °C exhibiting preferential (200) crystal orientation.

Figure 4.15 shows a Williamson-Hall (W-H) plot (section 2.4) for the GDC films deposited at different substrate temperatures. For correction of the instrument peak broadening, measurements from a silicon sample were taken into account. Hence, for the GDC film deposited at 178 °C, a microstrain ( $\varepsilon$ ) of 0.002% calculated from the slope of the fit and a grain size of 45 nm from the y-intercept [76]. However, preferential orientation of the film deposited at 225 °C introduces an uncertainty for a fit that will give an estimation of the microstrain and the grain size. Therefore, the points corresponding to (200) and (400) diffraction peaks were excluded for a more accurate fit. Respectively, from the W-H plot a microstrain of 0.007% and a grain size of 30 nm for the GDC film deposited at 225 °C were calculated. The nano-sized grains of the films presumably results from the applied process conditions (*i.e.* intermittent spray deposition) and the substrate [116,131]. In addition, the low deposition temperature (<250 °C) of the films also contributes to the formation of small grains [132]. According to the literature, there is a correlation of the microstrain with the ionic conductivity of the GDC films, where it is reported that high ionic conductivities are associated with high microstrain values [133]. Therefore, it is expected the more strained GDC film ( $T_{\text{sub.}}=225$  °C) to exhibit an improved ionic conductivity. A summary of the microstrain and grain size values using W-H plots and Scherrer equation for the GDC films is given in table 4.3.

Table 4.3: Geometric parameters of the GDC films.

Substrate temperature [°C]	Film thickness [ $\mu\text{m}$ ]	Debye-Scherrer	Williamson-Hall	
		Grain size [nm]	Microstrain $\varepsilon$ [%]	Grain size [nm]
178	1.0	43	0.002	45
225	0.6	27	0.007	30

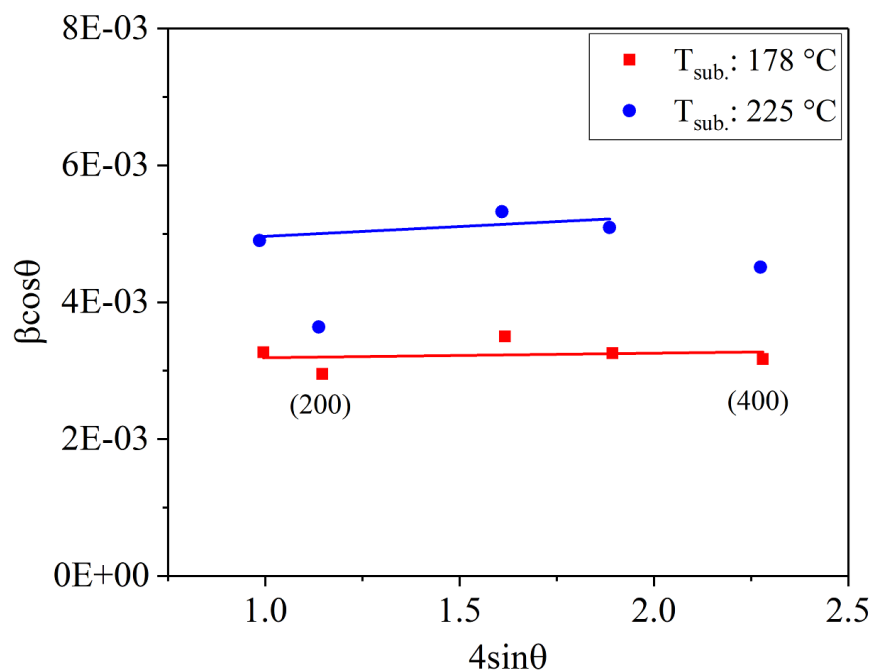


Figure 4.15: Williamson-Hall plot of GDC films deposited at different substrate temperatures.

Electrical properties of the GDC films were measured by 4-point DC conductivity (section 2.8.3). A schematic drawing of a prepared sample prior each measurement is shown in figure 4.16. The DC conductivity measurements were carried out within a temperature range of 500-800 °C with a heating-cooling rate of 3 °C/min in static air. Figure 4.17 shows electrical measurements of the GDC thin films and the 8YSZ substrate. Specifically, measured resistances of the GDC/8YSZ samples and the uncoated substrates are shown in figure 4.17-a. It is noteworthy, that even though the GDC films are significantly thinner than the substrates (*i.e.* 200  $\mu\text{m}$  thick.), the total resistance of the GDC/8YSZ is comparably lower than the substrate. Individually, for the GDC films the resistance was calculated based on the the assumption that the two components are connected in a parallel electrical circuit. Figure 4.17-b

shows the *total* conductivity ( $\sigma$ ) of the GDC films and the substrate which were estimated from the values of resistance employing the appropriate geometric factors. Total DC conductivities of 0.45 S/cm and 0.27 S/cm were measured at 600 °C for the GDC films deposited at  $T_{\text{sub.}}:225$  °C and  $T_{\text{sub.}}:178$  °C, respectively. This difference in conductivity between the GDC films indicates a substrate temperature dependence correlated with preferential oriented growth of the GDC film ( $T_{\text{sub.}}:225$  °C). Furthermore, it has been previously reported in the literature that higher conductivity values of GDC thin films were inherent to smaller grain sizes [134–136]. Hence, the high-conductivity values are sensible, due to the small grain size (<50 nm), for the GDC thin films presented in this study. However, it is still unclear whether electronic or ionic conductivity contributes the most, particularly for a *total* conductivity measured at higher temperatures than 500 °C.

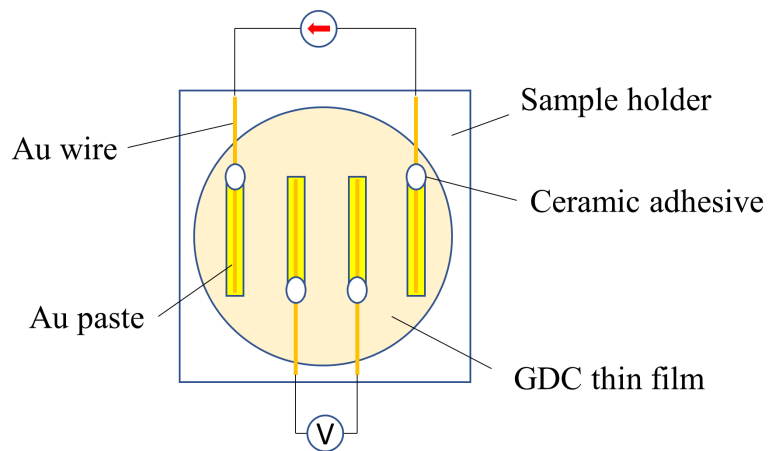
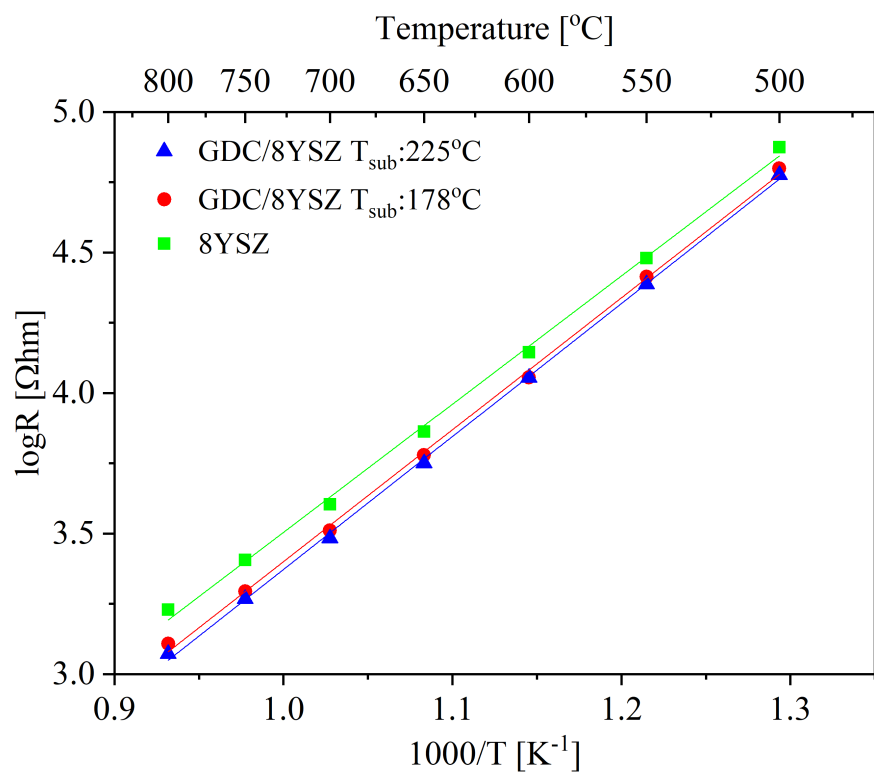
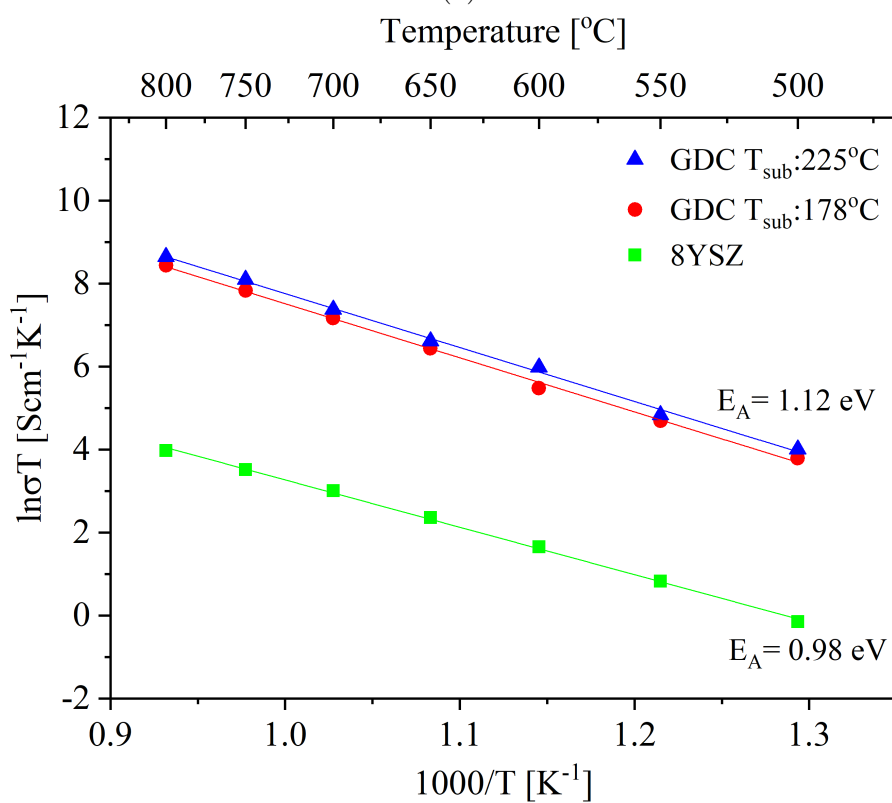


Figure 4.16: Schematic of gold electrical contacts integrated onto a GDC thin film for 4-point DC conductivity measurements.



(a)



(b)

Figure 4.17: Electrical measurements of GDC thin films and 8YSZ substrate: (a) total resistances of GDC/8YSZ and 8YSZ substrate; (b) conductivity of the GDC thin films and 8YSZ.

---

Taking into account the above results of the substrate temperature effect on YSZ and GDC films it has been found that at higher substrate temperatures a rougher morphology was obtained for the YSZ films while for the GDC films surface cracks were less pronounced. In addition, preferential orientation for both the YSZ and GDC thin films was favoured at higher substrate temperatures by intermittent spray deposition. This effect of substrate temperature seems to be directly correlated with a slower growth rate obtained at a higher substrate temperature and thus at a lower deposition rate. Moreover, for the GDC films measurements of 4-point DC conductivity revealed an enhanced total conductivity for the preferential (200) oriented film deposited at 225 °C. Therefore, controlling the substrate temperature shows the potential to produce nanostructured thin films with unique characteristics.

### 4.2.3 Precursor solution concentration

In spray pyrolysis one of the most important process parameters is the precursor solution concentration. Weber *et al.* [117] studied the effect of precursor solution concentration on morphology of various oxide films prepared by spray pyrolysis on dense substrates. From this work it was found that both the morphology of the films and substrate temperature range were dictated by precursor concentration. Specifically, for deposited YSZ films the authors observed as the precursor concentration was increased the minimum deposition temperature and roughness of the films were also increased. On the contrary, Beckel *et al.* [114] reported formation of smoother films from precursor concentrations of 0.04 mol/l instead of using 0.02 mol/l, due to more precipitates present within the incident droplets which influence their spreading behaviour on the substrate surface. Moreover, Chourashiya *et al.* [119] observed formation of gadolinia-doped ceria (GDC) films with lower roughness when they used a precursor concentration of 0.05 mol/l in contrast of using 0.04 mol/l. The authors attributed this effect on the increased number of nucleation sites which grow less compared to a decreased number of nucleation sites.

Chen *et al.* [137] investigated the effect of solution concentration on the morphology of YSZ thin films. At low concentrations a porous microstructure was obtained which shifted to a dense film morphology when a highly concentrated solution was used. This was attributed to surface and volume precipitation which occurs within the droplets leading to formation of either porous or dense solid particles, respectively. Messing *et al.* [44] proposed a model shown in figure 4.18 describing the effect of precipitation conditions on particle morphology prepared by spray pyrolysis.

According to this model, the aerosol droplets undergo evaporation of the solvent,

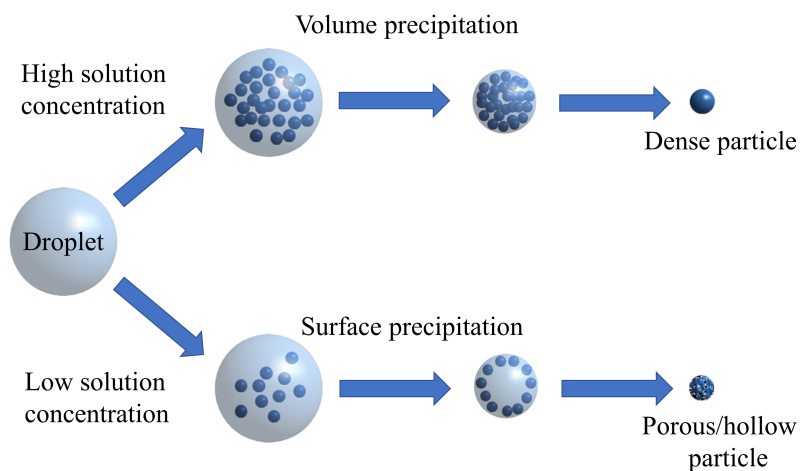


Figure 4.18: Schematic illustration of the precursor solution concentration effect on particle morphology by spray pyrolysis [44].

precipitation of solutes, thermal decomposition of the precipitate particles and sintering at even higher temperatures to form dense particles. Initially, size reduction of the droplet due to solvent evaporation results in a concentration gradient within the droplet. Close to the surface the concentration will be higher due to a faster evaporation rate than the rate of solute diffusion [44]. Therefore, at the onset of precipitation a solid crust will start to form at the periphery of the droplet. At high initial precursor concentrations and small size droplets precipitation is more likely to occur at a higher extent towards the center of the droplet, defined as volume precipitation. For low initial precursor concentrations droplets with a reduced amount of precipitates will engender formation of either a porous or a dense crust on droplet's surface. In case of a porous crust the remaining solvent will continue to evaporate leading to formation of a hollow particle. However, if the crust becomes dense enough to trap the remaining solvent, once the temperature exceeds

the boiling point of the solvent the gas pressure will increase breaking the crust and subsequently form a fractured particle. In both cases, this is known as surface precipitation leading to formation of either a hollow or a fractured particle.

Figure 4.19 shows different morphologies of 8YSZ particles based on volume and surface precipitation conditions.

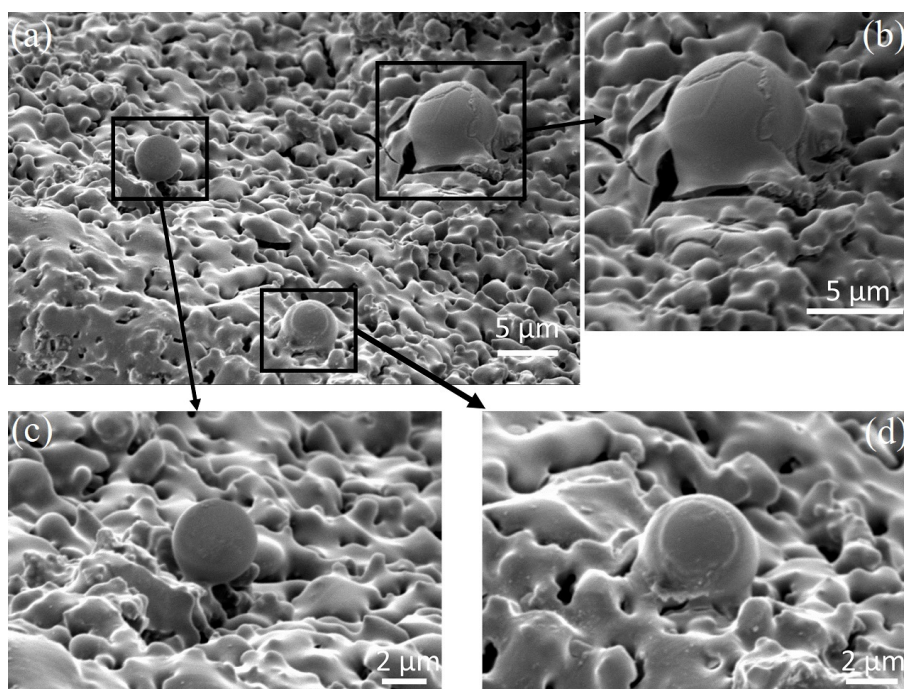


Figure 4.19: SEM micrographs in tilted view ( $45^\circ$ ) of 8YSZ particles formed during intermittent spray deposition onto porous 5LSM-3YSZ substrates showing the effect of volume and surface precipitation on particle morphology. Precursor concentration 0.1 mol/l, total deposition time 2.5 min with 30 sec/cycle, substrate temperature  $210^\circ\text{C}$ , precursor solution flow rate 0.6 ml/min, air flow rate 30 L/min, nozzle-to-substrate 25 cm, sintering at  $850^\circ\text{C}$  for 2 hours.

Specifically, spherical dense particles shown in figure 4.19c,d are the result of volume precipitation. In general, during solution atomization small and large droplets may collide to form even larger droplets. As a result, solid particles with different sizes will be produced (Fig.4.19a). The majority of small solid particles will splat

on the heated surface melt and coalesce gradually as deposition time increases to form a dense layer. However, under certain conditions (*e.g.* poor atomization) surface precipitation might also occur although a high precursor concentration is used. Figure 4.19b shows the effect of surface precipitation on particle morphology where the conditions were met to form a fractured particle.

Figure 4.20 shows different morphologies in top view of 8YSZ thin films deposited onto porous 5LSM-3YSZ cathode substrates. The solution precursor concentration was varied from 0.001 mol/l to 0.1 mol/l while deposition time was fixed at 100 min. Spray deposition of the prepared solution was performed at substrate temperature of 200 °C. Subsequently, the films were sintered at 500 °C and 850 °C for 2 hours to further investigate the effect of sintering temperature on film morphology. Crack free morphology was obtained for the films deposited with 0.001 mol/l and 0.005 mol/l sintered at 500 °C. However, the films have not fully covered the substrate as porous areas of the substrate are shown (Fig. 4.20a,b) due to low deposited mass. Applying higher precursor concentrations of 0.015 mol/l (Fig. 4.20e) and 0.025 mol/l (Fig. 4.20g) the morphology of the films shifted to a columnar structure with severe cracks. Due to a low substrate temperature the as-deposited films composed from a mixture of salts which have partially decomposed. Hence, upon post-thermal treatment and further decomposition of the precursor, volume change is greater provoking the formation of residual stresses and the appearance of cracks. Interestingly, subsequent sintering of the films at 850 °C for 2 hours had a minor effect on the morphology of the films which slightly increased their roughness due to an increase of the grain size.

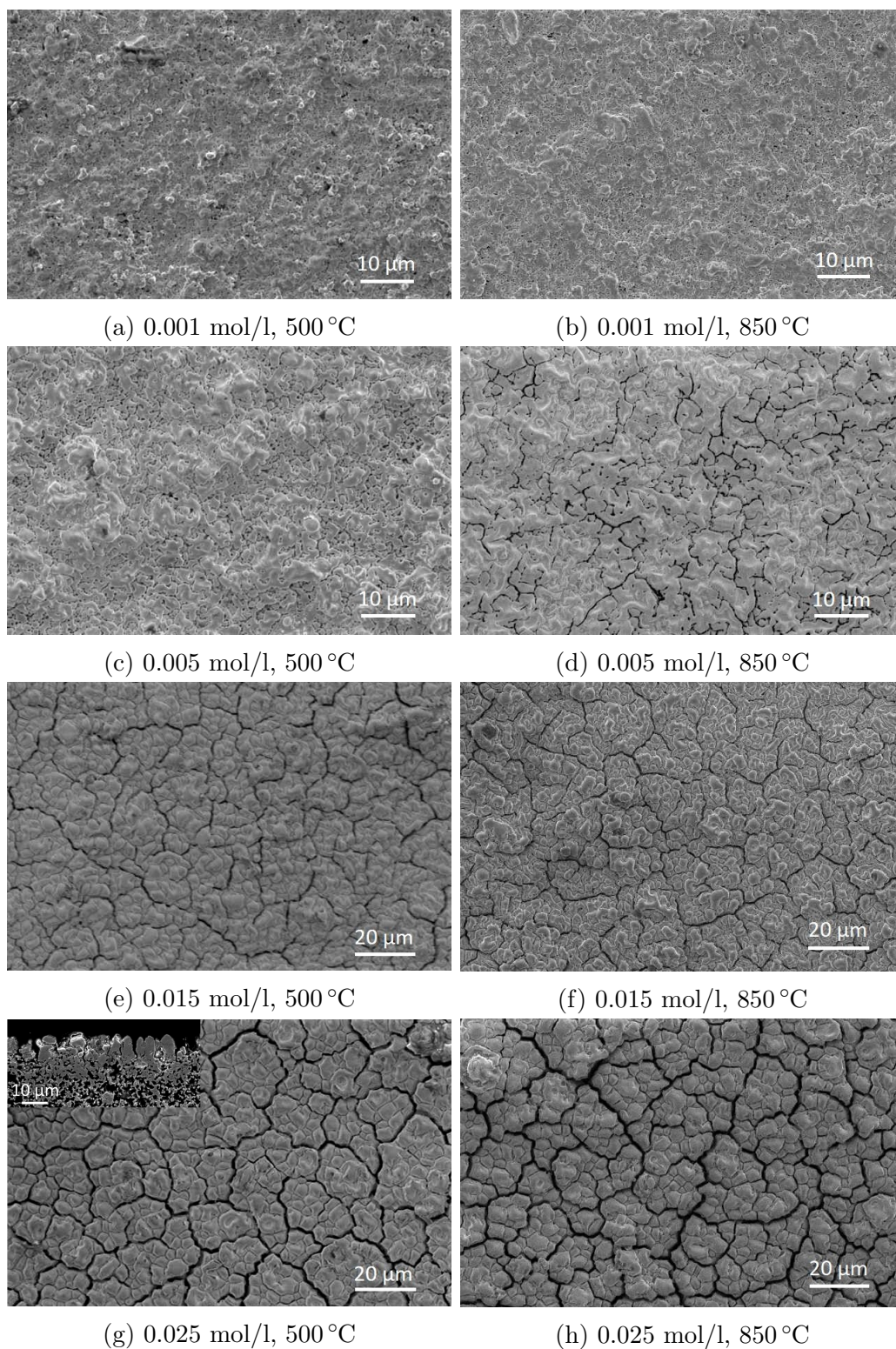


Figure 4.20: SEM micrographs in top view of 8YSZ thin films deposited on top of porous 5LSM-3YSZ substrates showing the effect of solution concentration and sintering temperature. Substrate temperature 200 °C, precursor solution flow rate 0.6 ml/min, air flow rate 30 L/min, deposition time 100 min, nozzle-to-substrate distance 25 cm, sintering at 500 °C and 850 °C for 2 hours.

In general, using higher precursor concentration leads to higher deposition rates and faster film growth [46, 54]. However, the formation of columnar grains grown perpendicular to the substrate (Fig. 4.20g) indicates a slow growth of the films where crystallites have to grow without each drop nucleating a new grain [116]. This mechanism is known as the *shadowing* effect and has been reported for thin films with columnar structure grown from the vapor phase [107, 138, 139]. A similar effect of the precursor concentration on the morphology of YSZ thin films was observed by Schlupp *et al.* [54]. A different precursor concentration of 0.005 M and 0.025 M which correspond to different growth rates, resulted in columnar and randomly oriented structures of 8YSZ films, respectively. It is noteworthy that Matsuzaki *et al.* [61] have also produced columnar YSZ thin films where growth of the films took place from the liquid phase and the precursors pyrolyzed *in situ*. However, the substrate temperature (*i.e.* 800 °C) was remarkably higher and the precursor concentration was not reported.

From the experimental results shown in figure 4.20 a suitable deposited mass and thus a critical thickness was determined resulting in a 8YSZ thin film with a crack free morphology (Fig. 4.20a,b). Adopting the latter, higher precursor concentrations were used adjusting the deposition time accordingly leading to faster growth rates. Figure 4.21 shows the effect of higher precursor concentration ( $>0.025$  mol/l) and thus higher growth rates on film's morphology which shifted from a columnar structure to smoother and denser structures. Spray deposition was carried out in intermittent spray cycles with a pause of 40 min at 500 °C and subsequent sintering at the same temperature and post-sintering at 850 °C for 2 hours. For precursor concentration of 0.1 mol/l deposition time was adjusted at 0.5 min per cycle and for 0.05 mol/l at 2 min per cycle. In total 5 cycles were performed for each precursor

concentration. In that way, residual stresses were minimized upon thermal decomposition of the precursor leading to a crack free morphology. Interestingly, the film deposited with a 0.1 mol/l precursor concentration shows fewer pinholes compared to the film deposited with a 0.05 mol/l, although the total deposited mass was lower. This can be explained by the lower extent of infiltration into the porous substrate and thus a denser film, due to larger particle sizes (section 4.2.5) obtained when a higher precursor concentration was used.

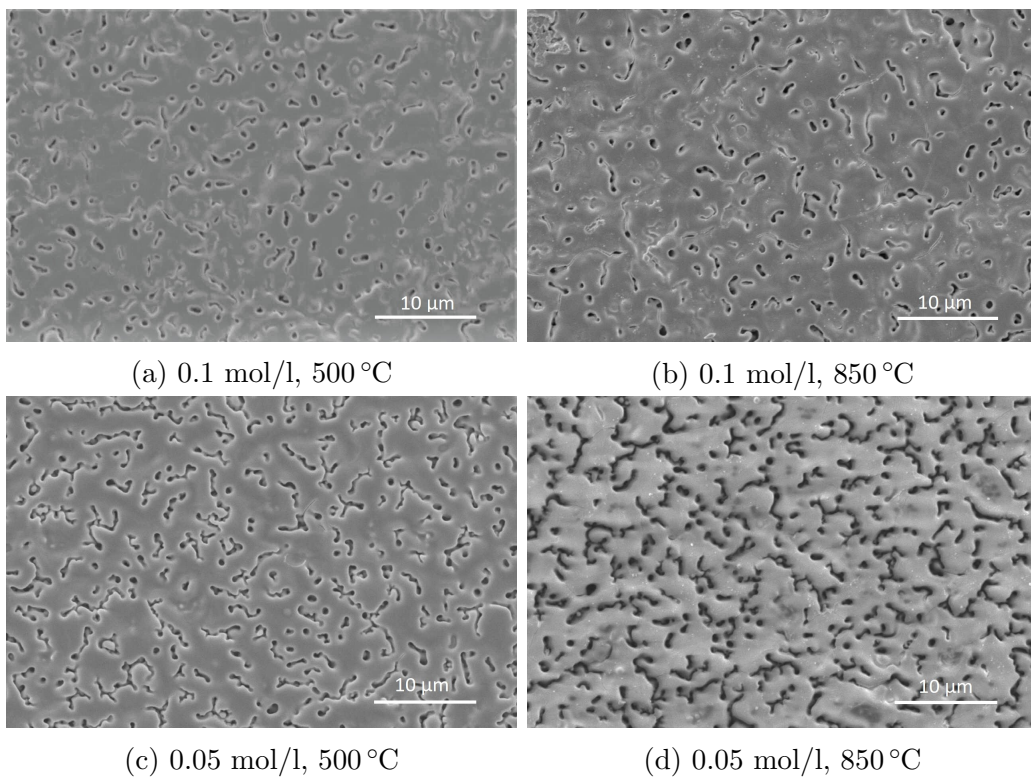


Figure 4.21: SEM micrographs in top view of 8YSZ thin films deposited on top of porous 5LSM-3YSZ substrates showing the effect of solution concentration and intermittent spray deposition (a,b) 0.1 mol/l, 30 sec/cycle, 5 cycles (c,d) 0.05 mol/l, 2 min/cycle, 5 cycles. Substrate temperature 210 °C, precursor solution flow rate 0.6 ml/min, air flow rate 30 L/min, nozzle-to-substrate 25 cm, sintering at 500 °C and 850 °C for 2 hours.

Figure 4.22 shows X-ray diffraction (XRD) patterns of the 8YSZ thin films deposited with different precursor concentrations (0.001 - 0.025 mol/l) obtained after post-sintering at 500 °C (fig. 4.22a) and 850 °C (fig. 4.22b) for 2 hours. The XRD pattern of the 5LSM-3YSZ used as a substrate is also shown as a reference to the peaks that appeared in each measurement. In addition, an indication of the film thickness can be concluded from the intensity of the substrate peaks which seems to gradually decrease as the precursor concentration increases and thus the thickness of the film. Analysis of the XRD patterns at 500 °C and 850 °C was performed using WinX<sup>POW</sup> software for the 8YSZ (0.025 mol/l) thin films and the lattice parameters are given in table 4.4. All the XRD patterns of the 8YSZ films correspond to a cubic fluorite crystal structure. The influence of the precursor concentration seems to be negligible and only to affect the intensity of the peaks as the thickness of the film increases. Additional sintering at 850 °C for 2 hours improved the crystallinity of the films as shown in figure 4.22b. Moreover, Scherrer equation was used to estimate the grain size which increased from 32 nm to 43 nm after sintering at 850 °C for 2 hours.

Table 4.4: Lattice & geometric parameters of the 8YSZ films. Precursor concentration 0.025 mol/l, deposition time 100 min, substrate temperature 200 °C, nozzle-to-substrate distance 25 cm.

Lattice parameter [ $\alpha$ (Å)]	Sintering temperature [°C]	Debye-Scherrer	Williamson-Hall	
		Grain size [nm]	Microstrain $\epsilon$ [%]	Grain size [nm]
5.1487(16)	500	32	0.04	39
5.1412 (7)	850	43	0.03	50

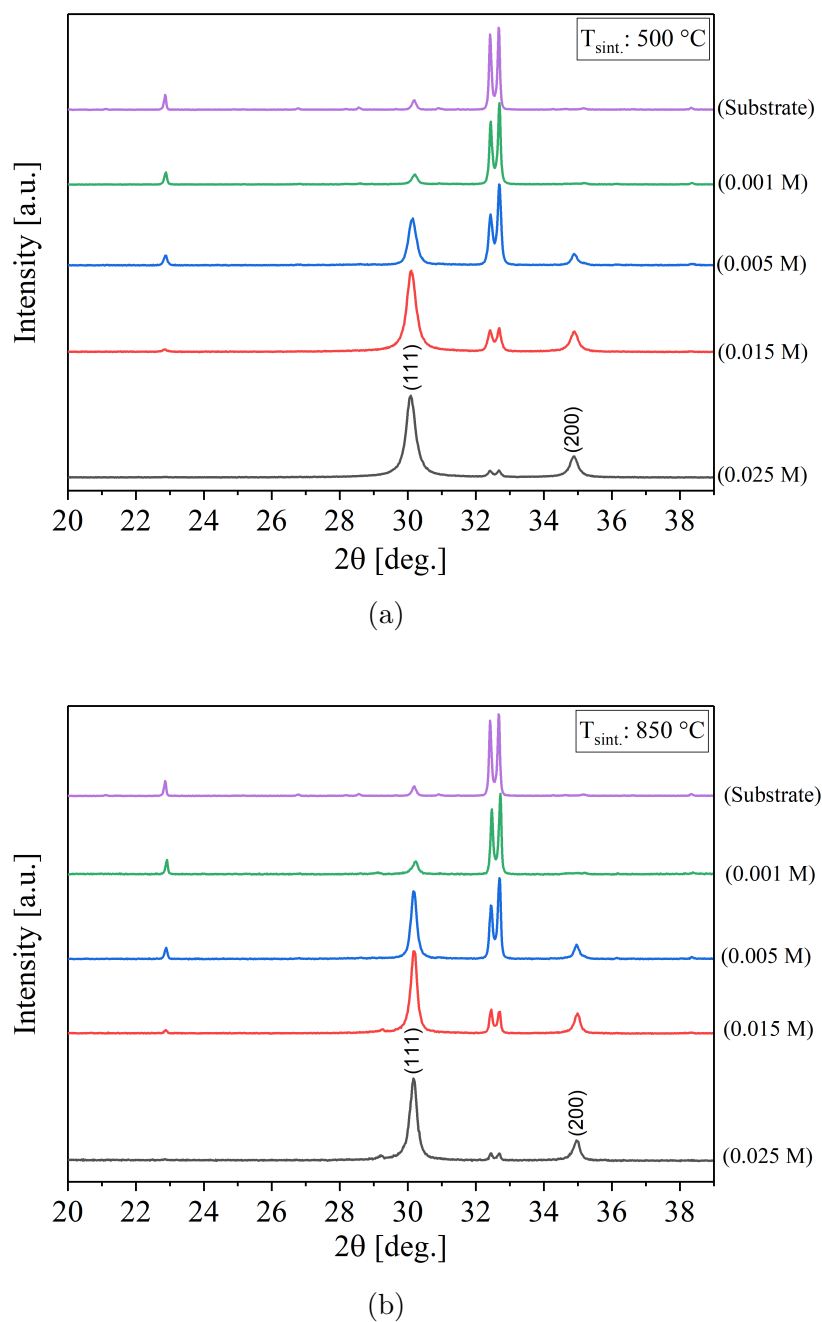


Figure 4.22: X-ray diffraction patterns of 8YSZ thin films deposited with different precursor concentrations onto porous 5LSM-3YSZ substrates (The 8YSZ peaks are denoted by Miller indices). Deposition time 100 min, substrate temperature  $200\text{ }^{\circ}\text{C}$ , solution flow rate 0.6 ml/min, air flow rate 30 L/min, nozzle-to-substrate distance 25 cm, sintered at  $500\text{ }^{\circ}\text{C}$  and  $850\text{ }^{\circ}\text{C}$  for 2 hours.

The Williamson-Hall method is employed to calculate and separate the strain from the grain size contribution to broadening of the XRD peaks. Figure 4.23 shows W-H plots of the 8YSZ film and the effect of sintering temperature. Using the equation (2.7) the microstrain ( $\varepsilon$ ) was calculated from the slope of the fit and the grain size from the y-intercept, listed in table 4.4. A microstrain relief from 0.04%, measured initially for the 8YSZ film sintered at 500 °C, to 0.03% after sintering at 850 °C for 2 hours was observed. This microstrain decrease seems to be related with a higher degree of crystallinity and a larger grain size obtained after sintering at a higher temperature in agreement with the literature [115, 122, 136].

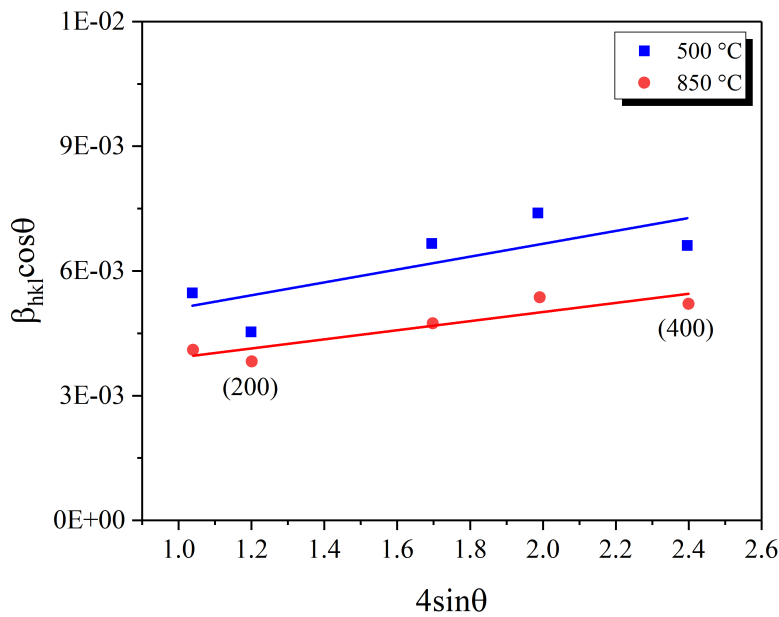


Figure 4.23: Williamson Hall plot of 8YSZ thin films deposited onto porous substrates of 5LSM-3YSZ showing the effect of sintering temperature on the strain of the films. Precursor solution concentration 0.025 mol/l, deposition time 100 min, substrate temperature 200 °C, solution flow rate 0.6 ml/min, air flow rate 30 L/min, nozzle-to-substrate distance 25 cm, sintering at 500 °C and 850 °C for 2 hours, respectively.

Based on the experimental results shown in this section it is clear that the process parameter of precursor concentration in spray pyrolysis has a strong effect on the morphology of the films. Specifically, using lower precursor concentrations and long deposition times ( $< 0.025$  mol/l, Fig.4.20) were found to form columnar structures of 8YSZ thin films. Nevertheless, a columnar structure of this type may not be suitable for electrolytes used in SOFCs that possibly will fail to be gas-tight. However, these structures exhibit an improved thermal shock tolerance and can be used for other applications (*e.g.* thermal barrier coatings) [107, 140]. In contrast, smooth and denser structures of 8YSZ thin films obtained when higher precursor concentrations and short deposition times ( $\geq 0.05$  mol/l, Fig.4.21) were applied. Therefore, application of 0.1 mol/l precursor concentration was found to be suitable for spray deposition of 8YSZ thin films to be used as SOFCs electrolytes.

#### 4.2.4 Deposition time

Deposition time is one of the process parameters of spray pyrolysis related with the deposited film mass and consequently the thickness of the film [43, 46, 47]. For a single cycle of film deposition there is a threshold thickness of the film above that cracks start to form as a result of the film shrinkage during thermal decomposition of the precursor [40, 72, 141, 142]. Therefore, it is important to estimate the maximum deposition time at a given precursor concentration for preparation of a thin film free from defects. Perednis *et al.* [46] studied the effect of the deposition time for YSZ films prepared by spray pyrolysis on dense substrates. However, no significant effect was found since the thickness of the film (*i.e.* 175 nm) was significantly lower compared to the 8YSZ film with a thickness of 9.7  $\mu\text{m}$  shown in figure 4.24d. This

observation supports the existence of an optimum film thickness in which no cracking occurs. The influence of deposition time on surface morphology of yttria-stabilized zirconia thin films deposited on porous cathode substrates at 200 °C and sintered *in situ* at 500 °C for 2 hours is shown in figure 4.24. For a short deposition time of 4 min the droplets landing on the substrate start to infiltrate and fill the pores of the substrate. The resulting film is coherent and exhibits a rough morphology with stacked irregular layers of gradual smaller surface areas (fig. 4.24a). As the deposition time increased to 20 min the morphology shifts to a cracked film due to tensile residual stresses formed during thermal decomposition of the precursor (fig. 4.24b). With a deposition time of 60 min cracks are expanded throughout the film and stacked layers start to grow into discrete 3D clusters (fig. 4.24c). After 100 min even though cracks are still present within the film the formed 3d clusters seem to increased in size and coalesce yielding a film with a columnar structure (fig. 4.24e). Interestingly, a columnar YSZ film morphology has been obtained from vapor deposition processes [107, 139]. However, the low substrate temperature during the spray deposition opposes this deposition mechanism indicating more likely a liquid phase deposition [42].

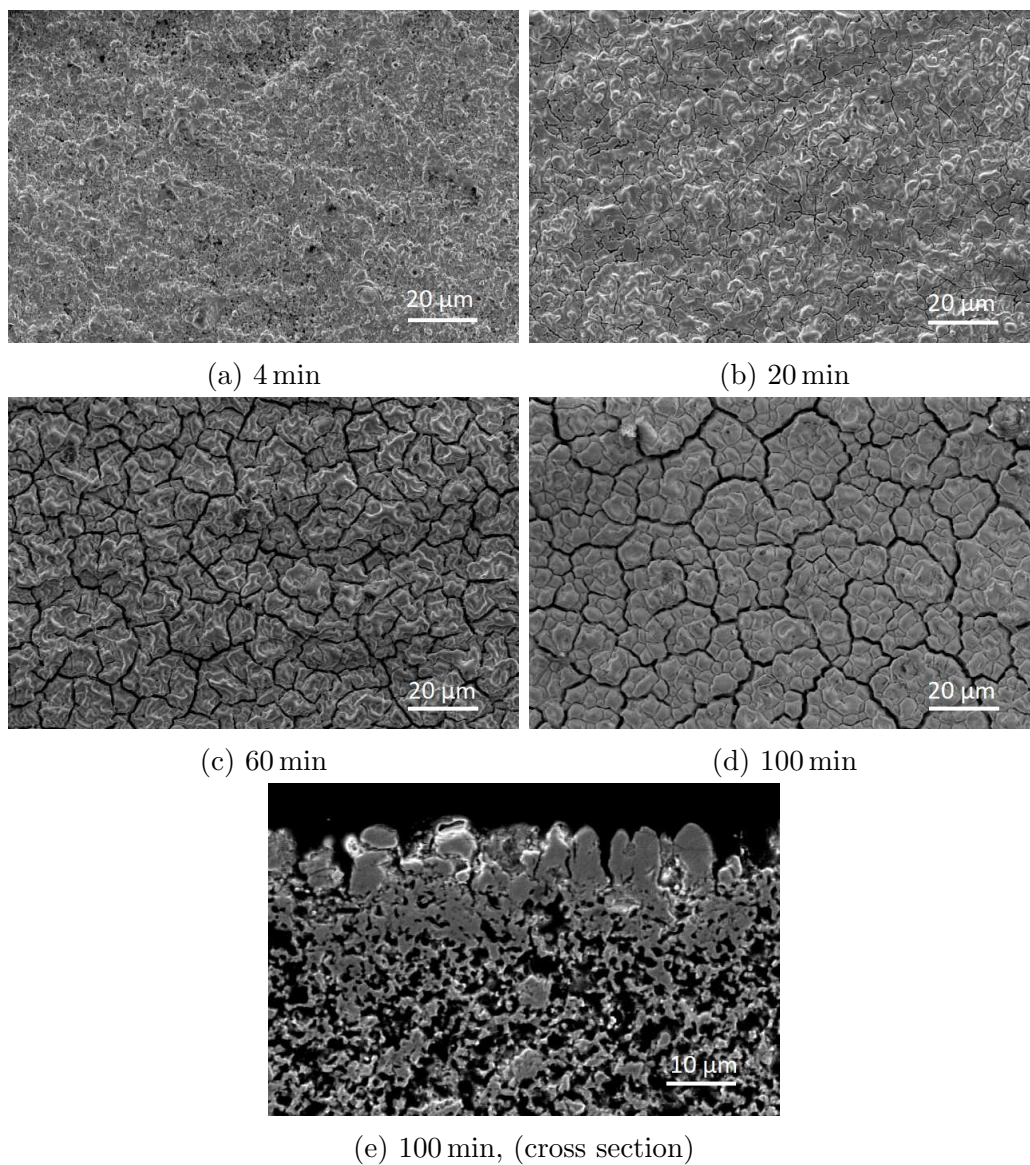


Figure 4.24: SEM micrographs in top view and cross section of 8YSZ thin films deposited on top of porous 5LSM-3YSZ substrates showing the effect of deposition time (a) 4 min (b) 20 min (c) 60 min (d) 100 min. Precursor solution concentration 0.025 mol/l, solution flow rate 0.6 ml/min, air flow rate 30 L/min, substrate temperature 200 °C, nozzle-to-substrate 25 cm, sintering at 500 °C for 2 hours.

Adopting the 4 min deposition time for a single spray deposition cycle, 8YSZ thin films were deposited in a series of cycles with a pause in-between at 540 °C for 20 min. Subsequently the samples were calcined *in situ* at 540 °C for 1 hour and post-sintered at 750 °C for 2 hours. Figure 4.25 presents the growth and morphology of 8YSZ thin films obtained after intermittent spraying deposition on porous 5LSM-3YSZ substrates. For a *total* deposition time of 40 min the 8YSZ film has not completely covered the porous surface of the substrate with pinholes being present. However, as the deposition time increases gradually the pinholes are completely covered by the sprayed pyrolyzed 8YSZ film resulting in completely dense structure as shown in figure 4.25c. Remarkably, the morphology of the films is coherent without any cracks in contrast with the films shown in figure 4.24b,c,d even though the *total* deposition time was either higher or equal. This can be explained from the intermittent spray deposition where each step leads to formation of individual monolayers which constitute the film. Therefore, during precursor decomposition fewer stresses are generated resulting in a crack free morphology (fig. 4.24a). In our case, it was difficult to determine the exact thickness of the film where cracks are not formed since the spray deposition took place on a porous substrate. Basically the first mono-layer infiltrates within the porous structure of the substrate explaining also the presence of porous areas in figure 4.24a. Therefore, to avoid formation of cracks in a film, deposition time should be kept within a range that will result to a film with a thickness lower than a critical value as mentioned earlier.

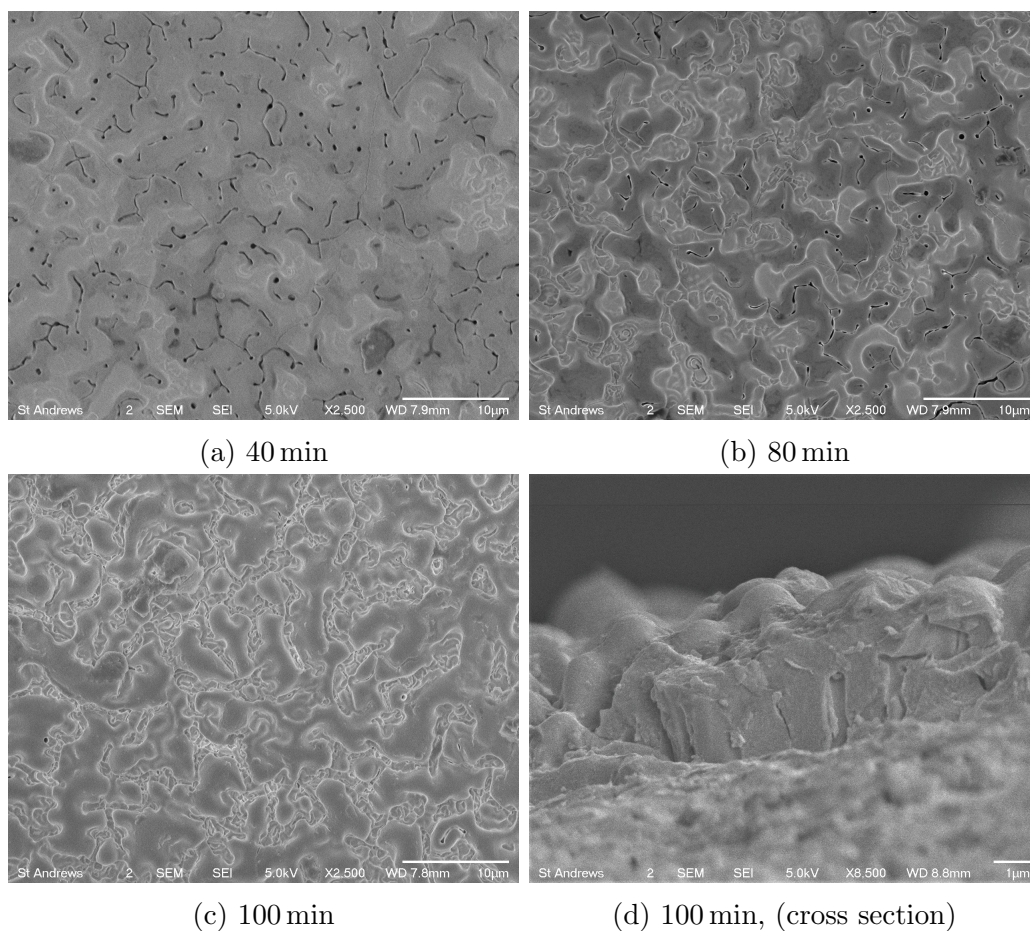


Figure 4.25: FEG-SEM micrographs in top view and cross section of 8YSZ thin films deposited onto porous 5LSM-3YSZ substrates showing the effect of deposition time and intermittent spray deposition: (a) 40 min (b) 80 min (c) 100 min. Deposition time per cycle 4 min, precursor concentration 0.025 mol/l, substrate temperature 170 °C, solution flow rate 0.6 ml/min, air flow rate 30 L/min, sintering at 750 °C for 2 hours.

Figure 4.26 shows X-ray diffraction patterns of 8YSZ thin films obtained after a continuous spray deposition for 100 min (Fig.4.24d,e) and intermittent spray deposition with 4 min per cycle and *total* deposition time of 100 min (Fig.4.25c,d). Substrate XRD peaks are also visible, thus the substrate's XRD pattern is also included in figure 4.22 as a reference. Both XRD patterns of the films are denoted by

Miller indices and matched to a cubic fluorite-type phase according to the literature (ICSD # 238375, Fm3m space group). A preferential (111) orientation was obtained for the 8YSZ film deposited with intermittent spray cycles. In contrast, a continuous spray deposition resulted in randomly oriented crystals of the film. The difference in structural order reveals the controlling factor is the dividing of the deposition time in short segments which results to a different growth mechanism, morphology and to preferential orientation of the film.

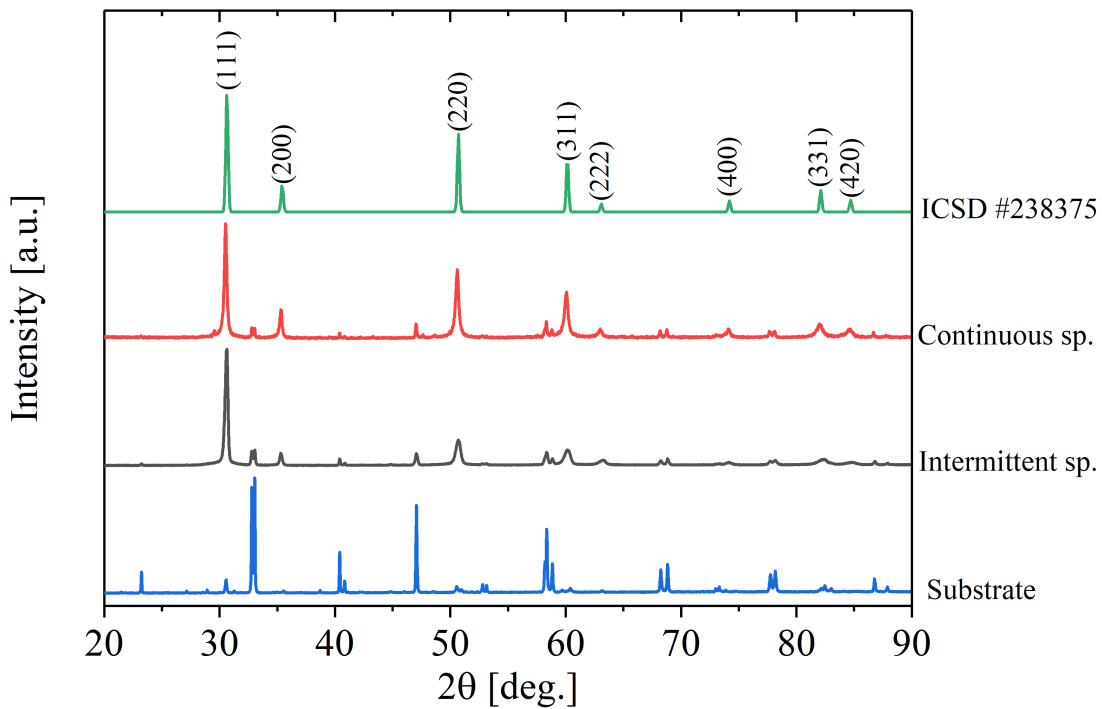
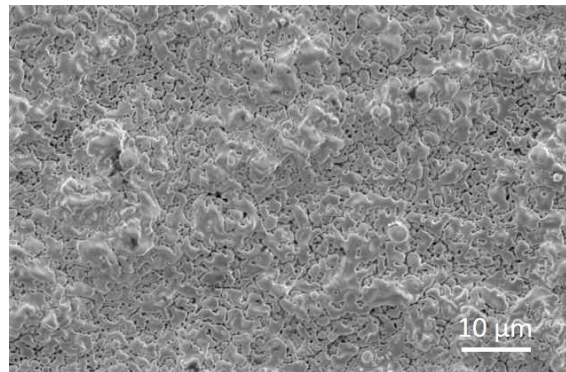


Figure 4.26: X-ray diffraction patterns of 8YSZ thin films deposited on 5LSM-3YSZ substrates showing the effect of continuous spray deposition and intermittent spray deposition (deposition time: 4 min/cycle, 25 cycles) on preferential crystal orientation. Precursor solution concentration 0.025 mol/l, *total* deposition time 100 min, solution flow rate 0.6 ml/min, air flow rate 30 L/min, nozzle-to-substrate 25 cm.

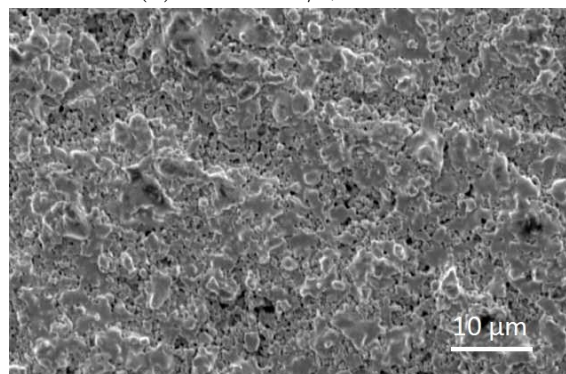
### 4.2.5 Precipitate particle size

In order to improve the deposition rate of the film a precursor solution with a higher solution concentration and a shorter deposition time is encouraging and facilitates the formation of dense and smooth films due to an increased density of precipitate particles [43, 46, 114]. Moreover, one of the requirements to avoid crack formation within a film is to minimise residual stresses during the spray deposition of the precursor solution. Initially, this can be accomplished at a low deposition rate by using a diluted precursor solution and long deposition times to deposit a mass that will result in a film, free from cracks as shown in figure 4.27a. Instead, a higher precursor concentration and a shorter deposition time can also be used to form a film with the same thickness improving the deposition rate as shown in figure 4.27b.

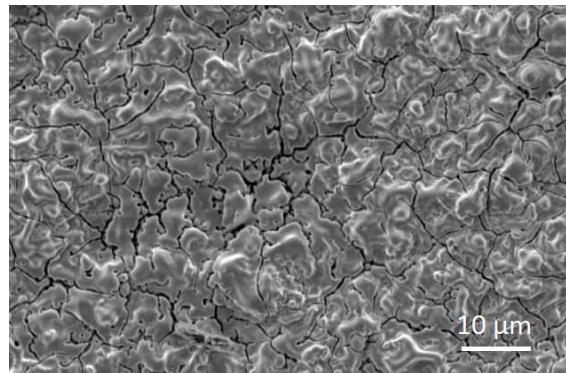
However, comparing the morphologies of YSZ films in figure 4.27(a,c), it can be seen that although the deposited mass was the same in both cases (0.103g) by adjusting the deposition time, cracks were formed for the sample presented in the third micrograph. This can be explained by the differences in incident precipitate particle sizes where a higher solution concentration after solvent evaporation will result in larger precipitate particles size [43]. It seems that since the spray deposition of the 0.025 mol/l precursor solution was carried out on a porous substrate larger precipitate particles were not infiltrated within the substrate as much as the smaller particles derived from the 0.005 mol/l precursor solution leading to formation of a thicker film. This finding can be an overlooked argument in the literature for explanation of the origin of cracks in a film deposited on a porous substrate. Therefore, it is more important not to exceed a critical thickness rather than a deposited mass to obtain a film free from cracks on porous substrates.



(a) 0.005 mol/l, 100 min



(b) 0.025 mol/l, 4 min



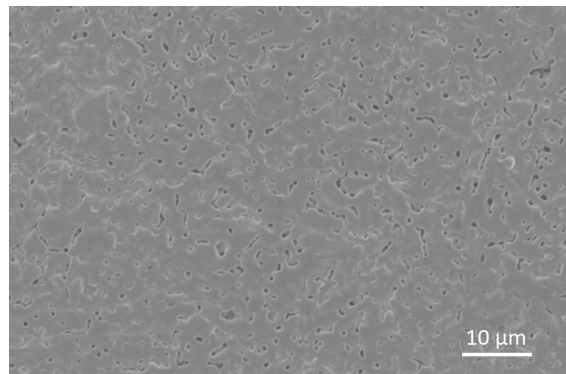
(c) 0.025 mol/l, 20 min

Figure 4.27: SEM micrographs in top view of 8YSZ thin films deposited on top of porous 5LSM-3YSZ substrates showing the effect of precipitate particles size: (a) 0.005mol/l for 100 min (b) 0.025 mol/l for 4 min (c) 0.025 mol/l for 20 min. Substrate temperature 200 °C, precursor solution flow rate 0.6 ml/min, air flow rate 30 L/min, nozzle-to-substrate 25 cm, sintering at 500 °C for 2 hours.

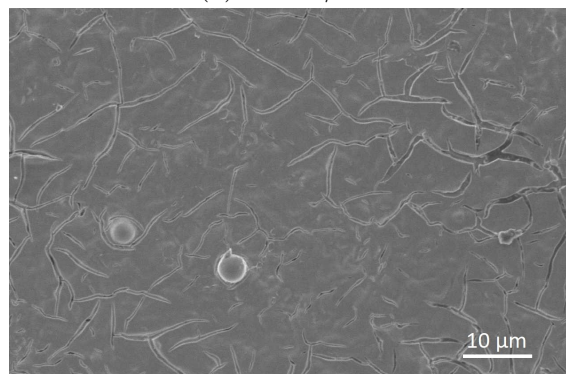
### 4.2.6 Precursor solution flow rate

The precursor solution flow rate affects the rate of incident droplets on the substrate at a given deposition time [56]. Thus, at high flow rates a larger quantity of material will also be deposited increasing the deposition rate of the film [72]. However, excess accumulation of liquid on the surface of the substrate will take longer time to evaporate generating stresses during the evaporation of the solvent with detrimental effects on the morphology of the films [121]. Therefore, it is crucial to identify the maximum precursor solution flow rate that leads to the formation of a film without any defects.

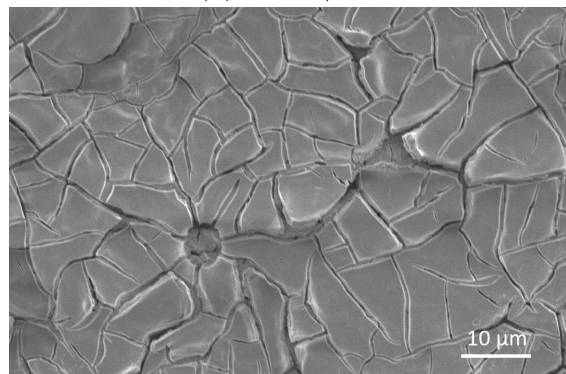
The influence of the precursor solution flow rate on the YSZ film morphology is shown in figure 4.28. Spray deposition was carried out in intermittent cycles of 30s followed by thermal treatment *in situ* at 500 °C for 40 min. At the end of the 5<sup>th</sup> cycle the deposited 8YSZ film was calcined on the hot plate at 500 °C for 2 hours. Due to the high precursor concentration of 0.1 mol/l a short deposition time of 30 sec was set and a flow rate of 1 ml/min to avoid formation of cracks as shown in figure 4.28a. In contrast, as the precursor flow rate increased cracks started to appear in the film (fig. 4.28b) with even delamination of the film to occur at even higher flow rates of 2.7 ml/min as shown in figure 4.28c. In these cases, evaporation of the solvent is slower, resulting in residual stresses and film cracking, due to larger and richer in solvent incident droplets on the substrate as the precursor flow rate increases [56,143]. Moreover, minor variations of the flow rate (*e.g.* 0.6 ml/min, fig. 4.25) as long as it doesn't exceed 1 ml/min (present work) have a negligible effect on crack formation within a film prepared by spray pyrolysis in agreement with the literature [46,114].



(a) 1.0 ml/min



(b) 1.5 ml/min



(c) 2.7 ml/min

Figure 4.28: SEM micrographs in top view of 8YSZ thin films deposited in steps of 30 sec with 40 min of pause at 500 °C, on top of 5LSM-3YSZ substrates showing the effect of precursor solution flow rate (a) 1.0 ml/min (b) 1.5 ml/min (c) 2.7 ml/min. Precursor solution concentration 0.1 mol/l, air flow rate 30 L/min, substrate temperature 220 °C, *total* deposition time 2.5 min, nozzle-to-substrate 25 cm, sintering at 500 °C for 2 hours.

### 4.2.7 Spray gun nozzle-to-substrate distance

The nozzle-to-substrate distance ( $D_{sp}$ ) is a process parameter that affects the evaporation rate of the droplets, the coating area and eventually the deposition rate [42, 56]. For small distances the droplets are more likely to be rich in solvent and evaporate too slowly once they reach the substrate resulting in a cracked film with poor adhesion. Furthermore, the deposition rate will be higher and the coating area ( $A_{sp}$ ) will be smaller which is also dependent on the spray cone angle ( $\theta$ ) [113]. For an ideal conical shape, the coating area can be calculated according to  $A_{sp} = 2D_{sp} \tan(\theta/2)$  to give an estimation of the substrates area that can be used. However, high flow rates of the pressurized air used to atomize the precursor solution into fine droplets cools down the substrate. Thus, additional heat from the hot plate is required in order to achieve the optimum substrate temperature. Therefore, the minimum spray nozzle to substrate distance is limited by the cooling effect of the air stream. On the other hand, at high distances some of the droplets will evaporate well before reach the substrate forming powder particles. In figure 4.29 shows this effect where the nozzle-to-substrate distance increased to 36 cm. The formed particles are large in size (*i.e.*  $\text{Ø}20 \mu\text{m}$ ) and exhibit poor adhesion creating craters that penetrated the thin film (fig.4.29b,c). Moreover, the coating area was increased to approximately 30% decreasing the deposition rate. In contrast, at a distance of 25 cm there was no powder formation of this extent resulting into electrolyte films that meet the gas-tight requirement for use in SOFCs. Consequently, even though at 36 cm the film shows no evidence of cracks (Fig. 4.29d) the formation of large powder particles restricts the use of this distance to 25 cm as an optimum nozzle-to-substrate distance.

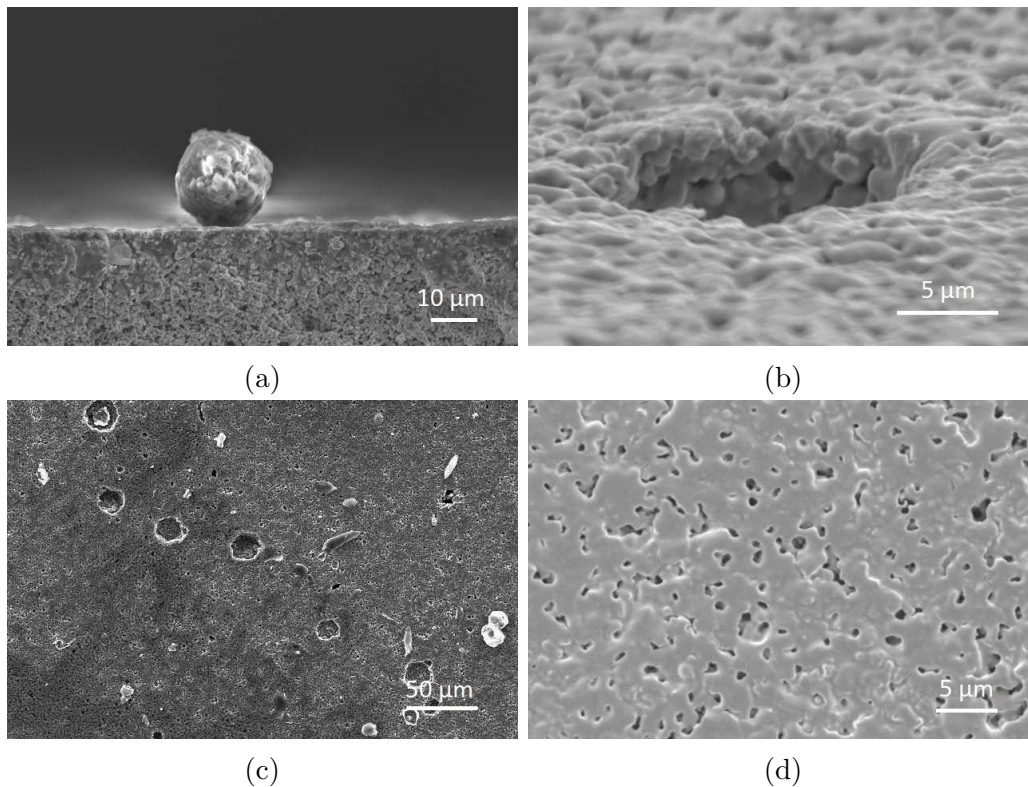


Figure 4.29: SEM micrographs (a) in cross section and (b,c,d) in top view of 8YSZ thin films deposited on top of porous 5LSM-3YSZ substrates showing the effect of a higher nozzle-to-substrate distance. The spray gun nozzle was fixed at 36 cm from the substrate. Precursor solution concentration 0.1 mol/l, substrate temperature 220 °C, solution flow rate 0.6 ml/min, air flow rate 30 L/min, deposition time 5 min, sintering at 750 °C for 2 hours.

## 4.3 Conclusions

Spray pyrolysis technique was employed to deposit YSZ and GDC thin films for application in SOFCs. Optimization of the spray pyrolysis parameters was carried out using exclusively aqueous precursor solutions of the appropriate metal nitrates. The process parameters of substrate temperature, precursor concentration, deposition time, solution flow rate and spray nozzle-to-substrate distance were studied. Emphasis was given on the effect of the above parameters and how to avoid the formation of defects in order to obtain the required dense and gas-tight film morphology. A summary of the experimental results is given in table 4.5. The main process parameter which determines the film morphology it is the precursor concentration. The higher the concentration is the shorter the deposition time per spray cycle should be to obtain a crack free film morphology at low substrate temperatures. In general, high concentrated solutions (*e.g.* 0.1 mol/l) and short deposition times per cycle are preferable for deposition of dense and smooth thin films. On the other hand, low precursor concentrations (*e.g.* 0.005 mol/l) and long deposition times lead to rather porous morphologies than dense which are more suitable for SOFC electrodes. Substrate temperatures  $>200\text{ }^{\circ}\text{C}$  lead to formation of rougher film morphologies, lower deposition rates and even particle formation with adverse effects on the structure of the films. Nozzle-to-substrate distances greater than 25 cm should be avoided due to particle ( $\sim 20\text{ }\mu\text{m}$ ) formation on the surface of the film and poor deposition efficiency. Solution flow rate has a negligible effect on the morphology of the films as long as it is lower than 1 ml/min. Based on the above, it was shown that dense films suitable for use in SOFCs can be successfully obtained by spray pyrolysis at sintering temperatures as low as  $750\text{ }^{\circ}\text{C}$ .

Table 4.5: Summary of the spray pyrolysis process parameters effect on the morphology of YSZ and GDC thin films.

Material	Precursor conc. [mol/l]	Dep. time [min]	Cycles [nr.]	Substrate temperature [°C]	Flow rate [ml/min]	Distance [cm]	Sintering [°C]	Film morphology
YSZ	0.1	19.5	39	170	0.6	25	900	Dense, smooth
YSZ	0.1	19.5	39	210	0.6	25	900	Dense, rough
GDC	0.1	4.0	12	178	0.6	25	850	Surface cracks
GDC	0.1	4.0	12	225	0.6	25	850	Surface cracks
YSZ	0.001	100	1	200	0.6	25	500,850	Coherent
YSZ	0.005	100	1	200	0.6	25	500,850	Coherent
YSZ	0.015	100	1	200	0.6	25	500,850	Cracked, columnar
YSZ	0.025	100	1	200	0.6	25	500,850	Cracked, columnar
YSZ	0.05	2.5	5	200	0.6	25	500,850	Pinholes, smooth
YSZ	0.1	2.5	5	200	0.6	25	500,850	Pinholes, smooth
YSZ	0.025	4.0	1	200	0.6	25	500	Coherent
YSZ	0.025	20	1	200	0.6	25	500	Cracked
YSZ	0.025	60	1	200	0.6	25	500	Cracked, columnar
YSZ	0.025	100	1	200	0.6	25	500,850	Cracked, columnar
YSZ	0.025	40	10	170	0.6	25	540,750	Pinholes, smooth
YSZ	0.025	80	20	170	0.6	25	540,750	Pinholes, rough
YSZ	0.025	100	25	170	0.6	25	540,750	Dense, rough
YSZ	0.1	2.5	5	220	1.0	25	500	Pinholes, smooth
YSZ	0.1	2.5	5	220	1.5	25	500	Cracked
YSZ	0.1	2.5	5	220	2.7	25	500	Cracked, delaminated
YSZ	0.1	5.0	1	220	0.6	36	750	Coherent, large particles (>10 $\mu\text{m}$ )



# Spray pyrolysis strategy for thin film SOFC electrolytes and electrodes

## 5.1 Introduction

The development of a cost-effective method with the potential to fabricate thin ( $< 10 \mu\text{m}$ ) and gas tight electrolyte films for use in solid oxide fuel cells at low sintering temperatures have been always an immense challenge [144]. Siemens-Westinghouse successfully demonstrated tubular cathode-supported SOFCs incorporating  $40 \mu\text{m}$  8YSZ film electrolytes initially prepared by electrochemical vapor deposition (EVD) and later by atmospheric plasma spray (APS) [15]. However, these fabrication techniques are quite expensive in terms of cost equipment, labor and maintenance related with mass production [39].

On the other hand, conventional methods (*e.g.* screen printing, tape casting) which have been well established on a large scale require elevated processing temperatures ( $1400^\circ\text{C}$ ) to fully densify the electrolyte [145]. Thus, the preparation of cathode-supported SOFC by these methods is limited due to the formation of zirconate phases at the LSM/YSZ interface and subsequent performance degradation

of the cell [146].

Spray pyrolysis is a versatile and cost-effective method that enables the formation of thin films at low post-sintering temperatures [42]. Early in the 1990s, Setoguchi *et al.* demonstrated electrochemical results from cathode-supported SOFCs with thin electrolytes of YSZ (18  $\mu\text{m}$  thick) [147] and calcia-stabilized zirconia (CSZ, 33  $\mu\text{m}$  thick) [14], prepared by spray pyrolysis at a post-sintering temperature of 1000  $^{\circ}\text{C}$ . The key strategy adopted by the authors was to spray the precursor solution in cycles with intermediate heating at 600  $^{\circ}\text{C}$  before the final sintering step at 1000  $^{\circ}\text{C}$ . This repeated sequence enabled tensile stresses to be relieved upon thermal decomposition of the precursor and also to repair previous defects of the film. Most recently, deposition of YSZ [25] and GDC [26], thin electrolytes also prepared by spray pyrolysis with promising electrochemical performance for anode-supported SOFC has been reported.

In the present work, spray pyrolysis was employed using environmentally friendly aqueous solutions to deposit in intermittent spray cycles, thin film SOFC components (*i.e.* cathode interlayer, electrolyte and anode) on cathode substrates of LSM-YSZ sintered to temperatures up to 950  $^{\circ}\text{C}$ .

## 5.2 Modification of substrate surfaces

Initially, for the preparation of 8YSZ thin films on porous cathode substrates of LSM-YSZ spray deposition was carried out in 30 intermittent spray cycles of 30 sec. Precursor concentration was 0.1 mol/l, the solution was supplied to the spray gun at a flow rate of 0.6 ml/min and it was atomized into a fine aerosol by compressed air at flow rate of 30 l/min, substrate temperature was 220  $^{\circ}\text{C}$  during spray deposition

and increased to 500 °C after each cycle for 40 min and every 10 cycles for 2 hours. The morphology of the 8YSZ thin film is shown in figure 5.1. Remarkably, a dense and crack-free electrolyte film was obtained at a low sintering temperature of 500 °C. However, spray deposition with the aforementioned process parameters resulted in the formation of a thin film with a significant thickness variation from 0.6 μm to 1.25 μm as can be seen in figure 5.1b. The high porosity (42%) and roughness of the cathode substrates in conjunction with pore sizes up to 2 μm (fig. 5.1b, 5.2a) is the main reason for the formation of the 8YSZ film with a non-uniform thickness.

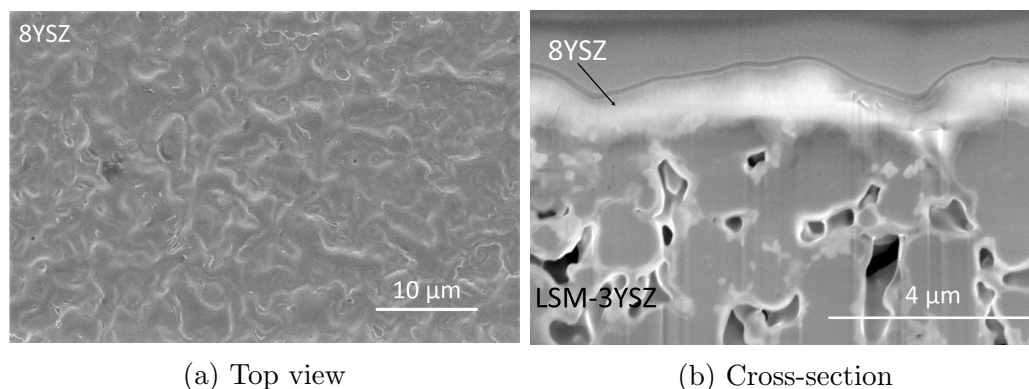


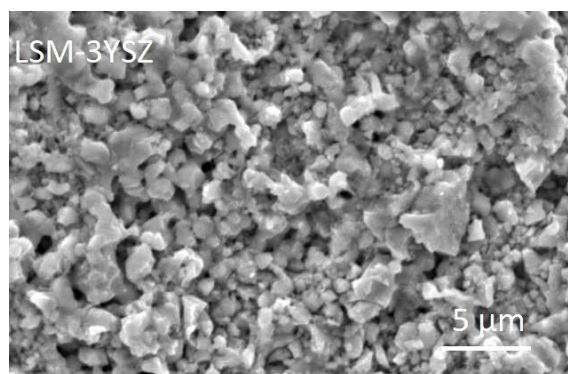
Figure 5.1: SEM micrographs in top view and cross section of 8YSZ thin film (0.6-1.25 μm) deposited onto porous cathode substrate of 5LSM-3YSZ. Precursor solution 0.1 mol/l, deposition time 15 min, number of spray cycles 30, Substrate temperature 220 °C, nozzle-to-substrate distance 25 cm, sintering temperature 500 °C for 2 hours.

In addition, the deposition rate is quite low and also varied from 2.4 μm/h to 5 μm/h corresponding to each thickness. To obtain a more uniform film thickness and to improve the deposition rate the surface of the substrate was modified by spraying an intermediate layer of the  $\text{La}_{0.8}\text{Sr}_{0.2}\text{MnO}_3$ . Steele *et al.* [148], investigated the concept of a modified cathode/electrolyte ( $\text{La}_{0.6}\text{Sr}_{0.4}\text{Co}_{0.2}\text{Fe}_{0.8}\text{O}_{3-x}/\text{CGO}$ ) interface and the effect on area specific resistivity (ASR) of the cathode. The authors found that the ASR was reduced by a factor of 2-3 by addition of a dense

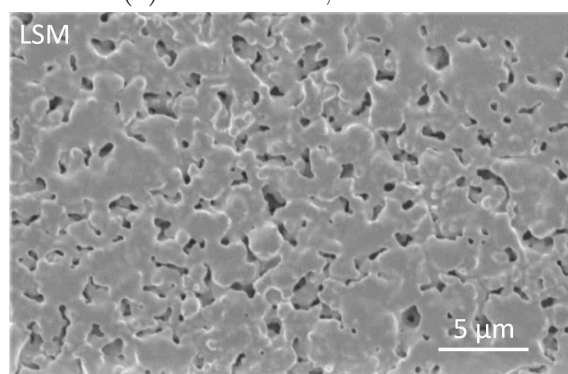
thin ( $\sim 1 \mu\text{m}$ ) interlayer of LSCF. This improvement was attributed to an increase of the effective interfacial area between the LSCF and the electrolyte that accelerate the charge-transfer reactions at the interface. The merits of a gradient porous microstructure for an LSM cathode produced by a multi-step spray pyrolysis, were also reported by Hamedani *et al.* [149,150].

An aqueous precursor solution was prepared by dissolving metal nitrates of  $\text{La}(\text{NO}_3)_3 \cdot 6\text{H}_2\text{O}$ ,  $\text{Sr}(\text{NO}_3)_2$  and  $\text{Mn}(\text{NO}_3)_2 \cdot x\text{H}_2\text{O}$  with a total ion concentration of 0.025 mol/l. Substrate temperature was  $200^\circ\text{C}$  during spray deposition. Spray deposition was performed in 5 cycles with a deposition time of 2 min per cycle. After each spray cycle the substrate temperature increased to  $540^\circ\text{C}$  for 20 min and for 1 hour at the end of the last spray cycle, subsequently the samples were sintered at  $750^\circ\text{C}$  for 2 hours in a muffle furnace. Thus, the surface morphology of the cathode support shifted from rough and highly porous to a smoother and less porous surface area as shown in figure 5.2b. Afterwards, intermittent spray deposition of 8YSZ aqueous precursor solution with a concentration of 0.1 mol/l resulted in the formation of a smooth and crack-free electrolyte (fig. 5.2c) after sintering at  $750^\circ\text{C}$  for 2 hours. The presence of few pinholes is due to a low total deposition time of 10 min which can be easily eliminated by increasing the number of spray cycles.

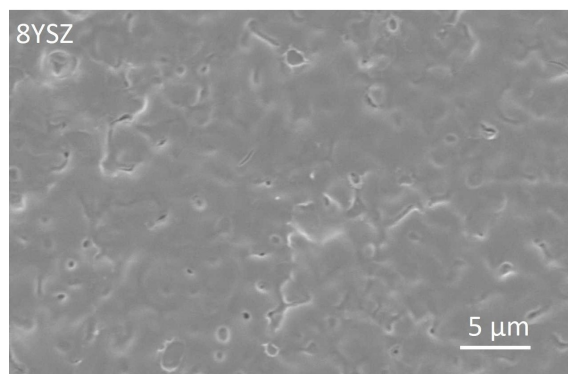
In figure 5.3 an 8YSZ electrolyte with a more uniform thickness (*i.e.* 2.4-2.8  $\mu\text{m}$ ) obtained after spray deposition of a precursor solution of 0.1 mol/l on a porous cathode substrate of LSM-3YSZ with a modified top surface. For the spray deposition of the intermediate layer of LSM the same process parameters applied as mentioned above. Moreover, the deposition rate of the 8YSZ electrolyte was significantly improved to 11.2  $\mu\text{m}/\text{h}$ . Therefore, a modification of the substrate surface is highly recommended prior to spray deposition of an electrolyte thin film.



(a) 5LSM-3YSZ, Substrate

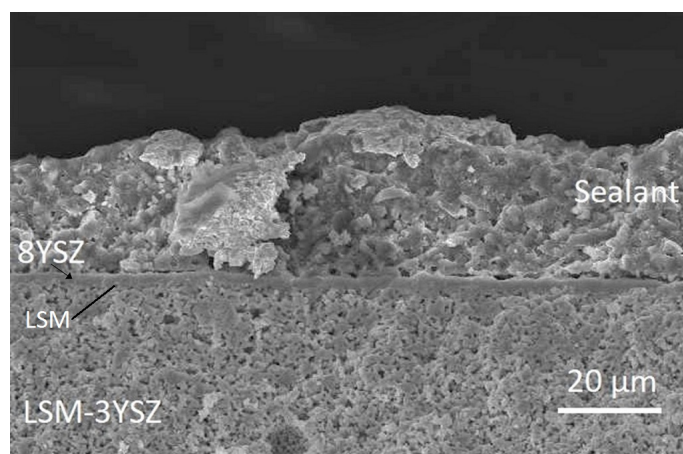


(b) LSM, Thin interlayer

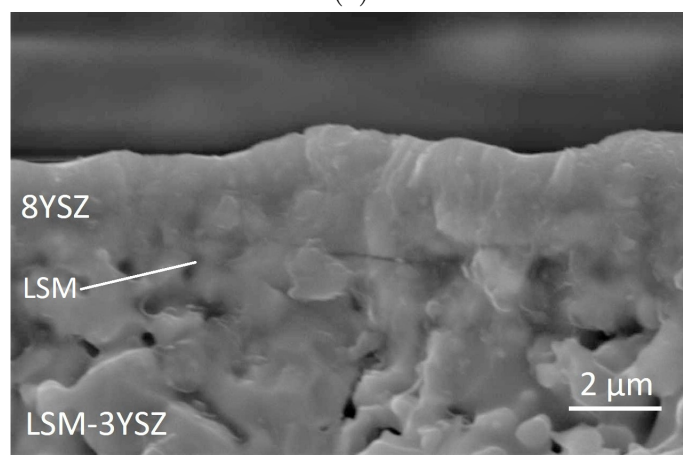


(c) 8YSZ, Thin film

Figure 5.2: Modification of the porous cathode substrate surface by spray deposition of  $\text{La}_{0.8}\text{Sr}_{0.2}\text{MnO}_3$  thin interlayer and subsequent spray deposition of a 8YSZ thin electrolyte: a) 5LSM-3YSZ(9:1 wt.%), sintered at 1200 °C for 2 hours b) precursor concentration 0.025 mol/l, deposition time 10 min, 5 spray cycles, substrate temperature 200 °C, sintering at 750 °C for 2 hours, c) precursor concentration 0.1 mol/l, deposition time 10 min, 20 spray cycles, substrate temperature 200 °C, Nozzle-to-substrate distance 25 cm, solution flow rate 0.6 ml/min, air flow rate 30 l/min, sintering at 750 °C for 2 hours.



(a)



(b)

Figure 5.3: SEM micrographs in cross section of 8YSZ thin electrolyte (2.4-2.8  $\mu\text{m}$ ) deposited onto a porous cathode substrate of 5LSM-3YSZ with an interlayer of LSM. Precursor concentration 0.1 mol/l, substrate temperature 200  $^{\circ}\text{C}$ , deposition time 15 min, 30 spray cycles, solution flow rate 0.6 ml/min, air flow rate 30 l/min, nozzle-to-substrate distance 25 cm, sintering temperature 750  $^{\circ}\text{C}$  for 2 hours with a heating-cooling rate of 3  $^{\circ}\text{C}/\text{min}$ .

### 5.3 Deposition of thin electrolytes by spray pyrolysis

For the deposition of thin gas-tight electrolytes, spray pyrolysis was employed using the experimental apparatus described previously in section 2.1. To reduce the surface porosity of the 5LSM-3YSZ (9:1wt.%) substrates a thin film of  $\text{La}_{0.8}\text{Sr}_{0.2}\text{MnO}_3$  (LSM) was sprayed and sintered prior to the deposition of the electrolyte films. Alternatively, less porous 5LSM-8YSZ (1:1 wt.%) substrates were used without the intermediate layer of LSM. Aqueous precursor solutions were prepared with a molar ratio of 85.2(Zr):14.8(Y) to obtain a thin film with the required stoichiometry of  $(\text{Y}_2\text{O}_3)_{0.08}(\text{ZrO}_2)_{0.92}$ . The total ion concentration was varied from 0.05 mol/l to 0.1 mol/l. The morphology and chemical composition of the produced films were characterized by field-emission gun scanning electron microscopy (FEG-SEM) and energy dispersive X-ray spectroscopy (EDS), respectively. To determine the crystallinity, crystal orientation and grain size of the films X-ray diffraction, transmission electron microscopy and electron diffraction were employed.

Figure 5.4 shows the FEG-SEM micrographs in cross section of a thin 8YSZ electrolyte sprayed on top of an interlayer of LSM supported on a porous substrate of 5LSM-3YSZ. For the deposition of the LSM a precursor solution with a concentration of 0.025 mol/l was used. Total deposition time was 14 min and spray deposition was performed in 7 intermittent cycles. Between each cycle substrate temperature increased from 170 °C to 540 °C for 20 min. Subsequently, the samples were sintered at 750 °C for 2 hours. In figure 5.4b the LSM layer is visible with nano-particles infiltrating into the porous substrate, retaining the triple phase boundary area. Afterwards, a precursor solution of 8YSZ with a total concentration

of 0.1 mol/l was intermittently sprayed at a substrate temperature of 170 °C. The resulted thickness of the electrolyte film was 5.7 μm after sintering at 750 °C and the deposition rate was 13.7 μm/h. Based on the type of the sealing material (*e.g.* pyrex glass or ceramic adhesive) and the sealing temperature of these materials the sintering temperature of the SOFC thin films was set accordingly. In some cases pyrex<sup>®</sup> glass was used as a sealant the sintering temperature of the electrolyte films was higher than 750 °C since this material softens at 821 °C and starts to seal. It is noteworthy, that spray deposition in short cycles (*i.e.* 30 s) produced electrolyte films which constitute by vertical columnar crystals. A similar columnar structured 8YSZ thin film ( $\sim 1.7$  μm thick.) was also obtained by intermittent spray deposition at a higher substrate temperature of 210 °C on porous cathode substrates of LSM-8YSZ (fig. 5.5). However, for this experiment 8YSZ instead of LSM was initially sprayed with a lower solution concentration of 0.05 mol/l and longer deposition time of 2 min for each spray cycle. Thus, a more concentrated solution of 0.1 mol/l was deposited afterwards to continue the growth of the 8YSZ film. The samples calcined at 540 °C *in situ* between each cycle and sintered at 900 °C for 2 hours.

This type of morphology is commonly found in thin films prepared by other methods such as pulsed laser deposition (PLD) [122, 151], aerosol-assisted chemical vapour deposition (AA-CVD) [54] and plasma spray physical vapor deposition (PS-PVD) [107, 139]. However, this is the first time reported to obtain similar columnar structures of 8YSZ by air-pressurised spray pyrolysis at a substrate temperature as low as 170 °C. Schulpp *et al.* [152] investigated the effect of preferentially and randomly crystal orientated 8YSZ thin films on cross plane conductivity. The authors found that the cross plane conductivity increased two orders of magnitude at 500 °C for the columnar structured films.

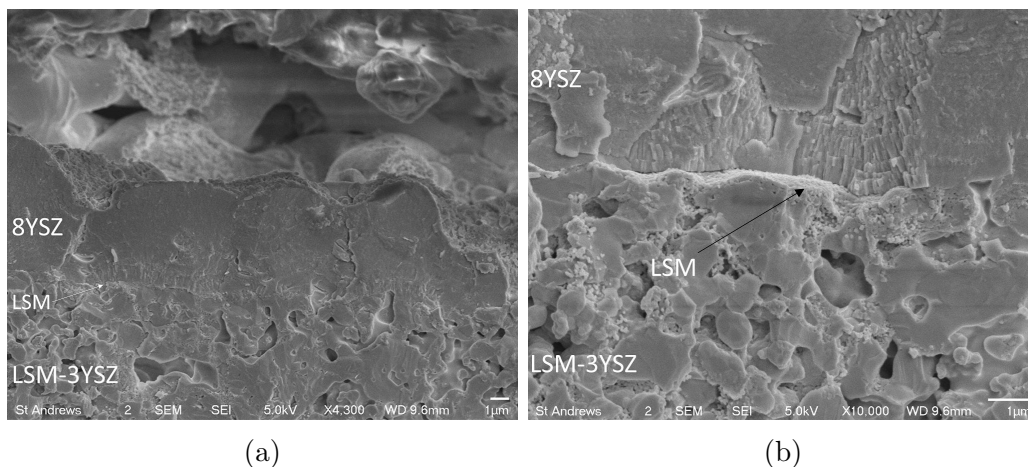


Figure 5.4: FEG-SEM micrographs in cross section of 8YSZ thin films (5.7  $\mu\text{m}$  thick.) deposited on sprayed interlayer of LSM supported on porous cathode substrates of 5LSM-3YSZ. Precursor concentration 0.1 mol/l, deposition time 25 min, 50 spray cycles, substrate temperature 170  $^{\circ}\text{C}$ , solution flow rate 0.6 ml/min, air flow rate 30 l/min, nozzle-to-substrate distance 25 cm, sintering at 750  $^{\circ}\text{C}$  for 2 hours.

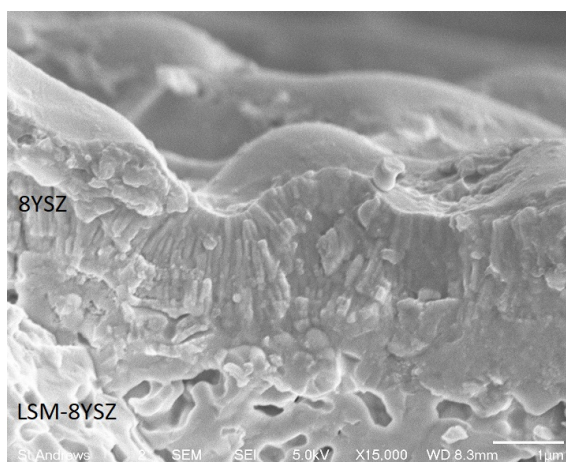


Figure 5.5: FEG-SEM micrograph in cross section of 8YSZ thin electrolyte deposited on porous cathode substrate of 5LSM-8YSZ(1:1 wt.%). Precursor concentration 0.05 mol/l, deposition time 2.5 min, 5 spray cycles, Precursor concentration 0.1 mol/l, deposition time 11.5 min, 23 spray cycles, substrate temperature 210  $^{\circ}\text{C}$ , solution flow rate 0.6 ml/min, air flow rate 30 l/min, nozzle-to-substrate 25 cm, sintering at 900  $^{\circ}\text{C}$  for 2 hours.

Thin films of 8YSZ prepared by spray pyrolysis were further characterised by transmission electron microscopy (TEM). Slices (lamellas) of 8YSZ films were extracted and polished by focused ion beam (FIB, FEI Scios DualBeam FIB/SEM) technique for TEM (FEI Titan Themis 200) analysis. The sample in figure 5.6b during TEM preparation was cut to include the anode electrode of the SOFC and thus, only a part of the 8YSZ electrolyte is shown. TEM micrographs in cross section shown in figure 5.6a,b reveal preferential oriented crystals of 8YSZ, grown perpendicular on the substrate. It is noteworthy that this preferential orientation was obtained also after thermal treatment at only 500 °C (fig. 5.6a) indicating that the spray deposition in cycles is favouring the formation of orientated films irrespective of the sintering temperature. However, the dimensions of the 8YSZ crystals are significantly different. Approximately, a width of 35 nm and 150 nm in length measured for the 8YSZ crystals sintered at 500 °C while a width of 47 nm and 300 nm in length measured for the 8YSZ crystals sintered at a higher temperature of 900 °C.

In addition, due to this strategy the films consist of multiple consolidated layers in a single uniform 8YSZ thin film. Closed porosity with nano-sized pores ( $\sim 5$  nm) appear in the microstructure of the films located especially in areas between the intermittently deposited layers. These negligible defects formed most likely during thermal decomposition of residual nitrates. Similar microstructure and defects were also observed by Schlupp *et al.* [153] for 8YSZ thin films prepared by intermittent chemical vapor deposition. The authors attributed the formation of porosity to the composition of the atmosphere above the substrate surface which becomes saturated with solvent and precursor molecules and their decomposition products. Electron diffraction pattern in figure 5.6c shows the films are crystalline with a preferen-

tial (111) orientation. The selected area electron diffraction pattern in figure 5.6d indicates the films consist of single crystals.

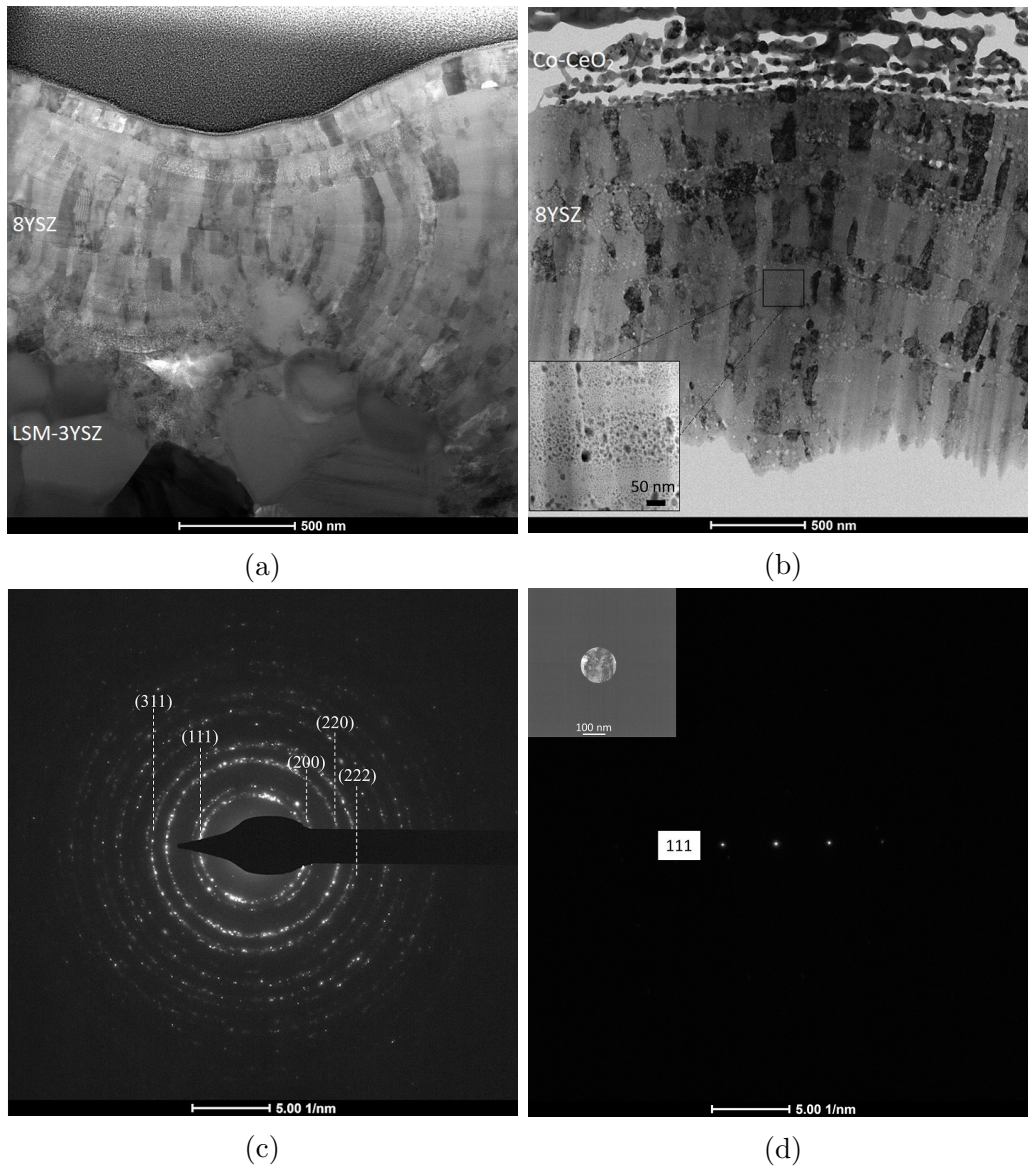


Figure 5.6: TEM micrographs in cross section of 8YSZ thin films a) deposited at 220 °C and sintered at 500 °C b) deposited at 170 °C and sintered at 900 °C c) Electron diffraction pattern of 8YSZ preferential(111) oriented film d) Selected area electron diffraction (SAED) pattern of a single crystal 8YSZ.

To determine the thermal expansion coefficient of a 8YSZ thin film variable-temperature X-ray diffraction (VT-XRD) patterns were obtained in air using a Panalytical empyrean diffractometer (Mo,  $K_{\alpha 1,2}$ ) equipped with a high temperature furnace. The sample was initially sintered at 750 °C for 2 hours. Measurements were performed within a temperature range of 25-950 °C and an isotherm of 60 min at each temperature with a heating rate of 5 °C/min (fig. 5.7). Using WinXPOW software the  $K_{\alpha 2}$  peaks were stripped from the VT-XRD patterns and the lattice parameter ( $\alpha$ ) of the cubic YSZ crystal structure was calculated using equation 2.3 for the (111) diffraction peak at each temperature. Respectively, thermal expansion coefficient for the 8YSZ film at each temperature are given in table 5.1.

Table 5.1: Thermal expansion coefficient of a 8YSZ film deposited on porous cathode substrate of 5LSM-3YSZ at various temperatures. (Mo,  $K_{\alpha 1}$ )

Lattice parameter [ $\alpha$ (Å)]	Temperature [°C]	Thermal expansion coefficient $10^{-6}$ [K $^{-1}$ ]
5.125	25	
5.159	650	10.6
5.166	750	11.0
5.175	850	11.8
5.194	950	14.6

The effect of heat treatment on crystallization, microstrain and grain growth of a 8YSZ thin film is shown in figure 5.8 and table 5.2. The XRD patterns for both sintering temperatures and lattice parameters estimated using WinXPOW software match a cubic fluorite crystalline phase (ICSD #238375) indicating a fully stabilized zirconia. The 8YSZ film sintered at 950 °C exhibits sharper XRD peaks and is better crystalline. At this temperature preferential (111) orientation becomes stronger as the intensities of the peaks are relative smaller to the 111 peak intensity comparably

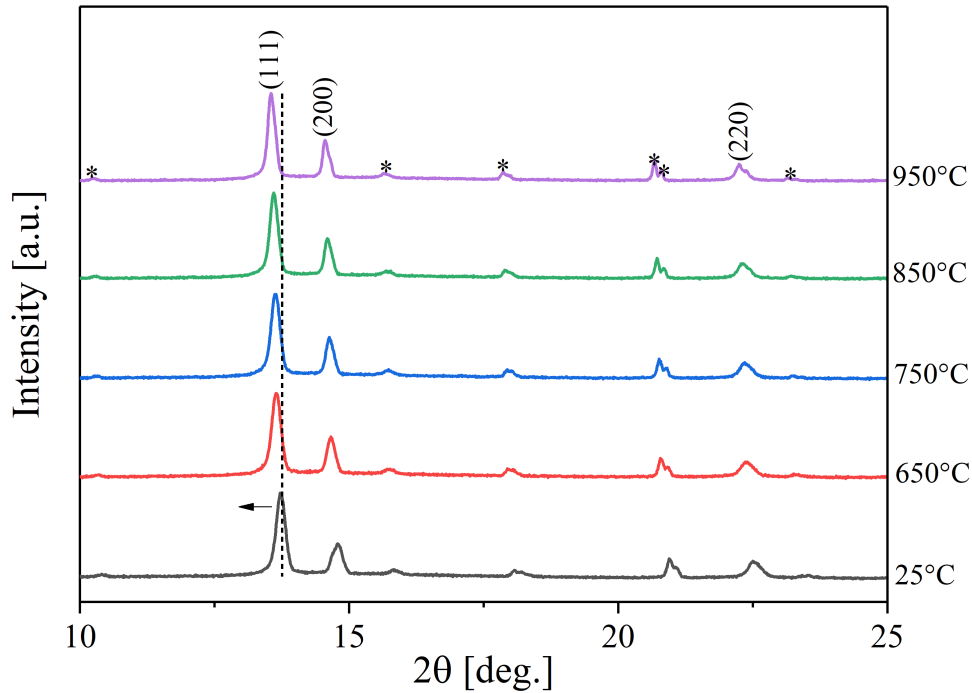


Figure 5.7: Variable temperature X-ray diffraction (VT-XRD) patterns of a 8YSZ thin film sintered initially at 750 °C for 2 hours. An isotherm of 1 hour was kept at each temperature during the measurement (Mo,  $K_{\alpha 1,2}$ , \* corresponds to substrate peaks).

with the XRD pattern obtained at 750 °C. An increase of the grain size from 31 nm to 54 nm was observed after sintering at 950 °C, using Scherrer equation. To determine the effect of sintering temperature on the microstrain of the 8YSZ film, Williamson-Hall plots were produced from the XRD patterns shown in figure 5.8a. From the slope of the fit for each temperature a decrease in the microstrain ( $\epsilon$ ) was observed from 0.13% to 0.05% at 950 °C. This reduction in microstrain is attributed to a better crystalline material with an improved structural order obtained at a higher temperature [122].

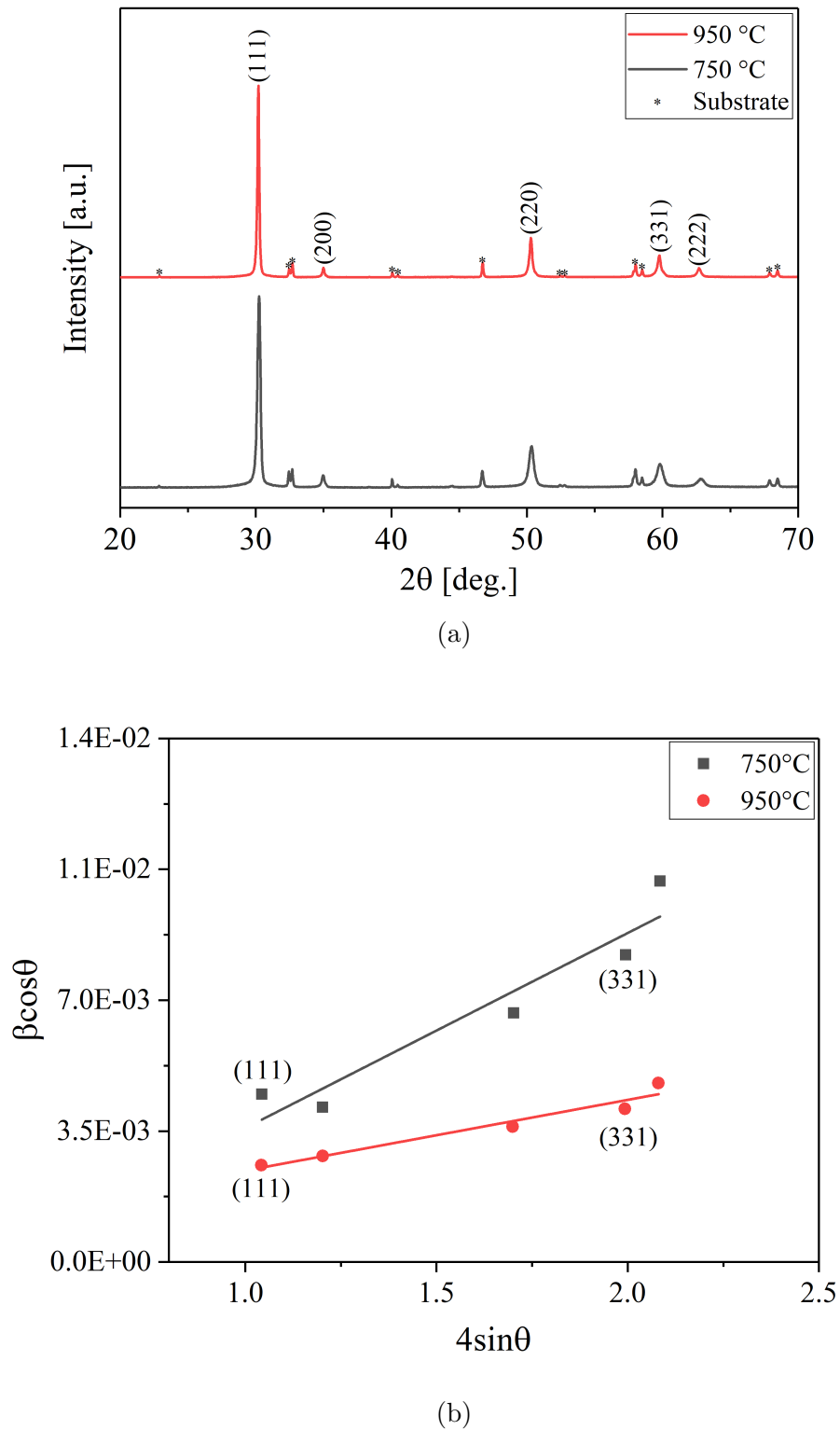
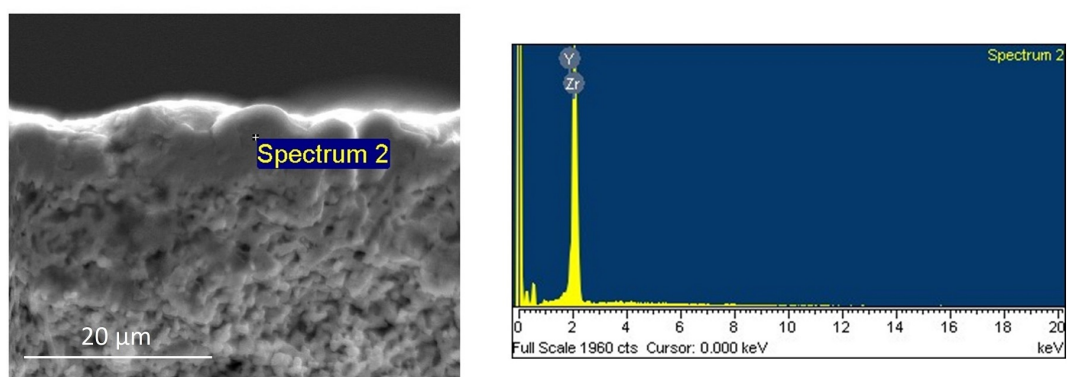


Figure 5.8: X-ray diffraction patterns of 8YSZ thin films in (a) and the corresponding Williamson-Hall plots in (b) sintered at 750 °C for 2 hours and 950 °C for 1 hour, respectively. Precursor solution 0.1 mol/l, total deposition time 25 min, 50 spray cycles, substrate temperature 170 °C, nozzle-to-substrate distance 25 cm.

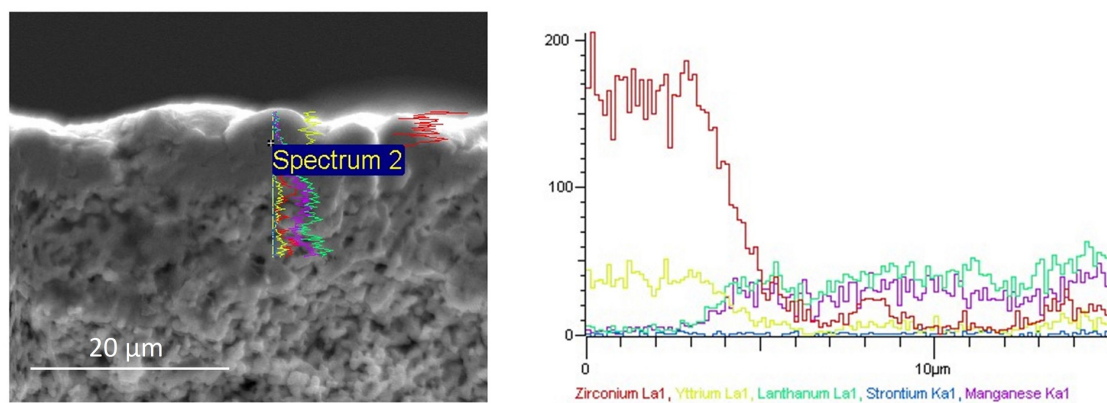
Table 5.2: Effect of sintering temperature on lattice & geometric parameters of a 8YSZ film deposited onto porous 5LSM-3YSZ substrate. Precursor concentration 0.1 mol/l, deposition time 25 min, 50 spray cycles, substrate temperature 170 °C, nozzle-to-substrate distance 25 cm.

Lattice parameter [ $\alpha$ (Å)]	Sintering temperature [°C]	Grain size [nm]	Microstrain $\varepsilon$ [%]
5.1350 (4)	750	31	0.13
5.1347 (5)	950	54	0.05

EDS analysis was carried out to determine the chemical composition of 8YSZ thin films prepared by spray pyrolysis. Figure 5.9a shows the EDS spectrum of a pure 8YSZ film corresponding to 84.36 at.% for Zr and 15.64 at.% for Y in good agreement with the nominal composition (85.2-Zr:14.8-Y at.%). In addition, an EDS line-scan in figure 5.9b shows a uniform chemical composition and the thickness of the film which is 5.5  $\mu\text{m}$ . An improved deposition rate of 16.5  $\mu\text{m}/\text{h}$  was obtained for this film due to sintering at 950 °C and larger particle growth compared to the previous film (fig. 5.4) where sintering took place at 750 °C. For this experiment a 20 mm porous substrate of 5LSM-3YSZ was used to deposit the electrolyte. The surface of the substrate was modified with an intermediate layer of LSM coated prior the spray deposition of the electrolyte as described earlier (section 5.2). It should be noted, the substrate temperature was 175 °C during the LSM deposition and the film was sintered at 950 °C for 2 hours. For the spray deposition of the 8YSZ film a precursor solution of 0.1 mol/l was used. Total deposition time was 20 min and the 8YSZ film was deposited in 40 intermittent cycles. Substrate temperature was 175 °C and every 10 cycles the sample was sintered at 950 °C for 2 hours with a heating-cooling rate of 3 °C/min.



(a) EDS point-scan



(b) EDS line-scan

Figure 5.9: EDS analysis of 8YSZ thin film (5.5 μm thick.) deposited on porous cathode substrates of 5LSM-3YSZ after sintering at 950 °C. Chemical composition 84.36 at.% for Zr and 15.64 at.% for Y.

## 5.4 Spray deposition of nano-structured anode electrodes

In solid oxide fuel cells (SOFCs) a suitable anode provides an extended triple phase boundary (TPB) area where oxidation of the fuel occurs. These porous electrodes comprise either a composite of ionic and electronic conductors or a single phase of mixed ionic-electronic conducting electrode. In addition, structural requirements are the ionic and electronic pathways must be contiguous alongside with an interconnecting porosity to facilitate fuel transportation and electrical conductivity [102, 154]. Predominantly, Ni-YSZ cermet have been used as an anode electrode due to excellent catalytic properties of nickel for hydrogen oxidation and high electronic conductivity, combined with good ionic conductivity of YSZ [155]. However, long-term stability of Ni-YSZ anode is quite limited due to Ni-coarsening, carbon deposition and volume instability upon redox cycling [156].

In cathode-supported SOFCs the anode is relatively thin ( $<10\ \mu\text{m}$ ) and thus, less susceptible to redox cycling. Nevertheless, a fine microstructure with sub-micron particles should be targeted in order to preserve a high TPB density, reduced interfacial resistances and thus a good performance [37, 157–159].

Preparation of the anode electrode by conventional fabrication techniques such as screen printing require processing temperatures that usually greatly exceed  $1000\ ^\circ\text{C}$  to obtain adequate particle-to-particle contact and good adhesion to the electrolyte surface [157]. However, for cathode-supported SOFCs formation of zirconate phases (*e.g.* lanthanum zirconate) between the electrolyte and the cathode electrode degrade the SOFC performance and thus, prohibit the use of these methods. Therefore, alternative processing techniques can be used such as wet impregnation [160], reac-

tive sputtering [161], pulsed laser deposition [144] or spray pyrolysis [32,65,162]. To prepare the anode electrodes in order to complete the cathode-supported SOFCs in the present work, spray pyrolysis route was employed.

For the Ni-YSZ(40:60 vol.%) precursor solution nickel nitrate,  $\text{Ni}(\text{NO}_3)_2 \cdot 6\text{H}_2\text{O}$  was dissolved in deionized water with the addition of 8YSZ solution. The total ion concentration was 0.005 mol/l to produce small precipitate particles and thus to form a porous structure with adequate gas permeation. However, during testing the deposited Ni-YSZ anode was highly resistive ( $>200 \Omega \text{ cm}^2$ ). Figure 5.10 shows the morphology of the anode where the 8YSZ grown in columns with decorated nickel particles which did not form a continuous network that would enable uninterrupted electron conduction explaining the high resistance of the electrode. Although, synthesis of Ni-YSZ composite particles by spray pyrolysis have been reported [163,164], a direct film deposition by this method has not yet been demonstrated and thus needs further investigation.

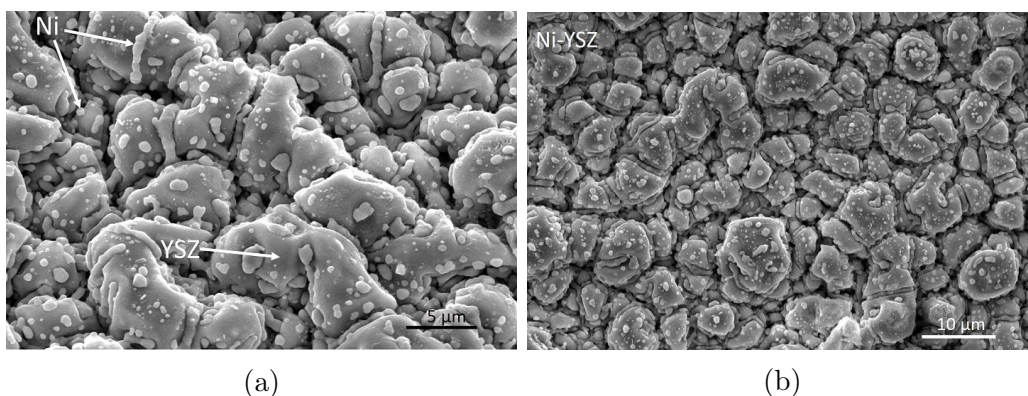


Figure 5.10: SEM micrographs in top view of Ni-YSZ anode prepared by spray pyrolysis after testing electrochemically in 5%  $\text{H}_2/\text{Ar}$ . Precursor concentration 0.005 mol/l, deposition time 270 min, 3 spray cycles, substrate temperature 210 °C, solution flow rate 0.6 ml/min, air flow rate 30 l/min, nozzle-to-substrate distance 25 cm, sintering at 750 °C for 2 hours.

Ceria-based anode electrodes exhibit mixed ionic and electronic conductivity due to reduction of  $\text{Ce}^{4+}$  to  $\text{Ce}^{3+}$  and are catalytic active to hydrocarbon fuel oxidation [165, 166]. This good catalytic activity of ceria ( $\text{CeO}_2$ ) arises from the ability to store and release oxygen vacancies associated with reversible phase transformations ( $\text{CeO}_{2-x}$ ) [167]. Moreover, the electronic conductivity as well as the catalytic activity of ceria can be significantly improved by the addition of transition metals such as Ni, Co, Pd or Ru forming a composite anode electrode [168–170].

Taking into account the above as an alternative anode material to Ni-YSZ, cobalt ceria ( $\text{Co}-\text{CeO}_2$ , 1:1 vol%) was selected. For the preparation of the precursor solution cobalt nitrate  $\text{Co}(\text{NO}_3)_2 \cdot 6\text{H}_2\text{O}$  and cerium nitrate  $\text{Ce}(\text{NO}_3)_3 \cdot 6\text{H}_2\text{O}$  were dissolved in deionized water. The total ion concentration was 0.005 mol/l. Spray deposition was performed in two intermittent cycles. Total deposition time was 180 min. At the end of each cycle the as-deposited film was sintered *in situ* at 540 °C for 1 hour. Afterwards, the sample was transferred to a muffle furnace where it was sintered at 750 °C for 2 hours with a heating-cooling rate of 3 °C/min. Figure 5.11 shows the morphology of the anode in top view before (fig. 5.11a,b) and after reduction (fig. 5.11c,d) in pure  $\text{H}_2$  during testing in a cathode-supported SOFC at 600 °C. The morphology belongs to a nano-porous interconnected network of  $\text{Co}-\text{CeO}_2$  decorated with cobalt nanoparticles. To determine the electrical conductivity of this anode and whether it is suitable for use in cathode-supported SOFCs, four-point DC conductivity measurements were performed up to 600 °C in 5% $\text{H}_2$ /Ar. For this experiment the cobalt ceria anode was prepared with the above process parameters deposited on a tape-cast 8YSZ substrate. The sample was placed in a tubular furnace and hydrogen was started to flow at 600 °C. In figure 5.12 4-point DC conductivity measurements are shown within a temperature range of 200 to

600 °C. The reduction of electronic conductivity as the temperature increased indicates that conduction occurs through the metallic phase of Co. At 600 °C a value of  $435 \text{ S cm}^{-1}$  was measured for the Co–CeO<sub>2</sub> that fulfils the requirement for an adequate electronic conductivity of a SOFC anode.

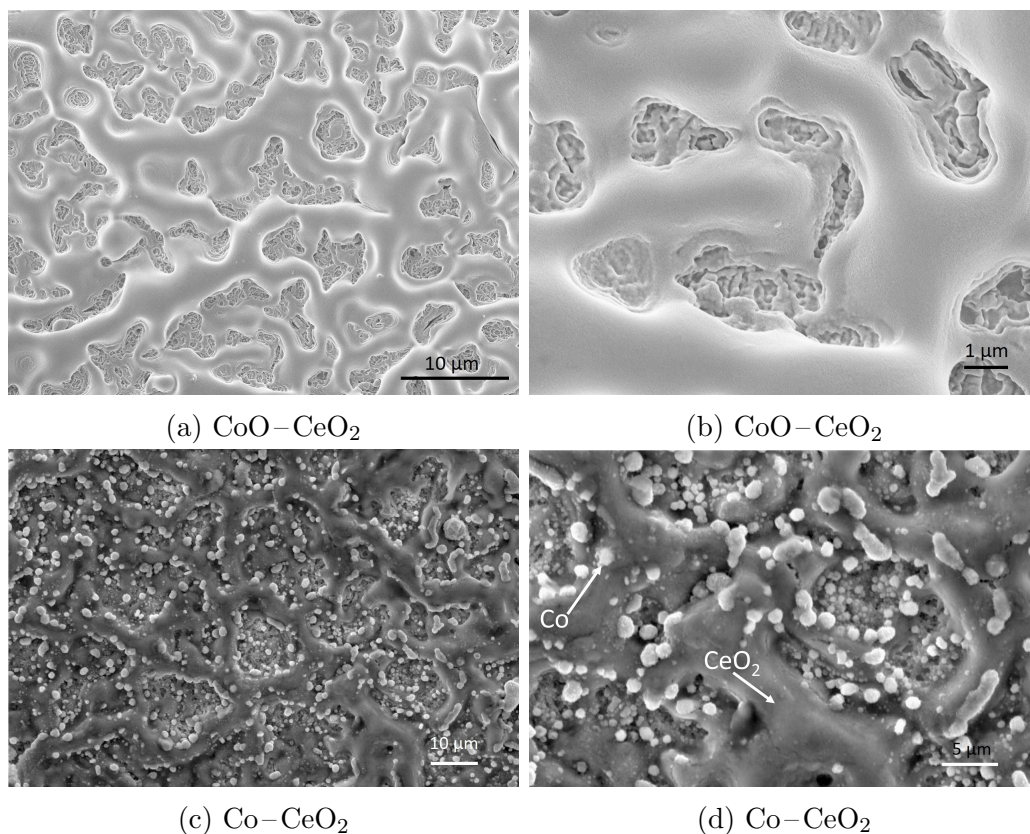


Figure 5.11: SEM micrographs in top view of nano-structured anode of Co–CeO<sub>2</sub> (1:1 vol.%) prepared by spray pyrolysis: a,b) oxidized and c,d) reduced after testing in H<sub>2</sub> at 600 °C. Precursor concentration 0.005 mol/l, total deposition time 180 min, 2 spray cycles, substrate temperature 170 °C, solution flow rate 0.6 ml/min, air flow rate 30 l/min, nozzle-to-substrate distance 25 cm, sintering at 750 °C for 2 hours.

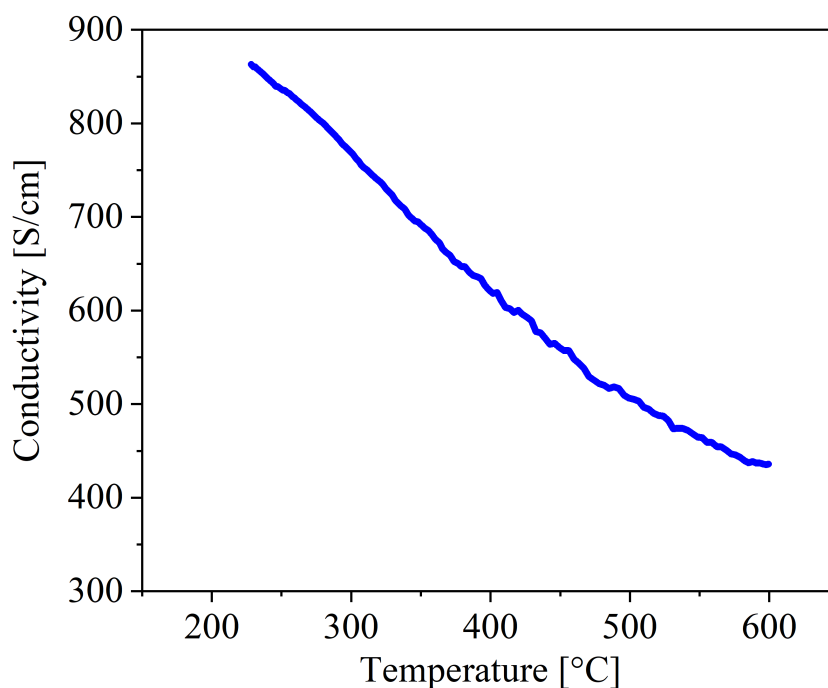


Figure 5.12: Four point conductivity of Co–CeO<sub>2</sub> in 5%H<sub>2</sub>/Ar ,deposited on tape cast 8YSZ by spray pyrolysis. Precursor concentration 0.005 mol/l, deposition time 180 min, 2 spray cycles, substrate temperature 170 °C solution flow rate 0.6 ml/min, air flow rate 30 l/min, nozzle-to-substrate distance 25 cm, sintered at 750 °C for 2 hours.

## 5.5 Conclusions

Cathode-supported SOFC components were successfully prepared by spray pyrolysis using pure aqueous solutions. Optimum process parameters for the spray deposition of these on cathode porous substrates of LSM-YSZ are given in table 5.3. The surface of the substrates was modified by spraying a cathode interlayer of LSM to provide a smooth substrate surface for the deposition of the electrolyte.

Dense and gas-tight thin films ( $\leq 5.5\mu\text{m}$ ) of 8YSZ electrolytes were deposited in spray cycles at substrate temperatures as low as 170 °C with a maximum depo-

sition rate of 16.5  $\mu\text{m}/\text{h}$ . The feasibility to obtain a dense microstructure of 8YSZ at sintering temperatures from 500  $^{\circ}\text{C}$  to 950  $^{\circ}\text{C}$  was also demonstrated. Intermit- tent spray deposition resulted in highly crystalline thin films of 8YSZ consisted of columnar single crystals grown perpendicular to the substrate with a preferential (111) orientation.

Nanostructured anode electrodes of cobalt ceria Co–CeO<sub>2</sub> (1:1 vol.%) were also prepared by spray pyrolysis. The anode electrode exhibited a high conductivity value of 435 S cm<sup>-1</sup> at 600  $^{\circ}\text{C}$  measured in 5% H<sub>2</sub>/Ar.

Table 5.3: Optimum spray pyrolysis process parameters for preparation of thin film cathode-supported SOFC components.

Thin films Experimental parameter	Interlayer La <sub>0.8</sub> Sr <sub>0.2</sub> MnO <sub>3</sub>	Electrolyte (Y <sub>2</sub> O <sub>3</sub> ) <sub>0.08</sub> (ZrO <sub>2</sub> ) <sub>0.92</sub>	Anode Co–CeO <sub>2</sub>	Units
Precursor concentration	0.025	0.1	0.005	mol/l
Nozzle to substrate distance	25	25	25	cm
Precursor flow rate	35	35	35	ml/h
Atomizing air flow rate	30	30	30	l/min
Substrate temperature	170	170-220	170	$^{\circ}\text{C}$
Deposition time/cycle	2	0.5	90	min
Annealing temperature/cycle	540	540	540	$^{\circ}\text{C}$
Annealing time/cycle	20	20	20	min
Sintering temperature	750-950	750-950	750	$^{\circ}\text{C}$
Sintering time	2	2	2	h

# Electrochemical performance of cathode-supported SOFCs

## 6.1 Introduction

Cathode-supported solid oxide fuel cells (SOFCs) in a tubular design emerged in the mid-1990s by Siemens/Westinghouse and have demonstrated the best durability in the development history of SOFCs [171]. The advantages of this type of SOFCs lie in the tubular geometry with the one-end closed, which doesn't require challenging gas sealants and enables the use of inexpensive transition metals such as Ni for cell-to-cell connections in reducing atmospheres [172]. Moreover, the electrolyte layer is better protected from cracking, in contrast with anode-supported SOFCs which are more susceptible to mechanical damage due to redox cycling [29].

There is a general consensus that minimizing the thickness of the electrolyte layer reduces significantly the ohmic losses in the cell and thus the SOFCs can operate sufficiently at lower temperatures [37]. However, it is often observed that despite the low ohmic contribution, the total resistance of the cell is considerably larger [9]. The main reason for this is the activation and concentration polarizations

of the electrodes and their interfaces with the electrolyte can often surpass the ohmic contribution especially for cathode-supported SOFCs at low temperatures [16,22].

Another major challenge is to obtain a dense and gas-tight electrolyte at low sintering temperatures  $< 1000\text{ }^{\circ}\text{C}$  in order to avoid the formation of insulating pyrochlore phases ( $\text{La}_2\text{Zr}_2\text{O}_7$ ,  $\text{SrZrO}_3$ ) at the cathode interface with the electrolyte [98]. Existing processing techniques that give a solution to this problem (*e.g.* EVD, RF-sputtering) require expensive and complex equipment involving vacuum or electrical charge increasing the cost for industrial applications [15]. On the other hand, spray pyrolysis is a coating technique that offers a cost-effective solution and already has been used for preparation of thin electrolytes in SOFCs [14, 25, 26]. However, optimization of many process parameters combined with the requirement to obtain a gas-tight electrolyte over porous bulk ceramics and sealing challenges explains why literature reports on SOFCs testing are limited.

In the present study, electrochemical results of cathode-supported SOFCs are reported. The fuel cells consists of thin film of electrolytes and anode electrodes prepared by spray pyrolysis, operated within a temperature range of  $600\text{--}850\text{ }^{\circ}\text{C}$ . The influence of the cathode support porosity and the ageing behaviour of the anode electrode on the performance of the cells are discussed.

## 6.2 Electrical measurements

Cathode-supported SOFCs containing thin films of LSM interlayers, 8YSZ electrolytes and  $\text{Co-CeO}_2(1:1\text{ vol.}\%)$  anodes were prepared by spray pyrolysis technique. For the deposition of the thin film SOFC components cathode substrates of 5LSM-3YSZ (9:1 wt.%) and 5LSM-8YSZ (1:1 wt.%) were used. The substrates were

prepared as described in detail previously (section 2.2). For the 5LSM-8YSZ substrates the porosity was reduced to 23% to improve the mechanical strength of the substrates and also 8YSZ was used at a higher percentage to improve the ionic conductivity of the composite cathode. The 5LSM-3YSZ substrates were more porous with a 42% porosity and less mechanically strong than the 5LSM-8YSZ substrates. Spray pyrolysis process parameters for the preparation of the cathode-supported SOFCs components are given in table 6.1.

For the electrochemical measurements of the cathode-supported SOFCs the experimental apparatus shown in figure 2.10 was used. Figure 6.1a shows the structure in cross section of a cathode-supported SOFC ( $\text{Co-CeO}_2/8\text{YSZ}/\text{LSM}/(\text{LSM-3YSZ})_{\text{substrate}}$ ) with a thin YSZ electrolyte of 3.2-3.5  $\mu\text{m}$  after operating the cell in 5% $\text{H}_2/\text{Ar}$  for five consecutive days. The electrolyte exhibited a dense microstructure with a homogeneous thickness. Minor defects which are seen are probably formed during the extraction and breakage of the fuel cell for SEM examination. The sprayed LSM interlayer reduced the porosity of the substrate and thus the thickness deviation of the 8YSZ electrolyte was negligible. The  $\text{Co-CeO}_2$  anode shown in fig.6.1b has a nanostructured porosity obtained after a reduction of  $\text{CoO}$  particles to metallic  $\text{Co}$ . Interestingly, the  $\text{CeO}_2$  particles seem to have retained their structure in contrast with the metal particles of  $\text{Co}$  which were agglomerated forming larger size particles.

Figure 6.2 shows I-V-P curves at various temperatures of the fuel cell shown in fig.6.1. Initially, the cell was heated up to 860  $^\circ\text{C}$  to soften the pyrex glass rings and seal the fuel cell. Afterwards, it was cooled down prior the electrochemical testing of the cell within a temperature range from 700  $^\circ\text{C}$  to 850  $^\circ\text{C}$ . As a fuel hydrogen (5% $\text{H}_2$  diluted in argon) was supplied to the anode electrode at a flow rate of 15 mL/min.

Table 6.1: Spray pyrolysis process parameters for deposition of thin film cathode-supported SOFC components.

	Fuel cell no.A1				Fuel cell no.A2				Fuel cell no.A3		
Cathode substrates	5LSM-3YSZ (por. 42%)				5LSM-3YSZ (por. 42%)				5LSM-8YSZ (por. 23%)		
Thin films	Co-CeO <sub>2</sub>		8YSZ		Co-CeO <sub>2</sub>		8YSZ		Co-CeO <sub>2</sub>		8YSZ
Precursor concentration, [mol/l]	0.005	0.1	0.025	0.025	0.005	0.1	0.025	0.025	0.005	0.1/0.05	
Nozzle to substrate distance, [cm]	25	25	25	25	25	25	25	25	25	25	
Precursor flow rate, [ml/h]	35	35	35	35	35	35	35	35	35	35	
Atomizing air flow rate, [l/min]	30	30	30	30	30	30	30	30	30	30	
Substrate temperature, [°C]	170	170	170	170	170	170	170	170	210	210	
Deposition time/cycle, [min]	90	0.5	2	2	90	0.5	2	2	90	0.5/2	
Total deposition time, [min]	180	19.5	14	14	180	23.5	10	10	180	11.5+10	
Annealing temperature/cycle, [°C]	540	540	540	540	540	540	540	540	540	540	
Annealing time/cycle, [min]	60	20	20	20	60	20	20	20	60	20	
Sintering temperature, [°C]	750	900	900	900	750	750	750	750	850	900	
Sintering time, [h]	2	2	2	2	2	2	2	2	2	2	

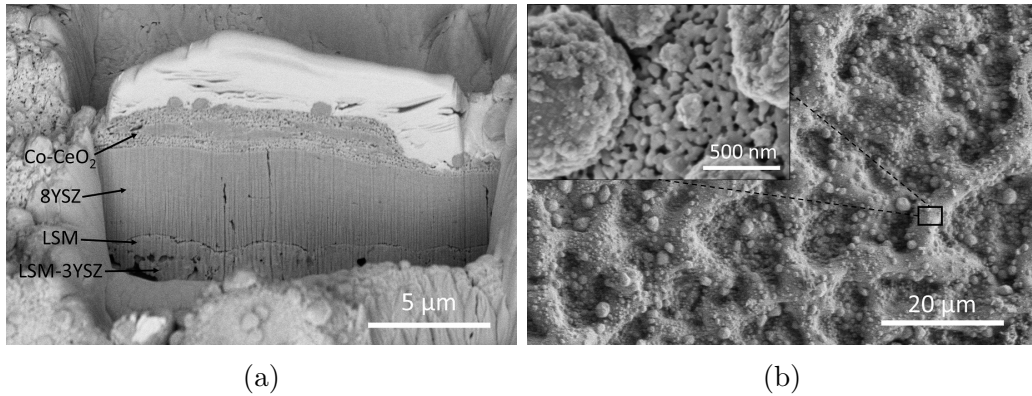


Figure 6.1: SEM micrographs in cross section and top view of cathode-supported SOFC(no.A1) with a  $3.5\ \mu\text{m}$  thick 8YSZ electrolyte and Co–CeO<sub>2</sub> anode after testing in 5%H<sub>2</sub> for  $\approx 100\text{h}$ .

To the cathode air was supplied at a flow rate of 90 ml/min. The active electrode area was  $0.385\ \text{cm}^2$ . It should be noted that due to the curing requirement of the sealant the deposited thin electrolytes were sintered at a higher temperature of  $900\ ^\circ\text{C}$  to stabilize their structure. During the first day of operation, a maximum power density of  $127\ \text{mW cm}^{-2}$  was achieved at 0.5 V and operating temperature of  $850\ ^\circ\text{C}$ . The OCV of the cathode-supported SOFC exhibited values close to the theoretical ones calculated using the Nernst equation, indicating a gas-tight electrolyte. However, the small deviation of the OCV shown in table 6.2 is attributed mostly to sealant failure as at lower operating temperatures (*e.g.*  $700\ ^\circ\text{C}$ ) the OCV was decreased. After nearly 100 hours of operation the peak power performance of the cell was  $\approx 35\%$  degraded as can be seen in figure 6.2b. The maximum power output was reduced to  $83\ \text{mW cm}^{-2}$  at  $850\ ^\circ\text{C}$ . The degradation of the fuel cell is mostly attributed to severe agglomeration of the metallic Co in the anode electrode as shown in figure 6.3, which resulted in a significant reduction of the catalytic active surface area of the electrode. A similar degradation mechanism has

been reported by Jung *et al.* [173] for copper ceria (Cu–CeO<sub>2</sub>) anode electrodes where the metallic copper particles agglomerated after exposure in pure hydrogen at 800 °C. In general, the mobility and segregation of Cu is mainly attributed to the relative melting temperature of Cu (1083 °C) [166,174]. On the other hand, cobalt exhibits much higher melting temperature (1495 °C) and has been used as a second metal to improve the thermal stability of anode electrodes [175]. However the results shown in fig.6.3,6.10 presumably indicate the mobility and agglomeration of cobalt are electrochemically driven.

Table 6.2: Long-term performance of cathode-supported SOFC(no.A1).

Operating temperature [°C]	OCV [V]	Power density [mW cm <sup>-2</sup> ]	Rs [Ω cm <sup>2</sup> ]	Rp [Ω cm <sup>2</sup> ]	
850	0.93	127	0.36	1.62	
790	0.88	71	0.41	2.65	1 <sup>st</sup> Day
763	0.93	56	0.44	4.01	
700	0.84	26	0.56	5.54	
850 <sup>1</sup>	1.00	88	0.43	2.55	
850	0.97	83	0.46	2.85	5 <sup>th</sup> Day
800	0.97	56	0.53	4.61	
750	0.94	33	0.68	7.18	
700	0.89	16	0.96	14.13	

<sup>1</sup> Power density and OCV data recorded on the 4<sup>th</sup> day of operation.

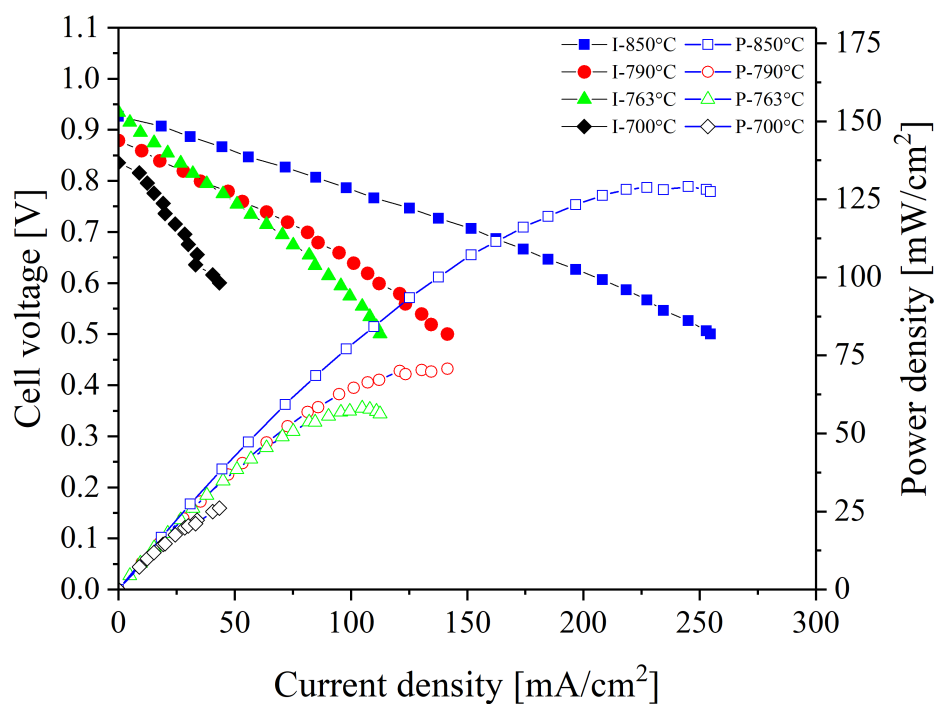
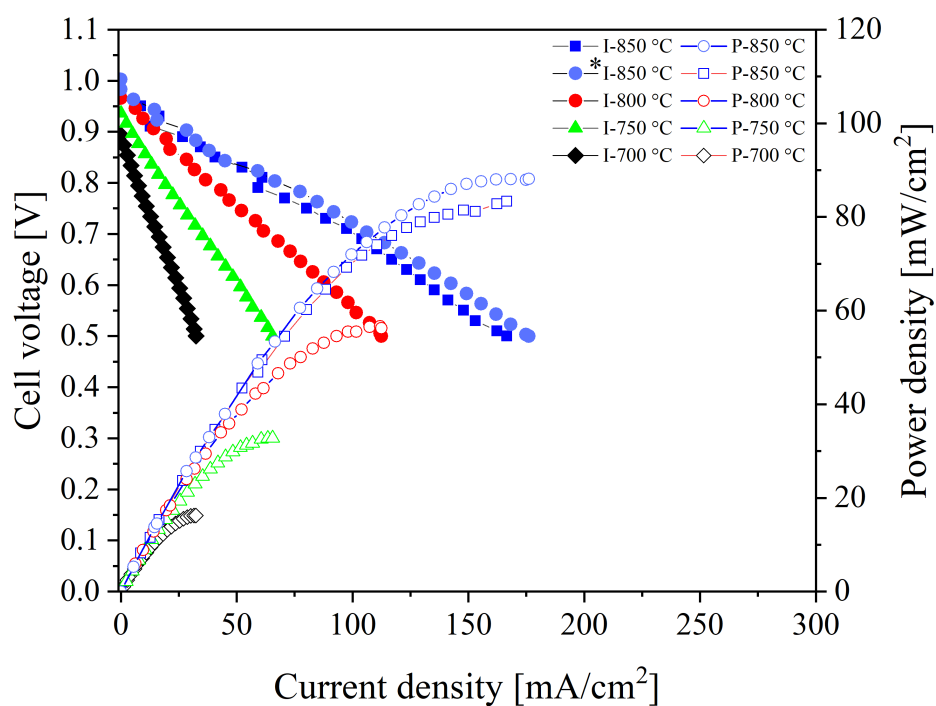
(a) 1<sup>st</sup> Day(b) 5<sup>th</sup>Day

Figure 6.2: Long-term performance of cathode-supported SOFC(no.A1) under 5% $\text{H}_2/\text{Ar}$  at various temperatures for 5 days. (\* I-V curve obtained during the 4<sup>th</sup> day of operation).

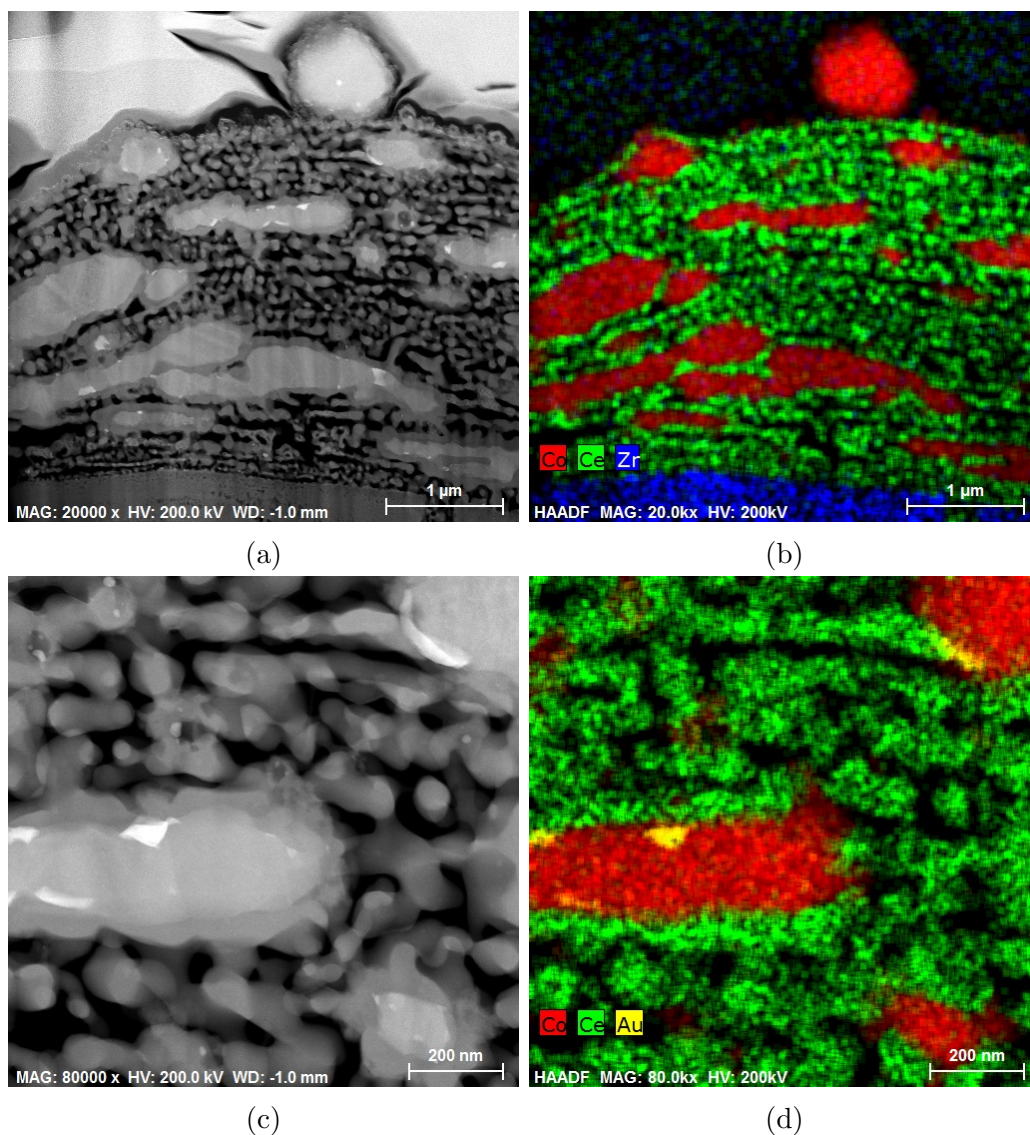


Figure 6.3: TEM and EDS analysis of the Co-CeO<sub>2</sub> anode electrode (fuel cell no.A1) after testing in 5%H<sub>2</sub>/Ar within a temperature range of 700-850 °C for 5 days. (a,c) TEM micrographs of the analysed area, (b,d) EDS mapping of cobalt, cerium, zirconium and gold. Gold paste used as a current collector explaining the presence of Au particles.

Figure 6.4 shows impedance spectra of the cathode-supported SOFC (no.A1) measured under the same operating conditions and temperatures for I-V curves. The high frequency impedance intercept gives the total ohmic resistance ( $R_s$ ) of the cathode-supported SOFC while the low frequency intercept gives the total polarisation resistance of the electrodes ( $R_p$ ). After five days of operation only a small increase of the ohmic resistance is observed compared to a dramatic increase of the  $R_p$ , especially at lower temperatures (see table 6.2). Since the sintering temperature of the electrolyte was well below  $1000\text{ }^\circ\text{C}$  and the operating temperature of the cell, the formation of zirconate phases at the interface of the cathode and the electrolyte that would contribute to the increase of the  $R_s$  is excluded. Taking into consideration the LSM is very stable in air for long term periods the increase of the  $R_p$  is attributed to the reduction of the catalytic active area of the Co–CeO<sub>2</sub> anode resulting in performance degradation of the cell. In general, the ohmic losses of a SOFC are mostly dominated by the electrolyte membrane since this component exhibits the highest resistance in the cell. However, for electrode supported SOFCs where the electrolytes are very thin ( $< 10\text{ }\mu\text{m}$ ) the ohmic losses are significantly minimised. This is reasonable since the area specific resistivity (ASR) of a  $3.5\text{ }\mu\text{m}$  thick YSZ film at  $800\text{ }^\circ\text{C}$  should be only  $0.018\text{ }\Omega\text{ cm}^2$ . The measured  $R_s$  values of the cathode-supported SOFC although they are relative small  $< 1\text{ }\Omega$  are exceeding the ASR for the thin YSZ electrolyte of the measured cell. Therefore, this is attributed mainly to the cathode support which is the thickest(1mm) component of the cell combined with wire losses.

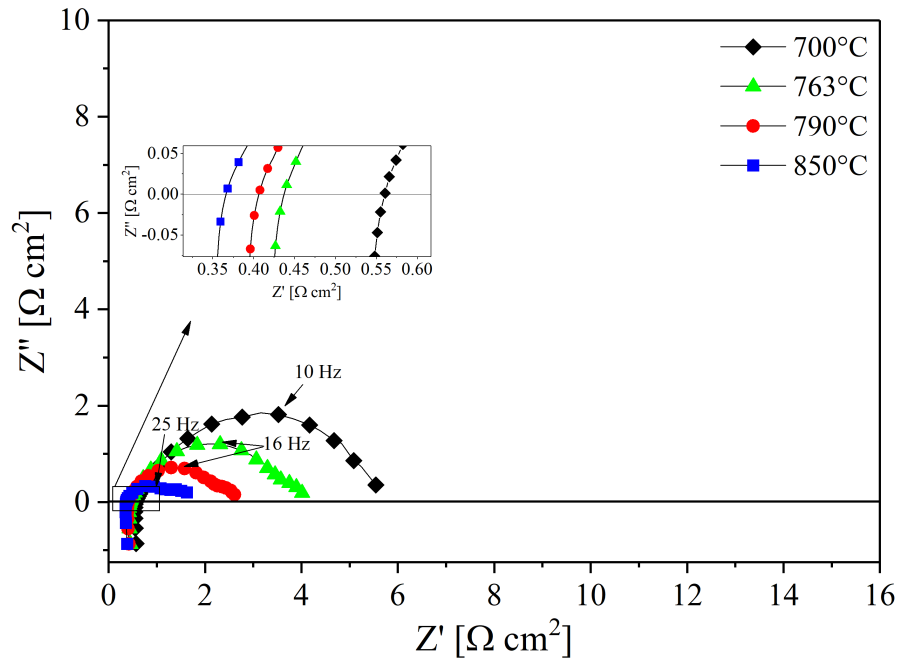
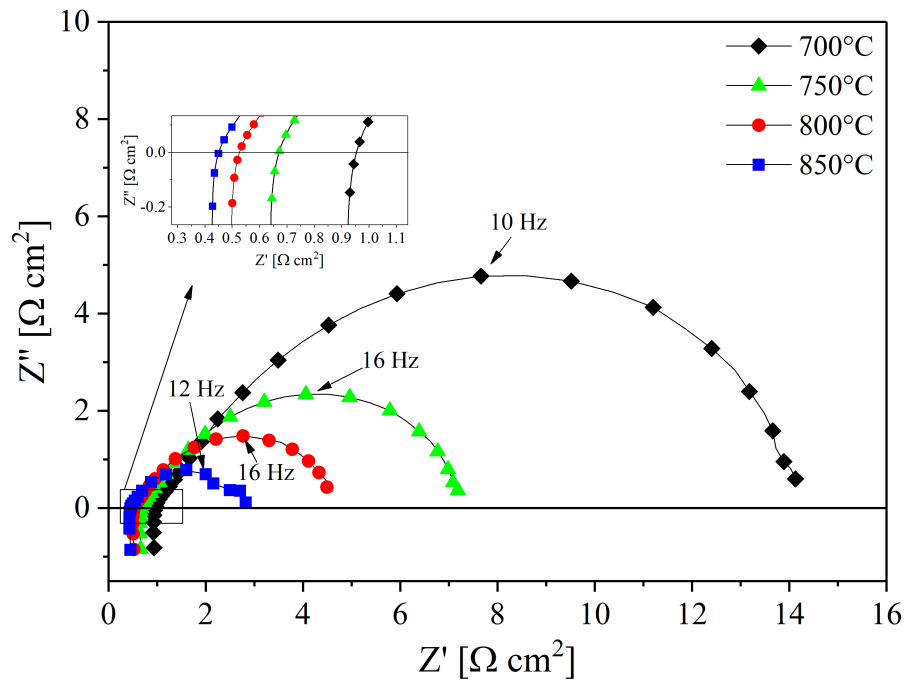
(a) 1<sup>st</sup> Day(b) 5<sup>th</sup> Day

Figure 6.4: Impedance spectra of cathode-supported SOFC(no.A1) obtained at OCV within a temperature range of 700-850 °C for a) 1 day and b) after 5 days.

Figure 6.5 exhibits the total ohmic resistances of the cathode-supported SOFC (no.A1) obtained at OCV (fig. 6.4) as a function of the reciprocal temperature. The resistance values show an Arrhenius temperature dependence and from the linear fits an activation energy of 0.15 eV was obtained which is very close to the 0.11 eV measured for the 5LSM-3YSZ cathode support. This shows that the performance of the cell is limited by the cathode and its interface with the electrolyte [16]. However, the increase of the activation energy to 0.24 eV after  $\approx 100$  hours of operation is presumably caused from the degradation of the Co–CeO<sub>2</sub> electrode (fig.6.3).

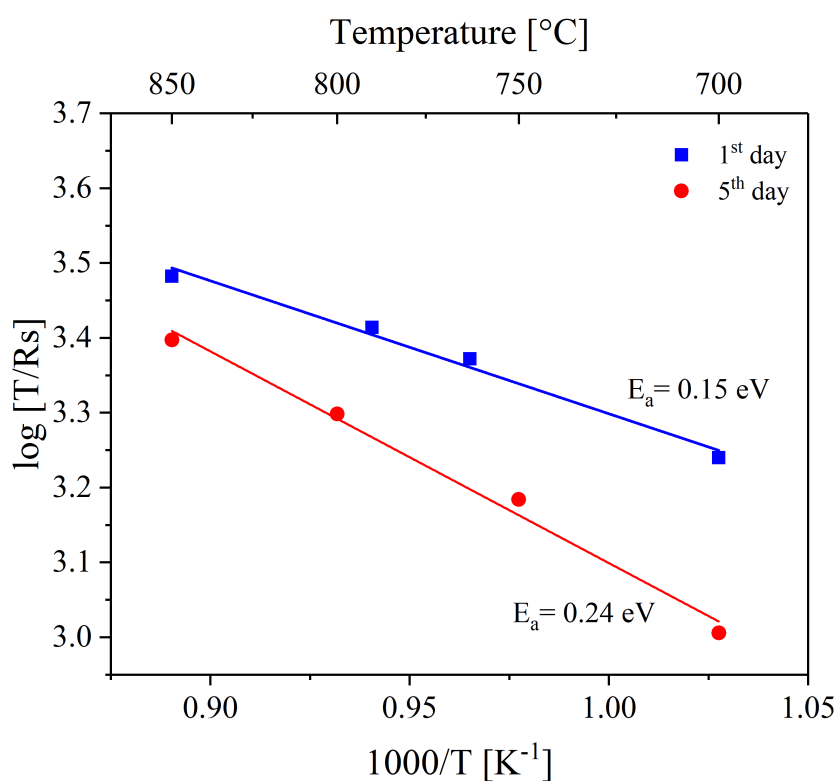


Figure 6.5: Arrhenius plot of the inverse ohmic resistance for a cathode-supported SOFC (no.A1) over a range of operating temperatures in 5% $H_2$ /Ar.

Figure 6.6 illustrates the microstructure of a cathode-supported SOFC(no.A2) in cross section after testing in pure  $H_2$ . The thickness of the spray deposited YSZ film was approximately  $4\ \mu\text{m}$ . The 8YSZ electrolyte was gas-tight and adhered well to the cathode support. As can be seen the gold paste was not very well attached to the  $\text{Co-CeO}_2$  which also might contribute to the total ohmic resistance ( $R_s$ ) of the cell.

For this experiment the fuel cell was sealed using an alumina-based cement (Ceramabond 552) instead of pyrex glass rings. The anode was supplied with pure  $H_2$  while the cathode was exposed to static air. Figure 6.7 presents the electrochemical performance of the fuel cell(no.A2) in I-V curves and impedance spectra. The thermal expansion coefficient (TEC) mismatch between the sealant ( $7.7 \times 10^{-6}\ \text{K}^{-1}$ ) and the cathode support ( $12.0 \times 10^{-6}\ \text{K}^{-1}$ ) of the cell resulted in cracking of the cell explaining the low OCV value shown in figure 6.7a. However, the performance of the cell is quite remarkable at  $600\ ^\circ\text{C}$  considering the fact that the cell was leaking. Impedance spectra data were obtained at OCV. Model fitting with the equivalent circuit shown in fig. 6.7b was employed to fit the curves and calculate the  $R_s$  and  $R_p$  of the cell (see table 6.3). The total polarization resistance ( $R_p$ ) of the electrodes at  $600\ ^\circ\text{C}$  was  $1.06\ \Omega\ \text{cm}^2$ . This value is low taking into account the reported polarization resistance of the conventional LSM-YSZ cathode at this temperature is  $11.37\ \Omega\ \text{cm}^2$  [97]. This improvement possibly can be explained due to the addition of the cathode interlayer that increased the interface area accelerating the charge-transfer reactions at the interface [96, 148].

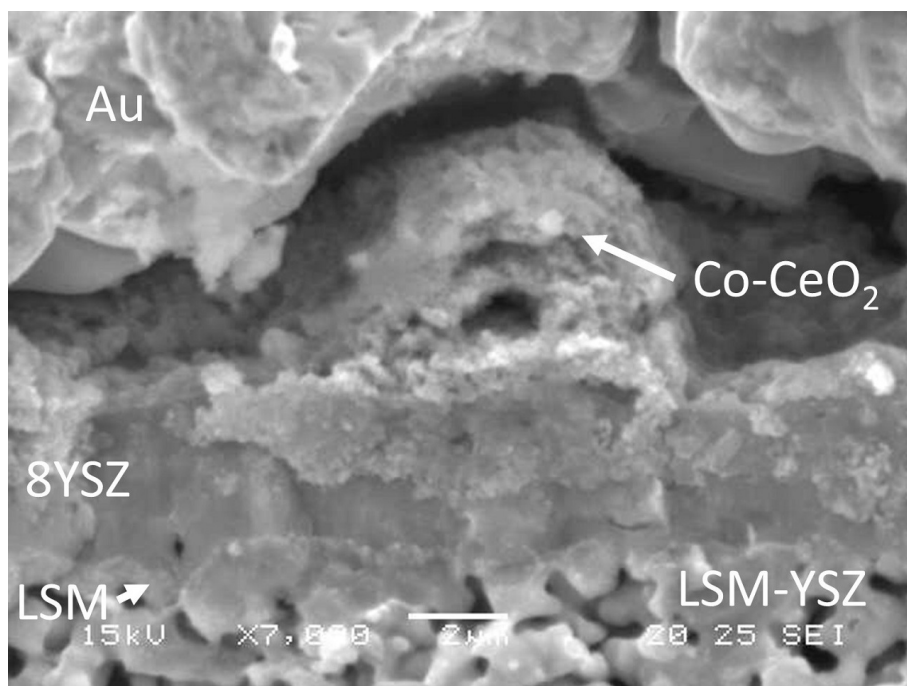


Figure 6.6: SEM micrograph in cross section of a cathode-supported SOFC (no.A2) after testing in pure  $H_2$  at  $600\text{ }^\circ\text{C}$ .

Table 6.3: Total polarization ( $R_p$ ) and ohmic ( $R_s$ ) resistances of cathode-supported SOFC(no.A2) obtained at OCV.

Operating temperature [ $^\circ\text{C}$ ]	$R_s$ [ $\Omega\text{ cm}^2$ ]	$R_p$ [ $\Omega\text{ cm}^2$ ]
600	0.45	1.06
550	0.77	1.27

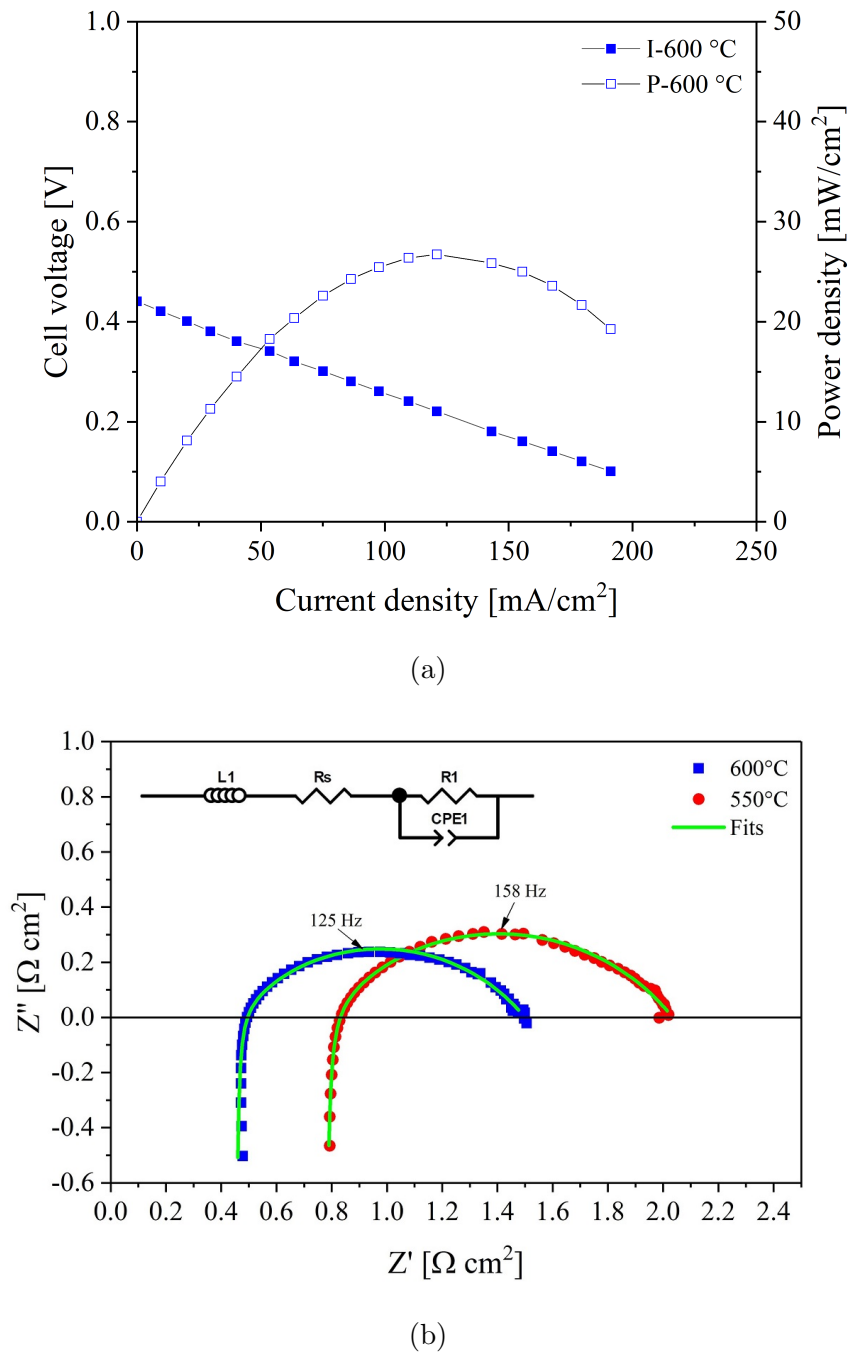


Figure 6.7: Electrochemical performance of cathode-supported SOFC(no.A2) in pure H<sub>2</sub> a) Voltage and power density vs current density and b) Impedance spectra obtained at open circuit voltage.

Figure 6.8 shows a SEM micrograph in cross-section of a fractured cathode-supported solid oxide fuel cell(no.A3). For this cell a LSM-8YSZ(1:1 wt.%) cathode support was used with a porosity of 23% in order to improve the mechanical robustness of the fuel cell. The 8YSZ film prepared by spray pyrolysis was gas-tight and had a thickness of  $3.8\ \mu\text{m}$ . The cell was operated at intermediate temperatures for five days in  $5\%\text{H}_2/\text{Ar}$ .

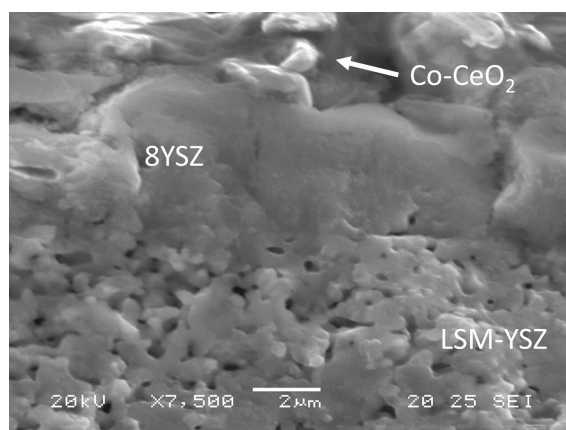
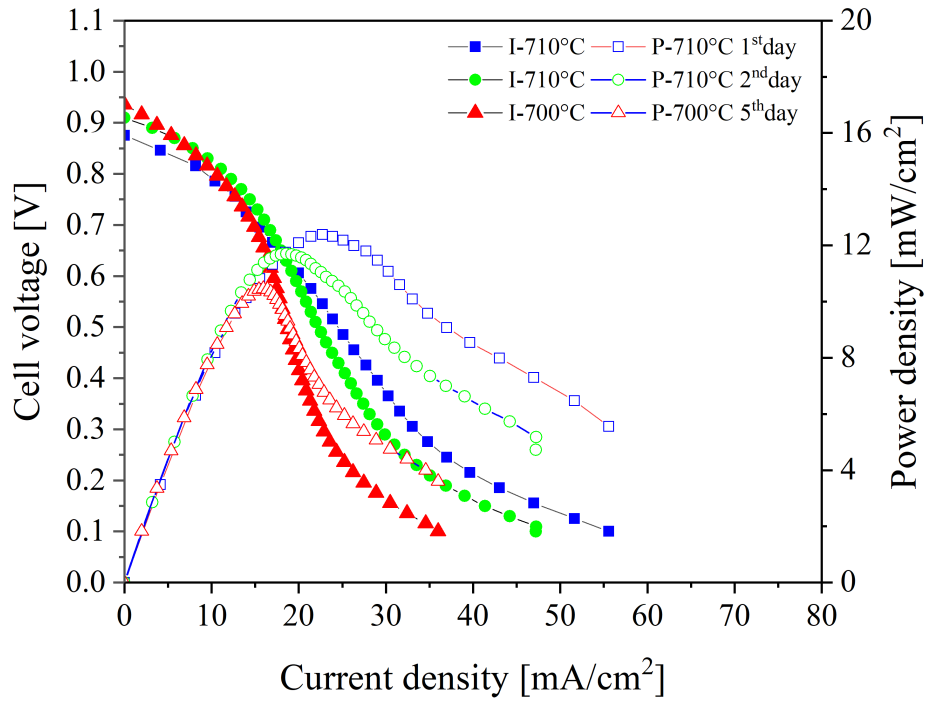
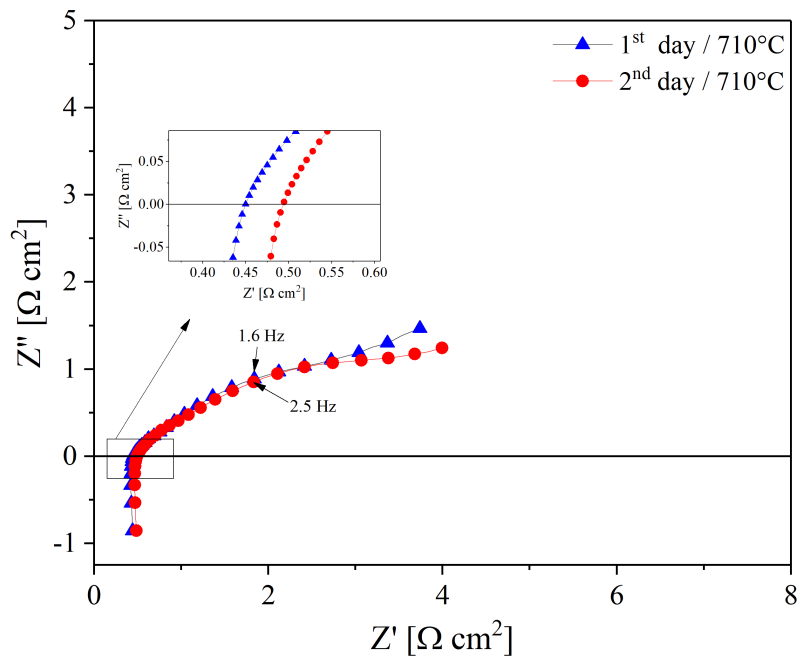


Figure 6.8: SEM micrograph in cross section of a cathode-supported SOFC (no.A3) with a  $3.8\ \mu\text{m}$  8YSZ electrolyte after testing in  $5\%\text{H}_2/\text{Ar}$  at various temperatures for 5 consecutive days.

Figure 6.9 shows the I-V-P characteristic curves for the cathode-supported SOFC (no.A3) obtained during the first and second day of operation and after five days. The cell initially exhibited a maximum power density of  $12\ \text{mW cm}^{-2}$  at  $710\ ^\circ\text{C}$ . Poor performance of the cell can be explained by the low porosity of the cathode support and the large thickness ( $\approx 1\text{mm}$ ) which resulted in severe mass transport limitation. This is evident from the slope of the I-V curves(fig.6.9a) and the impedance spectra (fig.6.9b). In addition, gradual performance degradation (*i.e.*20%) of the cell was also observed for this cell due to heavy agglomeration of the cobalt particles shown in figure 6.10.



(a)



(b)

Figure 6.9: Long-term performance of cathode-supported SOFC(no.A3) in 5% $H_2$ /Ar  
 a) I-V and I-P curves and b) Impedance spectra obtained at open circuit voltage

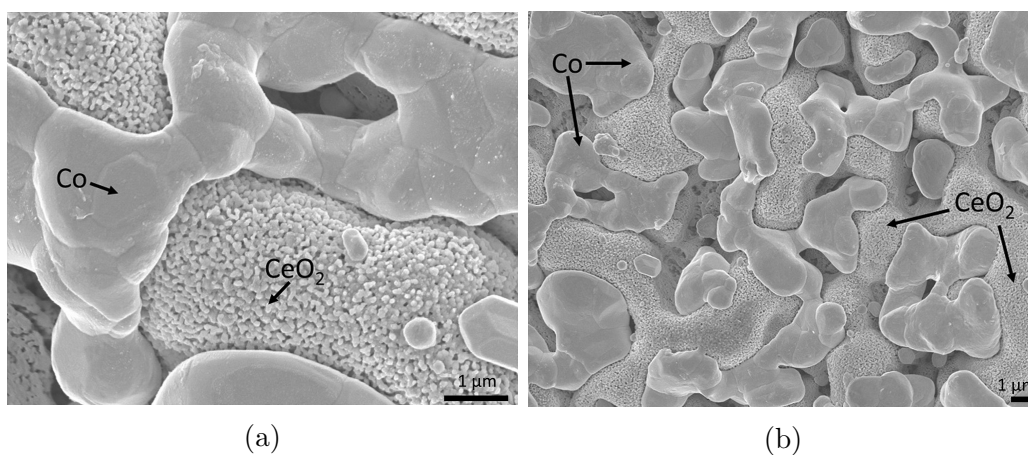


Figure 6.10: SEM micrographs in top view of Co–CeO<sub>2</sub> (fuel cell no.A3) after testing in 5% $\text{H}_2$ /Ar at intermediate operating temperatures for 5 days.

Figure 6.11 demonstrates the stability of the open circuit voltage of the cathode supported SOFC (no.A3) as a function of time at 700 °C. The value of the OCV was quite stable and a maximum value of 0.93V was obtained.

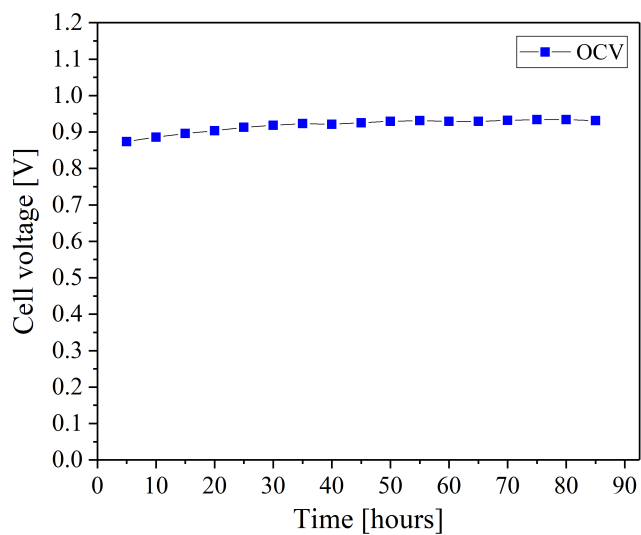


Figure 6.11: Open circuit voltage (OCV) of cathode-supported SOFC(no.A3) as a function of time at 700 °C in 5% $\text{H}_2$ /Ar.

## 6.3 Conclusions

In this chapter electrochemical performance of cathode-supported SOFCs with thin (3.5-4  $\mu\text{m}$ ) electrolytes prepared by spray pyrolysis technique was presented. Dense and defect-free 8YSZ electrolyte films were prepared on porous cathode supports of LSM-YSZ using aqueous solutions at sintering temperatures  $< 1000^\circ\text{C}$ . The gas-tightness of the electrolyte films was demonstrated by the measured high open circuit voltage (OCV) (table 6.4) that was close to the theoretical value for the fuel cells sealed with pyrex glass rings.

Alumina-based sealing materials (Ceramabond 552) which exhibit a significant different thermal expansion coefficient than the cathode support were found to be unsuitable for use with the cathode-supported SOFCs.

The best performance of the cathode-supported SOFCs was demonstrated using 5% $\text{H}_2/\text{Ar}$  as fuel. The OCV value was slightly reduced at lower operating temperatures (*e.g.* 0.84 V at  $700^\circ\text{C}$ ) indicating pyrex glass, in the current setup, did not completely seal the cell. As a result the supply of pure hydrogen formed a flame, caused by mixing of the hydrogen and oxygen at high operating temperature (*i.e.*  $850^\circ\text{C}$ ), melting the silver wires used for current collection.

A maximum power density of  $127\text{ mW cm}^{-2}$  was attained at operating temperature of  $850^\circ\text{C}$ . However, heavy agglomeration of the Co-CeO<sub>2</sub> anode resulted in severe performance degradation of the cells after long-term operation. Optimum cathode support porosity was 42%, as decreasing the porosity to 23% resulted in mass transport limitation of air, resulting in poor cell performance.

In conclusion, spray pyrolysis successfully was used to prepare thin film electrolytes for application in cathode-supported SOFCs.

Table 6.4: Summary of the cathode-supported SOFCs performance

Solid oxide fuel cells	no.A1	no.A2	no.A3
Cathode support	5LSM-3YSZ (9:1 wt.%)	5LSM-3YSZ (9:1 wt.%)	5LSM-8YSZ (1:1 wt.%)
Cathode support porosity [%]	42	42	23
Cathode interlayer	LSM	LSM	-
Electrolyte thickness [ $\mu\text{m}$ ]	3.5	4.0	3.8
Anode	Co-CeO <sub>2</sub>	Co-CeO <sub>2</sub>	Co-CeO <sub>2</sub>
Fuel	5%H <sub>2</sub> /Ar	H <sub>2</sub>	5%H <sub>2</sub> /Ar
Operating temperature [ $^{\circ}\text{C}$ ]	850	600	700
OCV [V]	1.002	0.441 <sup>1</sup>	0.931
Max. power density at 0.5V [mW/cm <sup>2</sup> ]	127	26 (at 0.2 V)	12
Max. current density [mA/cm <sup>2</sup> ]	255	121	24
Rs [ $\Omega\text{ cm}^2$ ]	0.36	0.45	0.45

<sup>1</sup> fuel cell sealed with ceramabond 552.



## General Conclusions

Spray pyrolysis technique was successfully optimized to deposit thin electrolytes and porous electrodes for cathode-supported solid oxide fuel cells. Composite cathodes of 5LSM-3YSZ with a uniform porosity of 42% and adequate mechanical strength were used as substrates for coating thin film SOFC components. The microstructure of the substrates had to be optimized by a series of processing steps (*i.e.* particles coarsening, ball milling, sieving etc.) due to excessive particle growth and shrinkage of the 5LSM that initially led to formation of large agglomerates, reducing the gas permeability of the support. The top surface of the substrates was modified by spraying a LSM cathode interlayer to provide a smooth less porous surface prior the deposition of the YSZ electrolyte.

A parametric study of the process parameters was carried out using pure aqueous solutions and revealed precursor concentration in conjunction with deposition time as the most critical parameters to obtain either a gas-tight electrolyte or a nano-porous anode electrode. To obtain a dense film microstructure the solution concentration should be as high as possible (*e.g.* 0.1 mol l<sup>-1</sup>) with a very short deposition time per cycle. In contrast, for nano-porous film structures, low solution

concentrations (*e.g.* 0.005 mol l<sup>-1</sup>) are preferable accompanied by longer deposition time per cycle.

Intermittent spray deposition is the key strategy to obtain preferential (111) oriented thin films of YSZ employing concentrated precursor solutions and thus, improving the deposition rate of the film. Columnar structures of thin YSZ films with a uniform thickness obtained at deposition temperatures as low as 170 °C with high deposition rates (*i.e.*  $\geq 10$   $\mu\text{m}/\text{h}$ ). To suppress the formation of insulating zirconate phases at the interface between the YSZ electrolyte and the LSM relative low sintering temperatures of 750 °C to 950 °C were applied. This was confirmed by XRD and TEM analysis where no indication of such a phase was found.

Cathode-supported SOFCs with thin YSZ electrolytes (*i.e.* 3.5-4  $\mu\text{m}$ ) and cobalt ceria Co-CeO<sub>2</sub> anode electrodes were electrochemically tested. Sealant materials should exhibit a thermal expansion coefficient (TEC) close to the substrate material, especially for cathode-support SOFCs.

The gas-tightness of the YSZ films was demonstrated by the open circuit voltage (OCV) that was close to the theoretical value. At 850 °C an OCV of 1.002 V was measured at the 4<sup>th</sup> day of operation under 5% H<sub>2</sub>/Ar. However, the power output was degraded 35% after  $\approx 100$  h of operation due to heavy agglomeration of cobalt metal observed in the anode electrode. The maximum power density was 127 mW cm<sup>2</sup> at 850 °C at the 1<sup>st</sup> day of operation. From Arrhenius plot of total ohmic resistance of the cell (*i.e.*  $\log[T/R_s]$  vs  $1000/T$ ), an activation energy of 0.15 eV was calculated, which was very close to the measured value for the cathode support, indicating the performance was limited mostly by the cathode support.

Spray pyrolysis has been successfully applied for preparation both of thin SOFC electrolytes and electrodes at considerable low sintering temperatures, reducing the

fabrication cost of cathode-supported SOFCs. One possible solution to improve the sealing of planar-SOFCs would be the use of zirconia-based ceramic tubes instead of alumina tubes with zirconia-based sealants. Moreover, to avoid particle agglomeration in the spray deposited anode, either the use of alloy metals (*e.g.* CoNi) or perovskites such as  $\text{La}_{0.75}\text{Sr}_{0.25}\text{Cr}_{0.5}\text{Mn}_{0.5}\text{O}_3$  (LSCM), with a more stable structure, would be suitable. In addition, it is highly recommended the process to be automated and controlled by a suitable PC software for intermittent spray deposition. This will significantly increase productivity and also minimize the human error. The advantage of spray pyrolysis to deposit thin films on non-planar substrates for preparation of cathode-supported SOFCs of tubular design should be the next target as sealing in planar geometries proved to be a major problem.



# References

- [1] J. I. Chowdhury, Y. Hu, I. Haltas, N. Balta-Ozkan, G. Matthew, and L. Varga, “Reducing industrial energy demand in the UK: A review of energy efficiency technologies and energy saving potential in selected sectors,” *Renewable and Sustainable Energy Reviews*, vol. 94, no. July, pp. 1153–1178, 2018.
- [2] N. Bizon and P. Thounthong, “Fuel economy using the global optimization of the Fuel Cell Hybrid Power Systems,” *Energy Conversion and Management*, vol. 173, no. July, pp. 665–678, 2018.
- [3] S. P. S. Badwal and K. Foger, “Solid Oxide Electrolyte Fuel Cell Review,” *Ceramics International*, vol. 22, pp. 257–265, 1996.
- [4] W. Grove, “Xxiv. on voltaic series and the combination of gases by platinum,” *The London, Edinburgh, and Dublin Philosophical Magazine and Journal of Science*, vol. 14, no. 86-87, pp. 127–130, 1839.
- [5] E. D. Wachsman, C. A. Marlowe, and K. T. Lee, “Role of solid oxide fuel cells in a balanced energy strategy,” *Energy and Environmental Science*, vol. 5, no. 2, pp. 5498–5509, 2012.
- [6] A. Tesfai and J. Irvine, “4.10 - solid oxide fuel cells: Theory and materials,” in *Comprehensive Renewable Energy* (A. Sayigh, ed.), pp. 261 – 276, Oxford: Elsevier, 2012.
- [7] N. Q. Minh and T. Takahashi, “Chapter 2 - principles of operation,” in *Science and Technology of Ceramic Fuel Cells* (N. Q. Minh and T. Takahashi, eds.), pp. 15 – 40, Oxford: Elsevier Science Ltd, 1995.
- [8] S. McIntosh and R. J. Gorte, “Direct Hydrocarbon Solid Oxide Fuel Cells,” *Chemical Reviews*, vol. 104, pp. 4845–4866, Oct 2004.

- [9] A. V. Virkar, J. Chen, C. W. Tanner, and J. W. Kim, "The role of electrode microstructure on activation and concentration polarizations in solid oxide fuel cells," *Solid State Ionics*, vol. 131, no. 1, pp. 189–198, 2000.
- [10] F. Zhao and A. V. Virkar, "Dependence of polarization in anode-supported solid oxide fuel cells on various cell parameters," *Journal of Power Sources*, vol. 141, no. 1, pp. 79–95, 2005.
- [11] J. T. S. Irvine, D. Neagu, M. C. Verbraeken, C. Chatzichristodoulou, C. Graves, and M. B. Mogensen, "Evolution of the electrochemical interface in high-temperature fuel cells and electrolyzers," *Nature Energy*, vol. 1, no. January, p. 15014, 2016.
- [12] J. Kilner, J. Druce, and T. Ishihara, "4 - electrolytes," in *High-Temperature Solid Oxide Fuel Cells for the 21st Century (Second Edition)* (K. Kendall and M. Kendall, eds.), pp. 85 – 132, Boston: Academic Press, second edition ed., 2016.
- [13] B. Timurkutluk, C. Timurkutluk, M. D. Mat, and Y. Kaplan, "A review on cell/stack designs for high performance solid oxide fuel cells," *Renewable and Sustainable Energy Reviews*, vol. 56, pp. 1101–1121, 2016.
- [14] T. Setoguchi, M. Sawano, K. Eguchi, and H. Arai, "Application of the stabilized zirconia thin film prepared by spray pyrolysis method to SOFC," *Solid State Ionics*, vol. 40/41, pp. 502–505, 1990.
- [15] K. Huang and S. C. Singhal, "Cathode-supported tubular solid oxide fuel cell technology: A critical review," *Journal of Power Sources*, vol. 237, pp. 84–97, 2013.
- [16] K. Huang, A. Zampieri, and M. Ise, "Cathode Polarizations of a Cathode-Supported Solid Oxide Fuel Cell," *Journal of The Electrochemical Society*, vol. 157, no. 10, p. B1471, 2010.
- [17] M. Liu, D. Dong, F. Zhao, J. Gao, D. Ding, X. Liu, and G. Meng, "High-performance cathode-supported SOFCs prepared by a single-step co-firing process," *Journal of Power Sources*, vol. 182, no. 2, pp. 585–588, 2008.
- [18] G. Chen, G. Guan, Y. Kasai, H. X. You, and A. Abudula, "Performance of cathode-supported SOFC with Ni 0.5Cu 0.5-CGO anode operated in humidified hydrogen and in low-concentration dry methane," *Journal of Solid State Electrochemistry*, vol. 16, no. 6, pp. 2071–2077, 2012.

- [19] G. Chen, H.-X. You, Y. Kasai, H. Sato, and A. Abudula, "Characterization of planer cathode-supported SOFC prepared by a dual dry pressing method," *Journal of Alloys and Compounds*, vol. 509, no. 16, pp. 5159–5162, 2011.
- [20] X. J. Chen, Q. L. Liu, S. H. Chan, N. P. Brandon, and K. A. Khor, "High-performance cathode-supported SOFC with perovskite anode operating in weakly humidified hydrogen and methane," *Fuel Cells Bulletin*, vol. 2007, no. 6, pp. 12–16, 2007.
- [21] K. Yamahara, C. P. Jacobson, S. J. Visco, and L. C. De Jonghe, "Catalyst-infiltrated supporting cathode for thin-film SOFCs," *Solid State Ionics*, vol. 176, no. 5-6, pp. 451–456, 2005.
- [22] T. Tsai and S. A. Barnett, "Effect of LSM-YSZ cathode on thin-electrolyte solid oxide fuel cell performance," *Solid State Ionics*, vol. 93, no. 3-4, pp. 207–217, 1997.
- [23] T. X. Ho, P. Kosinski, A. C. Hoffmann, and A. Vik, "Modeling of transport, chemical and electrochemical phenomena in a cathode-supported SOFC," *Chemical Engineering Science*, vol. 64, no. 12, pp. 3000–3009, 2009.
- [24] S. Su, X. Gao, Q. Zhang, W. Kong, and D. Chen, "Anode-Versus Cathode-Supported Solid Oxide Fuel Cell : Effect of Cell Design on the Stack Performance," *International Journal of Electrochemical Science*, vol. 10, pp. 2487–2503, 2015.
- [25] D. Perednis and L. J. Gauckler, "Solid oxide fuel cells with electrolytes prepared via spray pyrolysis," *Solid State Ionics*, vol. 166, pp. 229–239, Jan 2004.
- [26] R. P. Reolon, C. M. Halmenschlager, R. Neagu, C. De Fraga Malfatti, and C. P. Bergmann, "Electrochemical performance of gadolinia-doped ceria (CGO) electrolyte thin films for ITSOFC deposited by spray pyrolysis," *Journal of Power Sources*, vol. 261, pp. 348–355, 2014.
- [27] L. Peng and J. T. S. Irvine, "Fabrication of anode-supported zirconia thin film electrolyte based core-shell particle structure for intermediate temperature solid oxide fuel cells," *Progress in Natural Science: Materials International*, vol. 23, no. 3, pp. 302–307, 2013.
- [28] V. Vedaari, J. L. Young, and V. I. Birss, "A possible solution to the mechanical degradation of Ni-yttria stabilized zirconia anode-supported solid oxide fuel cells due to redox cycling," *Journal of Power Sources*, vol. 195, no. 17, pp. 5534–5542, 2010.

- [29] M. Cassidy, G. Lindsay, and K. Kendall, "The reduction of nickel-zirconia cermet anodes and the effects on supported thin electrolytes," *Journal of Power Sources*, vol. 61, pp. 189–192, Jul 1996.
- [30] S. D. Souza, S. J. Visco, and L. C. D. Jonghe, "Reduced-Temperature Solid Oxide Fuel Cell Based on YSZ Thin-Film Electrolyte," *Journal of The Electrochemical Society*, vol. 144, no. 3, pp. 35–37, 1997.
- [31] N. Q. Minh, "Solid oxide fuel cell technology - Features and applications," *Solid State Ionics*, vol. 174, no. 1-4, pp. 271–277, 2004.
- [32] Y. Xie, R. Neagu, C.-S. Hsu, X. Zhang, and C. Deces-Petit, "Spray Pyrolysis Deposition of Electrolyte and Anode for Metal-Supported Solid Oxide Fuel Cell," *Journal of The Electrochemical Society*, vol. 155, no. 4, p. B407, 2008.
- [33] K. J. Kim, B. H. Park, S. J. Kim, Y. Lee, H. Bae, and G. M. Choi, "Micro solid oxide fuel cell fabricated on porous stainless steel: a new strategy for enhanced thermal cycling ability.," *Scientific reports*, vol. 6, p. 22443, Mar 2016.
- [34] S. W. Baek, J. Jeong, H. Schlegl, A. K. Azad, D. S. Park, U. B. Baek, and J. H. Kim, "Metal-supported SOFC with an aerosol deposited in-situ LSM and 8YSZ composite cathode," *Ceramics International*, vol. 42, no. 2, pp. 2402–2409, 2016.
- [35] M. C. Tucker, "Progress in metal-supported solid oxide fuel cells: A review," *Journal of Power Sources*, vol. 195, no. 15, pp. 4570–4582, 2010.
- [36] N. E. Kiratzis, "Applications of the technique of solution aerosol thermolysis (SAT) in solid oxide fuel cell (SOFC) component fabrication," *Ionics*, pp. 1–20, 2016.
- [37] Z. Gao, L. V. Mogni, E. C. Miller, J. G. Railsback, and S. A. Barnett, "A perspective on low-temperature solid oxide fuel cells," *Energy Environ. Sci.*, vol. 9, no. 5, pp. 1602–1644, 2016.
- [38] B. C. Steele and A. Heinzl, "Materials for fuel-cell technologies.," *Nature*, vol. 414, no. November, pp. 345–352, 2001.
- [39] J. Will, A. Mitterdorfer, C. Kleinlogel, D. Perednis, and L. J. Gauckler, "Fabrication of thin electrolytes for second-generation solid oxide fuel cells," *Solid State Ionics*, vol. 131, pp. 79–96, 2000.

- [40] L. C. De Jonghe, C. P. Jacobson, and S. J. Visco, "Supported electrolyte thin film synthesis of solid oxide fuel cells," *Annual Review of Materials Research*, vol. 33, no. 1, pp. 169–182, 2003.
- [41] R. R. Chamberlin and J. S. Skarman, "Chemical Spray Deposition Process for Inorganic Films," *Journal of The Electrochemical Society*, vol. 113, no. 1, pp. 86–89, 1966.
- [42] D. Perednis and L. J. Gauckler, "Thin Film Deposition Using Spray Pyrolysis," *Journal of Electroceramics*, vol. 14, pp. 103–111, Mar 2005.
- [43] C. H. Chen, a. a. J. Buysman, E. M. Kelder, and J. Schoonman, "Fabrication of LiCoO<sub>2</sub>, thin film cathodes for rechargeable lithium battery by electrostatic spray pyrolysis," *Solid State Ionics*, vol. 80, no. 1, pp. 1–4, 1995.
- [44] G. L. Messing, S.-C. Zhang, and G. V. Jayanthi, "Ceramic Powder Synthesis by Spray Pyrolysis," *Journal of the American Ceramic Society*, vol. 76, no. 11, pp. 2707–2726, 1993.
- [45] C. Chen, P. J. J. M. van der Put, and J. Schoonman, "Morphology control of thin LiCoO<sub>2</sub> films fabricated using the electrostatic spray deposition (ESD) technique," *Journal of Materials Chemistry*, vol. 6, no. 5, pp. 765–771, 1996.
- [46] D. Perednis, O. Wilhelm, S. E. Pratsinis, and L. J. Gauckler, "Morphology and deposition of thin yttria-stabilized zirconia films using spray pyrolysis," *Thin Solid Films*, vol. 474, pp. 84–95, Mar 2005.
- [47] M. Garciasanchez, J. Pena, a. Ortiz, G. Santana, J. Fandino, M. Bizarro, F. Cruzgandarilla, and J. Alonso, "Nanostructured YSZ thin films for solid oxide fuel cells deposited by ultrasonic spray pyrolysis," *Solid State Ionics*, vol. 179, pp. 243–249, Apr 2008.
- [48] W. Siefert, "Corona spray pyrolysis: A new coating technique with an extremely enhanced deposition efficiency," *Thin Solid Films*, vol. 120, no. 4, pp. 267 – 274, 1984.
- [49] P. S. Patil, "Versatility of chemical spray pyrolysis technique," *Materials Chemistry and Physics*, vol. 59, no. 3, pp. 185–198, 1999.
- [50] D. Beckel, a. Bieberle-Hütter, a. Harvey, a. Infortuna, U. Muecke, M. Prestat, J. Rupp, and L. Gauckler, "Thin films for micro solid oxide fuel cells," *Journal of Power Sources*, vol. 173, pp. 325–345, Nov 2007.

- [51] D. Stender, R. Frison, K. Conder, J. L. M. Rupp, B. Scherrer, J. M. Martynczuk, L. J. Gauckler, C. W. Schneider, T. Lippert, and A. Wokaun, "Crystallization of zirconia based thin films," *Phys. Chem. Chem. Phys.*, vol. 17, no. 28, pp. 18613–18620, 2015.
- [52] L. Jadhav, A. Jamale, S. Bharadwaj, S. Varma, and C. Bhosale, "Synthesis and characterization of YSZ by spray pyrolysis technique," *Applied Surface Science*, vol. 258, pp. 9501–9504, Oct 2012.
- [53] M. Schlupp, S. Binder, J. Martynczuk, M. Prestat, and L. Gauckler, "Crack-free yttria stabilized zirconia thin films by aerosol assisted chemical vapor deposition: Influence of water and carrier gas," *Thin Solid Films*, vol. 522, pp. 58–65, Nov 2012.
- [54] M. Schlupp, M. Prestat, J. Martynczuk, J. Rupp, a. Bieberle-Hütter, and L. Gauckler, "Thin film growth of yttria stabilized zirconia by aerosol assisted chemical vapor deposition," *Journal of Power Sources*, vol. 202, pp. 47–55, Mar 2012.
- [55] O. Wilhelm, S. Pratsinis, D. Perednis, and L. Gauckler, "Electrospray and pressurized spray deposition of yttria-stabilized zirconia films," *Thin Solid Films*, vol. 479, pp. 121–129, May 2005.
- [56] R. Neagu, D. Perednis, a. Princivalle, and E. Djurado, "Influence of the process parameters on the ESD synthesis of thin film YSZ electrolytes," *Solid State Ionics*, vol. 177, pp. 1981–1984, Oct 2006.
- [57] Y. Xie, R. Neagu, C.-S. Hsu, X. Zhang, C. Deces-Petit, W. Qu, R. Hui, S. Yick, M. Robertson, R. Maric, and D. Ghosh, "Thin Film Solid Oxide Fuel Cells Deposited by Spray Pyrolysis," *Journal of Fuel Cell Science and Technology*, vol. 7, no. 2, p. 021007, 2010.
- [58] B. Scherrer, S. Heiroth, R. Hafner, J. Martynczuk, A. Bieberle-Hütter, J. L. M. Rupp, and L. J. Gauckler, "Crystallization and Microstructure of Yttria-Stabilized-Zirconia Thin Films Deposited by Spray Pyrolysis," *Advanced Functional Materials*, vol. 21, pp. 3967–3975, Oct 2011.
- [59] B. Scherrer, J. Martynczuk, H. Galinski, J. G. Grolig, S. Binder, A. Bieberle-Hütter, J. L. M. Rupp, M. Prestat, and L. J. Gauckler, "Microstructures of YSZ and CGO thin films deposited by spray pyrolysis: Influence of processing parameters on the porosity," *Advanced Functional Materials*, vol. 22, no. 16, pp. 3509–3518, 2012.

- [60] B. Scherrer, A. Rossi, J. Martynczuk, M. D. Rossell, A. Bieberle-Hütter, J. L. Rupp, R. Erni, and L. J. Gauckler, “Impact of substrate material and annealing conditions on the microstructure and chemistry of yttria-stabilized-zirconia thin films,” *Journal of Power Sources*, vol. 196, pp. 7372–7382, Sep 2011.
- [61] Y. Matsuzaki, M. Hishinuma, and I. Yasuda, “Growth of yttria stabilized zirconia thin films by metallo-organic, ultrasonic spray pyrolysis,” *Thin Solid Films*, vol. 340, no. 1-2, pp. 72–76, 1999.
- [62] D. Beckel, a. Dubach, a. R. Studart, and L. J. Gauckler, “Spray pyrolysis of  $\text{La}_{0.6}\text{Sr}_{0.4}\text{Co}_{0.2}\text{Fe}_{0.8}\text{O}_{3-\delta}$  thin film cathodes,” *Journal of Electroceramics*, vol. 16, pp. 221–228, May 2006.
- [63] S. Ricote, N. Bonanos, P. M. Rørvik, and C. Haavik, “Microstructure and performance of  $\text{La}_{0.58}\text{Sr}_{0.4}\text{Co}_{0.2}\text{Fe}_{0.8}\text{O}_{3\delta}$  cathodes deposited on  $\text{BaCe}_{0.2}\text{Zr}_{0.7}\text{Y}_{0.1}\text{O}_{3-\delta}$  by infiltration and spray pyrolysis,” *Journal of Power Sources*, vol. 209, pp. 172–179, Jul 2012.
- [64] D. Marrero-López, L. dos Santos-Gómez, J. Canales-Vázquez, F. Martín, and J. Ramos-Barrado, “Stability and performance of nanostructured  $\text{La}_{0.8}\text{Sr}_{0.2}\text{MnO}_3$  cathodes deposited by spray-pyrolysis,” *Electrochimica Acta*, vol. 134, pp. 159–166, Jul 2014.
- [65] U. Muecke, K. Akiba, a. Infortuna, T. Salkus, N. Stus, and L. Gauckler, “Electrochemical performance of nanocrystalline nickel/gadolinia-doped ceria thin film anodes for solid oxide fuel cells,” *Solid State Ionics*, vol. 178, pp. 1762–1768, Jan 2008.
- [66] U. P. Muecke, N. Luechinger, L. Schlagenhauf, and L. J. Gauckler, “Initial stages of deposition and film formation during spray pyrolysis Nickel oxide, cerium gadolinium oxide and mixtures thereof,” *Thin Solid Films*, vol. 517, pp. 1522–1529, Jan 2009.
- [67] L. Liu, G.-Y. Kim, and A. Chandra, “Fabrication of solid oxide fuel cell anode electrode by spray pyrolysis,” *Journal of Power Sources*, vol. 195, pp. 7046–7053, Oct 2010.
- [68] S. Barnett, “A new solid oxide fuel cell design based on thin film electrolytes,” *Energy*, vol. 15, no. 1, pp. 1–9, 1990.
- [69] DeVilBiss, “Service manual AG360 series: AG361 & AG361E, Air atomisation automatic spray guns,” 2014.

- [70] M. Wagner, “Thermogravimetric Analysis,” *Thermal Analysis in Practice*, pp. 162–186, 2017.
- [71] A. R. West, *Basic solid state chemistry*. John Wiley & Sons Inc, 1999.
- [72] E. Papastergiades, S. Argyropoulos, N. Rigakis, and N. E. Kiratzis, “Fabrication of ceramic electrolytic films by the method of solution aerosol thermolysis (SAT) for solid oxide fuel cells (SOFC),” *Ionics*, vol. 15, pp. 545–554, jan 2009.
- [73] W. D. Callister Jr and D. G. Rethwisch, *Materials science and engineering, 8<sup>th</sup> edition*. John Wiley & Sons, 2011.
- [74] W. H. Bragg and W. L. Bragg, “The reflection of x-rays by crystals,” in *Proc. R. Soc. Lond. A*, vol. 88, pp. 428–438, The Royal Society, 1913.
- [75] B. Cullity and S. Stock, *Elements of X-ray Diffraction, 3<sup>rd</sup> edition*. Prentice-Hall, 2001.
- [76] V. Mote, Y. Purushotham, and B. Dole, “Williamson-Hall analysis in estimation of lattice strain in nanometer-sized ZnO particles,” *Journal of Theoretical and Applied Physics*, vol. 6, no. 1, p. 6, 2012.
- [77] S. Henning and R. Adhikari, *Scanning Electron Microscopy, ESEM, and X-ray Microanalysis*. Elsevier Inc., 2017.
- [78] M. Abd Mutalib, M. A. Rahman, M. H. Othman, A. F. Ismail, and J. Jaafar, *Scanning Electron Microscopy (SEM) and Energy-Dispersive X-Ray (EDX) Spectroscopy*. Elsevier B.V., 2017.
- [79] B. J. Inkson, *Scanning Electron Microscopy (SEM) and Transmission Electron Microscopy (TEM) for Materials Characterization*. Elsevier Ltd, 2016.
- [80] M. D. A. Pereira-da silva and F. A. Ferri, *1 - Scanning Electron Microscopy*. Elsevier Inc., 2017.
- [81] W. Zhou, “Lecture notes in practical electron microscopy.” School of Chemistry, University of St. Andrews, 2016.
- [82] R. K. Mishra, A. K. Zachariah, and S. Thomas, *Energy-Dispersive X-ray Spectroscopy Techniques for Nanomaterial*. Elsevier Inc., 2017.
- [83] T. Walther, *Transmission Electron Microscopy of Nanostructures*. Elsevier Inc., 2017.
- [84] C. Y. Tang and Z. Yang, *Transmission Electron Microscopy (TEM)*. Elsevier B.V., 2017.

- [85] V. S. Kulkarni and C. Shaw, "Particle Size Analysis," *Essential Chemistry for Formulators of Semisolid and Liquid Dosages*, pp. 137–144, 2016.
- [86] C. Levoguer, "Using laser diffraction to measure particle size and distribution," *Metal Powder Report*, vol. 68, no. 3, pp. 15–18, 2013.
- [87] Q. A. Huang, R. Hui, B. Wang, and J. Zhang, "A review of AC impedance modeling and validation in SOFC diagnosis," *Electrochimica Acta*, vol. 52, no. 28, pp. 8144–8164, 2007.
- [88] S. Grassini, "Electrochemical impedance spectroscopy (EIS) for the in-situ analysis of metallic heritage artefacts," *Corrosion and Conservation of Cultural Heritage Metallic Artefacts*, pp. 347–367, 2013.
- [89] J. T. S. Irvine, D. C. Sinclair, and A. R. West, "Electroceramics: Characterization by Impedance Spectroscopy," *Advanced Materials*, vol. 2, no. 3, pp. 132–138, 1990.
- [90] M. Orazem and B. Tribollet, *Electrochemical Impedance Spectroscopy*. The ECS Series of Texts and Monographs, Wiley, 2008.
- [91] Y. S. Choudhary, L. Jothi, and G. Nageswaran, *Electrochemical Characterization*. Elsevier Inc., 2017.
- [92] M. Ghatee, M. Shariat, and J. Irvine, "Investigation of electrical and mechanical properties of 3YSZ/8YSZ composite electrolytes," *Solid State Ionics*, vol. 180, no. 1, pp. 57–62, 2009.
- [93] K. Huang, A. Zampieri, and M. Ise, "Cathode Polarizations of a Cathode-Supported Solid Oxide Fuel Cell," *Journal of The Electrochemical Society*, vol. 157, no. 10, p. B1471, 2010.
- [94] G. Chen, Y. Gao, Y. Luo, and R. Guo, "Effect of A site deficiency of LSM cathode on the electrochemical performance of SOFCs with stabilized zirconia electrolyte," *Ceramics International*, vol. 43, no. 1, pp. 1304–1309, 2017.
- [95] S. P. Jiang, "Development of lanthanum strontium manganite perovskite cathode materials of solid oxide fuel cells: a review," *Journal of Materials Science*, vol. 43, no. 21, pp. 6799–6833, 2008.
- [96] M. J. Jørgensen, S. Primdahl, C. Bagger, and M. Mogensen, "Effect of sintering temperature on microstructure and performance of LSM-YSZ composite cathodes," *Solid State Ionics*, vol. 139, pp. 1–11, 2001.

- [97] E. Perry Murray and S. A. Barnett, “(La,Sr)MnO<sub>3</sub>-(Ce,Gd)O<sub>2-x</sub> composite cathodes for solid oxide fuel cells,” *Solid State Ionics*, vol. 143, no. 3-4, pp. 265–273, 2001.
- [98] Y. Chen, L. Yang, F. Ren, and K. An, “Visualizing the structural evolution of LSM/xYSZ composite cathodes for SOFC by in-situ neutron diffraction,” *Scientific Reports*, vol. 4, 2014.
- [99] M. Mori, T. Abe, H. Itoh, O. Yamamoto, G. Q. Shen, Y. Takeda, and N. Imanishi, “Reaction mechanism between lanthanum manganite and yttria doped cubic zirconia,” *Solid State Ionics*, vol. 123, no. 1, pp. 113–119, 1999.
- [100] B. Ahmed, S. B. Lee, R. H. Song, J. W. Lee, T. H. Lim, and S. J. Park, “A study on sintering inhibition of La<sub>0.8</sub>Sr<sub>0.2</sub>MnO<sub>3</sub>-cathode material for cathode-supported fuel cells,” *Journal of the Korean Ceramic Society*, vol. 53, no. 5, pp. 494–499, 2016.
- [101] J. C. Ruiz-Morales, J. Canales-Vázquez, J. Peña-Martínez, D. Marrero-López, J. T. S. Irvine, and P. Núñez, “Microstructural optimisation of materials for SOFC applications using PMMA microspheres,” *Journal of Materials Chemistry*, vol. 16, no. 6, p. 540, 2006.
- [102] S. McIntosh and R. J. Gorte, “Direct Hydrocarbon Solid Oxide Fuel Cells,” *Chemical Reviews*, vol. 104, pp. 4845–4866, oct 2004.
- [103] F. G. E. Jones, *Tape casting, co-firing and electrical characterisation of a novel design solid oxide fuel cell: SOFCRoll*. PhD thesis, University of St. Andrews, 2005.
- [104] S. Boulfrad, M. Cassidy, and J. T. S. Irvine, “Adhesion and percolation parameters in two dimensional Pd-LSCM composites for SOFC anode current collection,” *Advanced Functional Materials*, vol. 20, no. 5, pp. 861–866, 2010.
- [105] M. Mamak, G. S. Métraux, S. Petrov, N. Coombs, G. A. Ozin, and M. A. Green, “Lanthanum strontium manganite/yttria-stabilized zirconia nanocomposites derived from a surfactant assisted, co-assembled mesoporous phase,” *Journal of the American Chemical Society*, vol. 125, no. 17, pp. 5161–5175, 2003.
- [106] J. Piao, K. Sun, N. Zhang, and S. Xu, “A study of process parameters of LSM and LSM-YSZ composite cathode films prepared by screen-printing,” *Journal of Power Sources*, vol. 175, pp. 288–295, 2008.

- [107] L. Gao, L. Wei, H. Guo, S. Gong, and H. Xu, "Deposition mechanisms of yttria-stabilized zirconia coatings during plasma spray physical vapor deposition," *Ceramics International*, vol. 42, no. 4, pp. 5530–5536, 2016.
- [108] D. Szymczewska, J. Karczewski, A. Chrzan, and P. Jasinski, "CGO as a barrier layer between LSCF electrodes and YSZ electrolyte fabricated by spray pyrolysis for solid oxide fuel cells," *Solid State Ionics*, vol. 302, pp. 113–117, 2017.
- [109] L. dos Santos-Gómez, J. Hurtado, J. M. Porrás-Vázquez, E. R. Losilla, and D. Marrero-López, "Durability and performance of CGO barriers and LSCF cathode deposited by spray-pyrolysis," *Journal of the European Ceramic Society*, no. January, pp. 1–9, 2018.
- [110] O. Wilhelm, L. Mädler, and S. E. Pratsinis, "Electrospray evaporation and deposition," *Journal of Aerosol Science*, vol. 34, no. 7, pp. 815–836, 2003.
- [111] N. Stelzer and J. Schoonman, "Synthesis of terbium-doped yttria-stabilized zirconia thin films by electrostatic spray deposition (ESD)," *Journal of Materials Synthesis and Processing*, vol. 4, no. 6, pp. 429–338, 1996.
- [112] T. P. Niesen and M. R. D. E. Guire, "Review : Deposition of Ceramic Thin Films at Low Temperatures from Aqueous Solutions," *Journal of Electroceramics*, pp. 169–207, 2001.
- [113] U. P. Muecke, G. L. Messing, and L. J. Gauckler, "The Leidenfrost effect during spray pyrolysis of nickel oxide-gadolinia doped ceria composite thin films," *Thin Solid Films*, vol. 517, pp. 1515–1521, jan 2009.
- [114] D. Beckel, a. Dubach, a. R. Studart, and L. J. Gauckler, "Spray pyrolysis of  $\text{La}_{0.6}\text{Sr}_{0.4}\text{Co}_{0.2}\text{Fe}_{0.8}\text{O}_{3-\delta}$  thin film cathodes," *Journal of Electroceramics*, vol. 16, pp. 221–228, may 2006.
- [115] J. L. Rupp, A. Infortuna, and L. J. Gauckler, "Microstrain and self-limited grain growth in nanocrystalline ceria ceramics," *Acta Materialia*, vol. 54, pp. 1721–1730, apr 2006.
- [116] J. B. Mooney, S. B. Raddin, and S. R. I. International, "Spray pyrolysis processing," *Ann. Rev. Mater. Sci.*, pp. 81–101, 1982.
- [117] S. B. Weber, H. L. Lein, T. Grande, and M. A. Einarsrud, "Influence of the precursor solution chemistry on the deposition of thick coatings by spray pyrolysis," *Surface and Coatings Technology*, vol. 221, pp. 53–58, 2013.

- [118] M. Choolaei, Q. Cai, R. C. Slade, and B. Amini Horri, "Nanocrystalline gadolinium-doped ceria (GDC) for SOFCs by an environmentally-friendly single step method," *Ceramics International*, vol. 44, no. 11, pp. 13286–13292, 2018.
- [119] M. Chourashiya, S. Pawar, and L. Jadhav, "Synthesis and characterization of Gd<sub>0.1</sub>Ce<sub>0.9</sub>O<sub>1.95</sub> thin films by spray pyrolysis technique," *Applied Surface Science*, vol. 254, pp. 3431–3435, mar 2008.
- [120] C. M. Halmenschlager, R. Neagu, L. Rose, C. F. Malfatti, and C. P. Bergmann, "Influence of the process parameters on the spray pyrolysis technique, on the synthesis of gadolinium doped-ceria thin film," *Materials Research Bulletin*, vol. 48, no. 2, pp. 207–213, 2013.
- [121] J. C. Vigui and J. Spitz, "Chemical Vapor Deposition at Low Temperatures," *J. Electrochem. Soc.*, vol. 122, no. 4, pp. 586–88, 1975.
- [122] S. Heiroth, R. Frison, J. L. Rupp, T. Lippert, E. J. Barthazy Meier, E. Müller Gubler, M. Döbeli, K. Conder, A. Wokaun, and L. J. Gauckler, "Crystallization and grain growth characteristics of yttria-stabilized zirconia thin films grown by pulsed laser deposition," *Solid State Ionics*, vol. 191, pp. 12–23, jun 2011.
- [123] a.P. Jamale, S. Dubal, S. Patil, C. Bhosale, and L. Jadhav, "Influence of substrate temperature on structural, morphological and electrical properties of La<sub>0.6</sub>Sr<sub>0.4</sub>Co<sub>0.2</sub>Fe<sub>0.8</sub>O<sub>3</sub> thin films for IT-SOFCs," *Applied Surface Science*, vol. 286, pp. 78–82, dec 2013.
- [124] D. Szymczewska, A. Chrzan, J. Karczewski, S. Molin, and P. Jasinski, "Spray pyrolysis of doped-ceria barrier layers for solid oxide fuel cells," *Surface and Coatings Technology*, vol. 313, pp. 168–176, 2017.
- [125] I. Taniguchi, R. Landschoot, and R. Schoonman, "Electrostatic spray deposition of Gd<sub>0.1</sub>Ce<sub>0.9</sub>O<sub>1.95</sub> and La<sub>0.9</sub>Sr<sub>0.1</sub>Ga<sub>0.8</sub>Mg<sub>0.2</sub>O<sub>2.87</sub> thin films," *Solid State Ionics*, vol. 160, pp. 271–279, jun 2003.
- [126] X. D. Zhou, B. Scarfino, and H. U. Anderson, "Electrical conductivity and stability of Gd-doped ceria/Y-doped zirconia ceramics and thin films," *Solid State Ionics*, vol. 175, no. 1-4, pp. 19–22, 2004.
- [127] J. L. Rupp, C. Solenthaler, P. Gasser, U. Muecke, and L. J. Gauckler, "Crystallization of amorphous ceria solid solutions," *Acta Materialia*, vol. 55, pp. 3505–3512, jun 2007.

- [128] M. G. Chourashiya, S. R. Bhardwaj, and L. D. Jadhav, "Fabrication of 10%Gd-doped ceria (GDC)/NiOGDC half cell for low or intermediate temperature solid oxide fuel cells using spray pyrolysis," *Journal of Solid State Electrochemistry*, vol. 14, pp. 1869–1875, mar 2010.
- [129] M. Chourashiya, S. Bharadwaj, and L. Jadhav, "Synthesis and characterization of electrolyte-grade 10%Gd-doped ceria thin film/ceramic substrate structures for solid oxide fuel cells," *Thin Solid Films*, vol. 519, pp. 650–657, nov 2010.
- [130] A. Tsoga, A. Naoumidis, W. Jungen, and D. Sto, "Processing and Characterisation of Fine Crystalline Ceria Gadolinia Yttria Stabilized Zirconia Powders," *Journal of the European Ceramic Society*, vol. 19, pp. 907–912, 1999.
- [131] A. Evans, A. Bieberle-Hütter, H. Galinski, J. L. M. Rupp, T. Ryll, B. Scherrer, R. Tölke, and L. J. Gauckler, "Micro-solid oxide fuel cells: status, challenges, and chances," *Monatshefte für Chemie - Chemical Monthly*, vol. 140, pp. 975–983, feb 2009.
- [132] H. B. Wang, C. R. Xia, G. Y. Meng, and D. K. Peng, "Deposition and characterization of YSZ thin films by aerosol-assisted CVD," *Materials Letters*, vol. 44, no. 1, pp. 23–28, 2000.
- [133] J. L. Rupp, "Ionic diffusion as a matter of lattice-strain for electroceramic thin films," *Solid State Ionics*, vol. 207, pp. 1–13, 2012.
- [134] A. Bieberle-Hütter, J. L. Hertz, and H. L. Tuller, "Fabrication and electrochemical characterization of planar Pt-CGO microstructures," *Acta Materialia*, vol. 56, no. 2, pp. 177–187, 2008.
- [135] J. Rupp and L. Gauckler, "Microstructures and electrical conductivity of nanocrystalline ceria-based thin films," *Solid State Ionics*, vol. 177, pp. 2513–2518, oct 2006.
- [136] T. Suzuki, I. Kosacki, and H. U. Anderson, "Microstructure-electrical conductivity relationships in nanocrystalline ceria thin films," *Solid State Ionics*, vol. 151, no. 1-4, pp. 111–121, 2002.
- [137] D. Chen, E. H. Jordan, and M. Gell, "Effect of solution concentration on splat formation and coating microstructure using the solution precursor plasma spray process," *Surface and Coatings Technology*, vol. 202, no. 10, pp. 2132–2138, 2008.

- [138] M. M. Hawkeye and M. J. Brett, "Glancing angle deposition: Fabrication, properties, and applications of micro- and nanostructured thin films," *Journal of Vacuum Science & Technology A: Vacuum, Surfaces, and Films*, vol. 25, no. 5, p. 1317, 2007.
- [139] Q.-Y. Chen, C.-X. Li, T. Wei, H.-B. Sun, S.-L. Zhang, X.-T. Luo, G.-J. Yang, C.-J. Li, and M.-L. Liu, "Controlling grain size in columnar YSZ coating formation by droplet filtering assisted PS-PVD processing," *RSC Advances*, vol. 5, no. 124, pp. 102126–102133, 2015.
- [140] S. Rezanka, G. Mauer, and R. Vaßen, "Improved thermal cycling durability of thermal barrier coatings manufactured by PS-PVD," *Journal of Thermal Spray Technology*, vol. 23, no. 1-2, pp. 182–189, 2014.
- [141] P. Bohac and L. Gauckler, "Chemical spray deposition of YSZ and GCO solid electrolyte films," *Solid State Ionics*, vol. 119, pp. 317–321, apr 1999.
- [142] T. Nguyen and E. Djurado, "Deposition and characterization of nanocrystalline tetragonal zirconia films using electrostatic spray deposition," *Solid State Ionics*, vol. 138, pp. 191–197, 2001.
- [143] I. Taniguchi and J. Schoonman, "Electrostatic spray deposition of Perovskite-type oxides thin films with porous microstructure," *Journal of Materials Synthesis and Processing*, vol. 10, no. 5, pp. 267–275, 2002.
- [144] H. S. Noh, H. Lee, B. K. Kim, H. W. Lee, J. H. Lee, and J. W. Son, "Microstructural factors of electrodes affecting the performance of anode-supported thin film yttria-stabilized zirconia electrolyte (1  $\mu\text{m}$ ) solid oxide fuel cells," *Journal of Power Sources*, vol. 196, no. 17, pp. 7169–7174, 2011.
- [145] X. Ge, X. Huang, Y. Zhang, Z. Lu, J. Xu, K. Chen, D. Dong, Z. Liu, J. Miao, and W. Su, "Screen-printed thin YSZ films used as electrolytes for solid oxide fuel cells," *Journal of Power Sources*, vol. 159, pp. 1048–1050, 2006.
- [146] M. Chen, Y. L. Liu, A. Hagen, P. V. Hendriksen, and F. W. Poulsen, "LSM-YSZ reactions in different atmospheres," *Fuel Cells*, vol. 9, no. 6, pp. 833–840, 2009.
- [147] T. Setoguchi, K. Eguchi, and H. Arai, "Thin film fabrication of stabilized zirconia for solid oxide fuel cells," *Proceedings of SPIE - The International Society for Optical Engineering*, vol. 1519, no. pt 1, pp. 74–79, 1991.
- [148] B. Steele and J.-M. Bae, "Properties of  $\text{La}_{0.6}\text{Sr}_{0.4}\text{Co}_{0.2}\text{Fe}_{0.8}\text{O}_{3-x}$  (lscf) double layer cathodes on gadolinium-doped cerium oxide (cgo) electrolytes: Ii. role of

- oxygen exchange and diffusion,” *Solid State Ionics*, vol. 106, no. 3, pp. 255 – 261, 1998.
- [149] H. A. Hamedani, K.-H. Dahmen, D. Li, H. Peydaye-Saheli, H. Garmestani, and M. Khaleel, “Fabrication of gradient porous LSM cathode by optimizing deposition parameters in ultrasonic spray pyrolysis,” *Materials Science and Engineering: B*, vol. 153, pp. 1–9, sep 2008.
- [150] H. A. Hamedani, M. Baniassadi, M. Khaleel, X. Sun, S. Ahzi, D.ruch, and H. Garmestani, “Microstructure, property and processing relation in gradient porous cathode of solid oxide fuel cells using statistical continuum mechanics,” *Journal of Power Sources*, vol. 196, no. 15, pp. 6325–6331, 2011.
- [151] A. Infortuna, A. S. Harvey, and L. J. Gauckler, “Microstructures of CGO and YSZ thin films by pulsed laser deposition,” *Advanced Functional Materials*, vol. 18, no. 1, pp. 127–135, 2008.
- [152] M. V. F. Schlupp, B. Scherrer, H. Ma, J. G. Grolig, J. Martynczuk, M. Prestat, and L. J. Gauckler, “Influence of microstructure on the cross-plane oxygen ion conductivity of yttria stabilized zirconia thin films,” *Physica Status Solidi (a)*, vol. 209, no. 8, pp. 1414–1422, 2012.
- [153] M. V. Schlupp, J. Martynczuk, M. Prestat, and L. J. Gauckler, “Precursor decomposition, microstructure, and porosity of yttria stabilized zirconia thin films prepared by aerosol-assisted chemical vapor deposition,” *Advanced Energy Materials*, vol. 3, no. 3, pp. 375–385, 2013.
- [154] J. C. Ruiz-Morales, J. Canales-Vázquez, C. Savaniu, D. Marrero-López, P. Núñez, W. Zhou, and J. T. S. Irvine, “A new anode for solid oxide fuel cells with enhanced OCV under methane operation.,” *Physical chemistry chemical physics : PCCP*, vol. 9, pp. 1821–30, apr 2007.
- [155] H. S. Spacil, “Electrical device including nickel-containing stabilized zirconia electrode,” March 1970. US Patent 3,503,809.
- [156] B. Shri Prakash, S. Senthil Kumar, and S. Aruna, “Properties and development of Ni/YSZ as an anode material in solid oxide fuel cell: A review,” *Renewable and Sustainable Energy Reviews*, vol. 36, pp. 149–179, 2014.
- [157] L. Zhang, L. Zhu, and A. V. Virkar, “Nanostructured Cathodes for Solid Oxide Fuel Cells by a Solution Spray-Coating Process,” *Journal of The Electrochemical Society*, vol. 163, no. 13, pp. 1358–1365, 2016.

- [158] Q. Cai, C. S. Adjiman, and N. P. Brandon, "Modelling the 3D microstructure and performance of solid oxide fuel cell electrodes: Computational parameters," *Electrochimica Acta*, vol. 56, no. 16, pp. 5804–5814, 2011.
- [159] Y. Liu, S. Zha, and M. Liu, "Novel nanostructured electrodes for solid oxide fuel cells fabricated by combustion chemical vapor deposition (CVD)," *Advanced Materials*, vol. 16, no. 3, pp. 256–260, 2004.
- [160] C. Ni, L. Lu, D. N. Miller, M. Cassidy, and J. T. Irvine, "Microstructure dependence of performance degradation for intermediate temperature solid oxide fuel cells based on the metallic catalyst infiltrated La- and Ca-doped SrTiO<sub>3</sub> anode support," *Journal of Materials Chemistry A*, vol. 6, no. 13, pp. 5398–5406, 2018.
- [161] E. P. Murray, T. Tsai, and S. a. Barnett, "A direct-methane fuel cell with a ceria-based anode," *Nature*, vol. 400, no. 6745, pp. 649–651, 1999.
- [162] G. Tsimekas, E. Papastergiades, and N. Kiratzis, "Morphology and structure of ceramic thin films deposited by spray pyrolysis," *ECS Journal of Solid State Science and Technology*, vol. 6, no. 8, pp. 4–11, 2017.
- [163] H. J. Park, Z. Shao, W. Wang, and K. S. Moon, "Electrochemical Performance of a Ni and YSZ Composite Synthesised by Ultrasonic Spray Pyrolysis as an Anode for SOFCs," *Fuel Cells*, vol. 11, pp. 654–660, oct 2011.
- [164] T. Fukui, S. Ohara, M. Naito, and K. Nogi, "Synthesis of NiO/YSZ composite particles for an electrode of solid oxide fuel cells by spray pyrolysis," *Powder Technology*, vol. 132, pp. 52–56, may 2003.
- [165] A. Atkinson, S. Barnett, R. J. Gorte, J. T. S. Irvine, a. J. McEvoy, M. Mogens, S. C. Singhal, and J. Vohs, "Advanced anodes for high-temperature fuel cells," *Nature materials*, vol. 3, pp. 17–27, jan 2004.
- [166] R. J. Gorte, S. Park, J. M. Vohs, and C. Wang, "Anodes for Direct Oxidation of Dry Hydrocarbons in a Solid-Oxide Fuel Cell," *Advanced Materials*, vol. 12, pp. 1465–1469, oct 2000.
- [167] M. Melchionna and P. Fornasiero, "The role of ceria-based nanostructured materials in energy applications," *Materials Today*, vol. 17, no. 7, pp. 349–357, 2014.
- [168] S.-I. Lee, K. Ahn, J. M. Vohs, and R. J. Gorte, "Cu-Co Bimetallic Anodes for Direct Utilization of Methane in SOFCs," *Electrochemical and Solid-State Letters*, vol. 8, no. 1, p. A48, 2005.

- [169] X.-h. Guo, C.-c. Mao, J. Zhang, J. Huang, W.-n. Wang, and Y.-h. Deng, "Cobalt-Doping-Induced Synthesis of Ceria Nanodisks and Their Significantly Enhanced Catalytic Activity," *Small*, no. 10, pp. 1515–1520, 2012.
- [170] J. T. S. Irvine and A. Sauvet, "Improved Oxidation of Hydrocarbons with New Electrodes in High Temperature Fuel Cells," *Fuel Cells*, no. 3, pp. 205–210, 2001.
- [171] R. A. George, "Status of tubular SOFC field unit demonstrations," *Journal of Power Sources*, vol. 86, no. 1, pp. 134–139, 2000.
- [172] R. a. George and N. F. Bessette, "Reducing the manufacturing cost of tubular solid oxide fuel cell technology," *Journal of Power Sources*, vol. 71, no. 1-2, pp. 131–137, 1998.
- [173] S. Jung, C. Lu, H. He, K. Ahn, R. J. Gorte, and J. M. Vohs, "Influence of composition and Cu impregnation method on the performance of Cu/CeO<sub>2</sub>/YSZ SOFC anodes," *Journal of Power Sources*, vol. 154, no. 1, pp. 42–50, 2006.
- [174] N. Kiratzis, P. Holtappels, C. Hatchwell, M. Mogensen, and J. Irvine, "Preparation and Characterization of Copper/Yttria Titania Zirconia Cermets for Use as Possible Solid Oxide Fuel Cell Anodes," *Fuel Cells*, vol. 1, no. 3-4, pp. 211–218, 2001.
- [175] Y. Li, X. Zhu, Z. Lu, Z. Wang, W. Jiang, X. Huang, and W. Su, "Cobalt-impregnated La<sub>0.75</sub>Sr<sub>0.25</sub>Cr<sub>0.5</sub>Mn<sub>0.5</sub>O<sub>3-d</sub> anodes for solid oxide fuel cells," *International Journal of Hydrogen Energy*, vol. 39, no. 15, pp. 7980–7987, 2014.